

Magnetoconvection in the  
Earth's core and flux expulsion  
into the mantle

by

Stephen John Drew

A thesis submitted to the Faculty of  
Science, University of Glasgow, for the  
degree of Doctor of Philosophy

Department of Mathematics,  
University of Glasgow  
October, 1992

© Stephen J. Drew, 1992

ProQuest Number: 13834194

All rights reserved

INFORMATION TO ALL USERS

The quality of this reproduction is dependent upon the quality of the copy submitted.

In the unlikely event that the author did not send a complete manuscript and there are missing pages, these will be noted. Also, if material had to be removed, a note will indicate the deletion.



ProQuest 13834194

Published by ProQuest LLC (2019). Copyright of the Dissertation is held by the Author.

All rights reserved.

This work is protected against unauthorized copying under Title 17, United States Code  
Microform Edition © ProQuest LLC.

ProQuest LLC.  
789 East Eisenhower Parkway  
P.O. Box 1346  
Ann Arbor, MI 48106 – 1346

Thesis  
9346  
copy 2

GLASGOW  
UNIVERSITY  
LIBRARY

*To my family*

# Contents

	Page
<b>Preface</b>	iv
<b>Summary</b>	v
<b>Chapter 1 Introduction</b>	
1.1 INTRODUCTION	1
<b>Chapter 2 Thermal convection in a spherical shell with a variable radius ratio</b>	
2.1 INTRODUCTION	8
2.2 MODEL	10
2.2.1 <i>Governing equations</i>	10
2.2.2 <i>Method of solution</i>	12
2.2.3 <i>Boundary conditions</i>	14
2.2.4 <i>Choice of temperature distribution</i>	16
2.3 NUMERICAL RESULTS	16
2.3.1 <i>Finding unstable modes</i>	16
2.3.2 <i>Initialisation</i>	17
2.3.3 <i>Plotting the eigenfunctions</i>	18
2.3.4 <i>Comparison with Fearn and Proctor (1983a)</i>	18
2.3.5 <i>Convergence of solutions</i>	20
2.3.6 <i>Variation of <math>R_c</math> with <math>r_{ib}</math></i>	20
2.3.7 <i>Variation of <math>R_c</math> with <math>\Lambda</math></i>	25
2.3.8 <i>Dipole parity</i>	30
2.3.9 <i>Effect of changing basic state <math>B_0</math></i>	33
2.4 EFFECT OF DIFFERENTIAL ROTATION	36
2.4.1 $q = 10^{-6}$	40

2.4.2	$q = 1$	45
2.4.3	<i>Initial decrease of <math>R_c</math> with <math>R_m</math></i>	50
2.5	VARYING THE TEMPERATURE DISTRIBUTION	51
2.5.1	<i>Compositional convection type distribution</i>	51
2.6	DISCUSSION AND CONCLUSIONS	56
<b>Chapter 3</b>	<b>The effect of a stable layer at the core-mantle boundary on thermal convection</b>	
3.1	INTRODUCTION	60
3.2	MODEL	61
3.3	RESULTS	62
3.3.1	$\Lambda \ll O(1)$	63
3.3.2	$\Lambda = O(1)$	69
3.3.3	$\Lambda \gg O(1)$	74
3.4	DISCUSSION	74
<b>Chapter 4</b>	<b>Magnetic field expulsion into a conducting mantle</b>	
4.1	INTRODUCTION	85
4.2	MODEL	87
4.2.1	<i>Governing equations</i>	87
4.2.2	<i>Boundary conditions</i>	90
4.2.3	<i>Matching the solution between the layers</i>	92
4.2.4	<i>Method of solution</i>	93
4.2.5	<i>Numerical stability of the model</i>	94
4.2.6	<i>Mantle field</i>	94
4.3	CHECKING CASES	94
4.3.1	<i>Decay time</i>	95
4.3.2	<i>Comparison with Bloxham's results</i>	98
4.4	RESULTS	100
4.4.1	$\eta = \text{constant}$	102
4.4.2	$\eta = f(z)$	102

4.4.3 $\eta = g(x)$	106
4.4.4 <i>Long term behaviour</i>	113
4.4.5 <i>Effect of changing initial magnetic field</i>	118
4.5 DISCUSSION	118
<b>References</b>	121

# Preface

This thesis is submitted to the University of Glasgow in accordance with the requirements for the degree of Doctor of Philosophy.

I would like to express my sincere gratitude to my supervisor Dr. D.R. Fearn for his advice, encouragement and guidance throughout the period of my research, and also to the other members of the MHD group at the University of Glasgow for much helpful discussion.

I must also thank Professor R. W. Ogden for the help and assistance he has provided during my time in the Department of Mathematics.

Thanks are also due to the Science and Engineering Research Council of Great Britain for providing me with a Research Studentship for the three years of my research.

Finally, I am very grateful to my family for the support and encouragement they have given me throughout.

## Summary

In this thesis we consider a number of problems aimed towards gaining a better understanding of the processes deep in the Earth's core which act to maintain the Earth's magnetic field against ohmic decay.

Firstly, as a model for the Earth's core, we consider a rapidly rotating electrically conducting fluid sphere with a solid concentric inner core. We impose an azimuthal magnetic field, an azimuthal shear flow and a temperature distribution appropriate to a uniform distribution of heat sources through the core, and investigate numerically the linear stability of this basic state. We consider the effect of inner core radius, magnetic field strength and differential rotation on thermal convection, comparing our results with the work of Fearn and Proctor (1983a) who considered a similar model without an inner core. Later we alter our temperature distribution, attempting to model thermally the effects of compositional convection, the process believed to be the primary power source for the geodynamo.

Continuing with the same model, we next study the effect of introducing a stably stratified layer adjacent to the core-mantle boundary. We consider a wide range of magnetic field strengths, and compare our results with work done previously in simpler geometries.

Finally, we look at a 2D numerical model of the expulsion of magnetic field from the Earth's core into a conducting mantle, driven by a prescribed upwelling fluid motion. We consider a variety of types of conductivity profile for the mantle and compare with the fully insulating mantle solution as studied by Bloxham (1986). Motivated by the recent work on lower mantle conductivity, we look at a conductivity profile with large lateral heterogeneity in conductivity.

All our calculations were performed on the University of Glasgow's IBM

3090-150E/VF mainframe. All our graphs and contour plots were produced with the aid of the UNIRAS graphics package. The results included in the following chapters can also be found in Drew 1991;1992a,b.

# Chapter 1

## Introduction

### 1.1 INTRODUCTION

The primary motivation for the work studied here, is towards gaining a greater understanding of the processes deep in the Earth's interior which act to maintain the Earth's magnetic field against ohmic decay. The origin and structure of the Earth's magnetic field have been studied for centuries, and we are still no little way from a full understanding of its properties. The cause of many of the difficulties of the subject lie in our lack of knowledge of the constituent materials and their physical properties in the Earth's core and mantle, although our picture of the Earth's interior continues to improve as high-pressure high-temperature experiments are performed and more data is accumulated.

Direct measurements of the Earth's magnetic field go back several centuries. The problem of ship navigation provided a great motivation for early studies and measurements of the magnetic field, but nowadays more accurate measurements are made at observatories throughout the world and from satellites. This collected data has resulted in the production of charts of the external magnetic field at different points in time (Bloxham and Gubbins 1985; Bloxham, Gubbins and Jackson 1989). These show that some parts of the field vary little over time, but there is also what is known as the geomagnetic secular variation which incorporates the observed westward drift of some of the field features. Also the declination angle (the angle between true north and magnetic north) varies noticeably with time. As useful as these direct observations are, the period of time they encompass is very short compared with the geological timescales of the Earth and its magnetic field. Evidence obtained from paleomagnetism however,

provides much information about the behaviour of the Earth's field going back some three billion years. During the formation of rock (e.g. from lava cooling or from sedimentation at the bottom of lakes), a "magnetic record" of the magnetic field at the time of solidification is frozen into the rock. Paleomagnetists can analyse these rocks and calculate the magnitude and direction of this frozen-in field, and this has provided information about the occurrence and regularity of field reversals. In addition by comparing the magnetic field strengths from these records, it can be seen that the average magnetic field strength has remained relatively constant. If we compare this with the ohmic decay timescale [ $O(10^5$  years)] for the Earth's field, then the longevity of the Earth's field, together with other features such as reversals and the secular variation, means that the field cannot be a fossil field, but must be being maintained by a dynamo process. The only feasible location for the generation region is the electrically conducting fluid core. Here we have a conducting fluid moving through a magnetic field, and such a motion induces the flow of electrical currents, which can in the right conditions produce a magnetic field which reinforces the original field. The Earth's core extends outwards from the centre to a radius of  $3480\text{km}$  (Dziewonski and Anderson 1981). It consists mainly of iron, with the remainder made up from lighter elements. There has been considerable argument over the identity of the lighter constituents (see e.g., Fearn 1989b; Jeanloz 1990), with Silicon, Oxygen and Sulphur among the main contenders. As the Earth has cooled, a solid inner core has formed (radius  $1221.5\text{km}$ , Dziewonski and Anderson 1981) as the liquid iron alloy in the core has solidified. When an alloy such as the iron-lighter constituent mixture freezes, most of the lighter constituent remains in the fluid, which is why the inner core is almost pure iron. This freezing process produces latent heat and also provides a source of compositionally buoyant light material at the inner core boundary which rises upwards through the core. This compositionally driven convection could thus provide the power for the geodynamo. Other energy sources have been considered for the geodynamo, as is discussed further in Chapter 2, but the primary source of energy is believed to be compositional

convection (see e.g., Gubbins 1977; Gubbins and Masters 1979; Gubbins, Masters and Jacobs 1979; Loper 1989).

The task of modelling the geodynamo is immensely difficult. Not only does the complicated interaction of conducting fluid and magnetic field mean that the governing equations are highly non-linear, but any model is required to explain observed features of the field such as the secular variation, and most importantly the field reversals. To make matters worse, it has been shown through Cowling's theorem and its later extensions (see e.g., Soward 1991; Roberts and Soward 1992) that an axisymmetric magnetic field cannot be maintained by dynamo action, so that any working dynamo model must necessarily contain non-axisymmetry. Although a fully three dimensional numerical simulation of the geodynamo is becoming more feasible with the advent of modern super-computing facilities, in the past it has been necessary to consider simpler models in more basic geometries, focusing in on small parts of the problem, and hoping to gradually build up an overall picture of the actual behaviour. Indeed, much useful information can still be gained from such an approach.

There are many different points of attack for the problem. From the charts of the magnetic field at the Earth's surface mentioned above, by extrapolating these through the mantle, maps of the magnetic field at the core-mantle boundary can be obtained. From these, constraints on the flow at the top of the core can be determined (see e.g., Gubbins 1982, 1991; Gire, Le Mouél and Madden 1986; Voorhies 1986; Bloxham and Jackson 1991). This is particularly useful, as although seismologists can provide us with estimates of quantities such as the core radii, conductivities and densities, we have little knowledge concerning the nature of the flow in the core. This is important, as clearly the efficiency of the geodynamo is strongly dependent on the form of the flow.

A simpler approach to modelling the geodynamo is to consider the kinematic dynamo problem. Here we impose a flow  $\mathbf{U}_0$  on a magnetic field  $\mathbf{B}$  and ignore the back-reaction of the magnetic field on the flow. We thus have only to solve the magnetic induction equation

$$\nabla \times (\eta(\nabla \times \mathbf{B}) - \mathbf{U}_0 \times \mathbf{B}) + \frac{\partial \mathbf{B}}{\partial t} = 0 \quad (1.1)$$

ignoring the equations of motion. We adopt a kinematic approach in Chapter 4.

Another approach to the problem is to study the linear stability of some basic state (see e.g., Gubbins and Roberts 1987; Fearn, Roberts and Soward 1988). This is the approach we adopt in Chapters 2 and 3. Starting from a plane layer geometry (e.g, Soward 1979; Eltayeb and Kumar 1977; Fearn and Proctor 1983b) and working through intermediate cylindrical models (e.g, Acheson 1978; Fearn 1983a,b, 1984, 1985, 1988, 1989; Fearn and Weiglhofer 1992a) to finally considering the spherical case, (e.g, Fearn 1979a,b; Fearn and Proctor 1983a; Fearn and Weiglhofer 1991a,b, 1992b) which is of course the most relevant geometry for the Earth, the use of linear stability analysis has enabled a picture to be built up of the different possible instability mechanisms: thermal instabilities (e.g., Eltayeb and Kumar 1977; Fearn 1979a,b; Fearn and Proctor 1983a), which are studied here in Chapters 2 and 3, the buoyancy catalysed instability (Soward 1979; Roberts and Loper 1979; Acheson 1983), the ideal (field gradient) instability (Acheson 1983, Fearn and Weiglhofer 1991a,b), resistive instabilities (Fearn and Weiglhofer 1991b, 1992a), the exceptional instability (Roberts and Loper 1979) and the dynamic instability (Malkus 1967), although the last two mechanisms require magnetic field strengths much higher than those believed to exist in the Earth's core. We are interested here only in the thermal instabilities. A more detailed description of the other magnetic instabilities can be found for example in Fearn, Roberts and Soward (1988).

In Chapter 2 we consider the linear stability of a basic state

$$B_0(r, \theta)\mathbf{1}_\phi, U_0(r, \theta)\mathbf{1}_\phi, T_0(r) \quad (1.2)$$

where  $(r, \theta, \phi)$  are spherical polar coordinates, in a rapidly rotating spherical shell, as a model for the Earth's core. In our model we include a solid inner

core, and we investigate the effect of varying the inner core radius on thermal convection. Although, as we mentioned above, compositional convection is the process believed to be the main source of energy for the geodynamo, our model uses thermal energy as would be appropriate for a uniform distribution of heat sources throughout the core. The reason that we do this is because the thermally driven convection is much simpler to model mathematically, and is qualitatively similar to compositional convection. Also, the nature of the rise of the buoyant light material from the inner core boundary, and its interaction with rotation and magnetic field is a problem which is only now beginning to be investigated (see e.g., Loper 1989), so it makes sense to use the better understood thermal convection. This is the process used in almost all other studies (e.g., Roberts 1968; Eltayeb and Kumar 1977, Fearn and Proctor 1983a), so for comparative purposes it makes sense to do so here. Later on in Chapter 2, we do alter our temperature distribution and thermal boundary conditions in an attempt to model compositionally driven convection more closely.

Although individually the addition of either a magnetic field or rotation has the effect of inhibiting thermal convection, initially when a magnetic field is added to a rotating system there is the opposite effect, this proving beneficial to convection (see e.g., Fearn, Roberts and Soward 1988). Increasing the strength of the magnetic field continues to provide this effect until the Lorentz force balances the Coriolis force after which point a further increase in the magnetic field strength acts to inhibit convection once again. We investigate this behaviour for different inner core radii, and also look at the effects of magnetic field strength and differential rotation on thermal convection, and compare our results with those of Fearn and Proctor (1983a), who studied a similar model, but without an inner core.

In Chapter 3, we consider a slightly different problem. Here we investigate the effect on thermal convection of the existence of a stably stratified layer at the core-mantle boundary. Motivation for such a study comes from two sources. Firstly, Whaler (1980) presented geomagnetic results which supported the ex-

istence of a stably stratified layer at the core-mantle boundary, and secondly, this was followed by theoretical analyses by Fearn and Loper (1981) and Gubbins, Thomson and Whaler (1982) which supported this. The next step was to construct models of convection in rapidly rotating electrically conducting fluid containing a stably stratified region. Boda (1988) and Ševčík (1989) studied a plane layer model with the upper part of the fluid stably stratified, and Fearn and Richardson (1991) looked at a cylindrical model with a stable layer adjacent to the outer boundary. In Chapter 3 we extend these results, moving to the spherical case. We use essentially the same model as in Chapter 2, but we modify the temperature distribution to allow a stably stratified layer to exist below the core-mantle boundary. We study the effect of adding this layer in three regimes of magnetic field strength: with weak, moderate and strong fields, and compare our findings with the results from previous models.

For our final results in Chapter 4, we turn to a different problem, although one still of interest towards understanding the Earth's magnetic field. We broaden our approach, now looking to the Earth's mantle as well as the core considering a subject currently of great interest, namely the electrical conductivity of the mantle. The Earth's solid mantle extends from its boundary with the core at a radius of  $3480\text{km}$  virtually to the surface at radius  $6371\text{km}$  (Dziewonski and Anderson 1981). The electrical conductivity of the mantle is not known with any accuracy, and previous models have either assumed that the mantle is electrically insulating, or adopted simple profiles for the conductivity. In recent years however, experiments performed at temperatures and pressures close to those found deep in the mantle have begun to produce estimates for the conductivity of deep mantle constituents (see e.g., Li and Jeanloz 1987, Peyronneau and Poirier 1989). These have produced conflicting values for the magnitude of mantle conductivity, but it is now more strongly accepted that the  $D''$  layer which occupies the bottom  $200\text{--}300\text{km}$  of the mantle (Young and Lay 1987), may have an appreciably higher conductivity than the rest of the mantle. This is because it is believed that in the  $D''$  layer there may be appreciable amounts of iron from the core present

which results in a higher conductivity there. The presence of pockets of iron in  $D''$  suggests that there may be a large lateral lateral heterogeneity in conductivity over a very short lengthscale (Jeanloz 1990), with a range of conductivity varying from metallic conductivity to virtual insulation. We attempt to model this heterogeneity as part of Chapter 4.

Our study of the effects of mantle conductivity takes the form of an extension of the work of Bloxham (1986). He considered a plane layer model where a uniform horizontal magnetic field was expelled into an insulating mantle by an upwelling fluid flow in the core. We look at the same problem here, but allow the mantle to have an arbitrary conductivity which can vary laterally and with height. We consider various profiles for the conductivity in the mantle, in particular trying to model the possible large lateral variation in conductivity in the  $D''$  layer.

## Chapter 2

# Thermal convection in a spherical shell with a variable radius ratio

### 2.1 INTRODUCTION

In this chapter we consider, as a model for the Earth's core, an electrically conducting fluid sphere with a solid concentric inner core. We impose an azimuthal magnetic field  $\mathbf{B}_0(r, \theta)\mathbf{1}_\phi$ , azimuthal shear flow  $\mathbf{U}_0(r, \theta)\mathbf{1}_\phi$  and temperature distribution  $T_0(r)$ , where  $(r, \theta, \phi)$  are spherical polar coordinates, and consider the linear stability of this basic state. We investigate the effect of inner core radius, magnetic field strength, and differential rotation on thermal convection.

The Earth's magnetic field has been maintained against ohmic losses for the past few billion years by the action of a dynamo mechanism in the outer core. The complicated interaction of the fluid velocity and the magnetic field acts to maintain the field against ohmic decay. The high non-linearity inherent in the full set of equations for the problem ensures that any numerical calculations performed are extremely demanding on storage and CPU time. It is common, therefore, to study simpler problems such as kinematic dynamo models, where the back reaction of the magnetic field on the flow is neglected, or, as here, convection in the presence of a prescribed magnetic field.

Much study has been made concerning the suitability of possible energy sources for the dynamo. Sources such as precession and thermal convection have been considered, but current thinking favours compositional convection, where the energy comes from the rise of buoyant light material released by freezing at the inner core boundary (Fearn 1989b, Loper 1989). Because of its being

mathematically simpler, thermal convection is the process used here, although we later modify the temperature distribution to model the effects of compositional buoyancy.

Thermal convection in a sphere has been studied by many authors (e.g., Roberts 1968, Eltayeb and Kumar 1977, Fearn 1979, Fearn and Proctor 1983a). They used a uniform distribution of radioactive heat sources in the core to provide a temperature distribution, and this is the mechanism we study to begin with, in order to have some check for our results. This method of heating, however, is no longer considered to be the primary source of energy for the dynamo as it is doubtful that there is enough radioactive material to provide the necessary amount of heating.

One addition to the models referred to above, is that of an inner core. The inner core has grown gradually outwards through the core as the earth has cooled, and we investigate the effect on convection of this growth. We find that there is a noticeable effect on core convection, particularly when the inner core radius becomes large and the restriction in space becomes important.

It is well known that, although separately the addition of differential rotation or a magnetic field acts to inhibit convection, introducing a magnetic field to a rapidly rotating system initially reduces the critical Rayleigh number,  $R_c$  (the non-dimensional parameter which marks the point of onset of convection). Increasing the magnetic field strength continues to provide this beneficial effect until the Lorentz force balances the Coriolis force, after which increasing the field results in convection becoming inhibited. For values of the Roberts number  $q = \kappa/\eta \leq O(1)$  which we study here, the minimum value of  $R_c$  is reached when the Elsasser number,  $\Lambda$ , a non-dimensional measure of the magnetic field strength, is  $O(1)$  (see Fearn, Roberts and Soward 1988). For  $q > O(1)$  the minimum is at  $\Lambda = O(q)$  (Acheson 1979; Fearn 1989a). The position of this minimum, as will be seen, is altered by a change in inner core radius.

Differential rotation also plays an important role in the convection process. When the strength of the shear (as measured by the magnetic Reynolds num-

ber  $R_m$ ) is increased to  $O(q)$ , convection becomes inhibited. Further increasing  $R_m$  results in convection becoming increasingly localised in some region. This is apparent for all perturbation variables for  $q = 1$ , but only in the temperature perturbation for  $q = 10^{-6}$  (Fearn and Proctor 1983a,b, Fearn 1989a). The findings for our model are completely in agreement with these earlier results.

## 2.2 MODEL

### 2.2.1 Governing Equations

The model considered here is an electrically conducting fluid sphere contained within a rigid electrically insulating boundary, with a solid concentric inner sphere which is a perfect electrical conductor. For the first part of this study we choose a system internally heated by a uniform distribution,  $H$ , of heat sources. With this temperature distribution we consider both the core-mantle boundary and the inner core to be perfect thermal conductors. The system rotates with angular velocity  $\mathbf{\Omega}_0 = \Omega_0 \mathbf{1}_z$ , where  $\mathbf{1}_z$  is the unit vector in the direction of the rotation axis. In the rotating frame of reference, and with spherical polar coordinates  $(r, \theta, \phi)$  the equations describing the fluid velocity  $\mathbf{U}$ , the magnetic field  $\mathbf{B}$ , the temperature  $T$  and the pressure,  $p$ , are, in the Boussinesq approximation

$$\frac{\partial \mathbf{U}}{\partial t} + (\mathbf{U} \cdot \nabla) \mathbf{U} + 2\mathbf{\Omega}_0 \times \mathbf{U} = -\frac{1}{\rho_0} \nabla p + \nu \nabla^2 \mathbf{U} + \frac{1}{\mu \rho_0} (\nabla \times \mathbf{B}) \times \mathbf{B} + \frac{\rho}{\rho_0} \mathbf{g}, \quad (2.1)$$

$$\frac{\partial \mathbf{B}}{\partial t} = \nabla \times (\mathbf{U} \times \mathbf{B}) + \eta \nabla^2 \mathbf{B}, \quad (2.2)$$

$$\frac{\partial T}{\partial t} + (\mathbf{U} \cdot \nabla) T = \kappa \nabla^2 T + H, \quad (2.3)$$

$$\nabla \cdot \mathbf{U} = \nabla \cdot \mathbf{B} = 0. \quad (2.4, 5)$$

where  $\mathbf{g} = -g_o r / r_o \mathbf{1}_r$  is the gravitational acceleration and  $\nu, \mu, \rho_o, \eta, \kappa, r_o$  denote the kinematic viscosity, magnetic permeability, mean fluid density, magnetic diffusivity, thermal diffusivity and outer core radius, all of which are assumed constant. To complete the system we use the equation of state

$$\rho = \rho_o(1 - \alpha(T - T_o)) \quad (2.6)$$

where  $\rho$  is the fluid density,  $T_o$  is a mean temperature and  $\alpha$  is the coefficient of volume expansion.

We perform a linear stability analysis on the equations, perturbing the basic fields

$$\mathbf{B} = \mathbf{B}_o + \mathbf{b}, \quad \mathbf{U} = \mathbf{U}_o + \mathbf{u}, \quad T = T_o + \vartheta \quad (2.7)$$

where,

$$\mathbf{B}_o = B_o(r, \theta) \mathbf{1}_\phi, \quad \mathbf{U}_o = U_o(r, \theta) \mathbf{1}_\phi, \quad T_o = T_o(r) \quad (2.8)$$

are the basic fields to be prescribed, and  $\mathbf{b}, \mathbf{u}, \vartheta$  are the perturbation variables.

The mean field variables  $\mathbf{B}_o, \mathbf{U}_o$  and  $T_o$  are normalised using  $B_M = \max|B_o|$ ,  $U_M = \max|U_o|$  and  $\beta r_o$  where  $\beta = \max|\nabla T_o|$ . We non-dimensionalise the equations using the magnetic diffusion timescale  $\tau_\eta = r_o^2/\eta$ , lengthscale  $r_o$ , temperature  $\beta r_o$ , magnetic field strength  $B_M$  and velocity  $\eta/r_o$ . We also make the ‘‘magnetostrophic approximation’’ (see Fearn, Roberts and Soward 1988), omitting inertial and diffusive terms from the momentum equation, (2.1), since, for parameter values appropriate to the Earth, their contribution is negligible. The linearised equations can thus be written

$$\mathbf{1}_z \times \mathbf{u} = -\nabla p + \Lambda((\nabla \times \mathbf{B}_o) \times \mathbf{b} + (\nabla \times \mathbf{b}) \times \mathbf{B}_o) + qR\vartheta \mathbf{r}, \quad (2.9)$$

$$\frac{\partial \mathbf{b}}{\partial t} = \nabla \times (\mathbf{u} \times \mathbf{B}_0) + R_m \nabla \times (\mathbf{U}_0 \times \mathbf{b}) + \nabla^2 \mathbf{b}, \quad (2.10)$$

$$\frac{\partial \vartheta}{\partial t} + (\mathbf{u} \cdot \nabla) T_0 + R_m (\mathbf{U}_0 \cdot \nabla) \vartheta = q \nabla^2 \vartheta, \quad (2.11)$$

$$\nabla \cdot \mathbf{u} = \nabla \cdot \mathbf{b} = 0. \quad (2.12, 13)$$

The non-dimensional parameters here are the Elsasser number  $\Lambda$ , the Roberts number  $q$ , the magnetic Reynolds number  $R_m$  and a modified Rayleigh number  $R$  which are defined by

$$\begin{aligned} \Lambda &= \frac{B_M^2}{2\Omega_0 \mu \rho_0 \eta}, & q &= \frac{\kappa}{\eta}, \\ R_m &= \frac{U_M r_o}{\eta}, & R &= \frac{g \alpha \beta r_o^2}{2\Omega_0 \kappa}. \end{aligned} \quad (2.14)$$

### 2.2.2 Method of Solution

The system of equations (2.9)–(2.13) together with the boundary conditions which we employ (see Section 2.2.3) is separable in  $\phi$  and  $t$  so we make the modal expansion

$$[\mathbf{u}, \mathbf{b}, p, \vartheta] = [\mathbf{u}(r, \theta), \mathbf{b}(r, \theta), p(r, \theta), \vartheta(r, \theta)] \exp(\sigma t) \exp(im\phi) \quad (2.15)$$

We are left with a system of coupled two-dimensional partial differential equations in  $r$  and  $\theta$ . We split  $\mathbf{b}$ ,  $\mathbf{u}$  into components, writing

$$\mathbf{b} = (b_r, b_\theta, b_\phi), \quad \mathbf{u} = (u_r, u_\theta, u_\phi). \quad (2.16)$$

Equation (2.13) is not independent of the magnetic induction equation (2.10), but we use this divergence relation in preference to the  $\phi$ -component of the induction equation which is more complicated. Using (2.12), (2.13) and  $1_\phi \cdot (2.9)$  we eliminate  $u_\phi, b_\phi$  and the pressure  $p$  respectively. There is no boundary condition on  $u_\theta$ , so we remove the  $\frac{\partial u_r}{\partial r}$  term occurring in the  $r$ -component of (2.10) by using  $\frac{\partial}{\partial r}[1_\theta \cdot (2.9)]$ . We can further simplify the system, by eliminating  $u_\theta$  using the  $\theta$ -component of (2.9), which leaves us with four coupled partial differential equations in  $u_r, b_r, b_\theta$  and  $\vartheta$ .

We then discretise the equations replacing the differential operators with second-order finite-difference approximations. We have  $N$  grid points in the  $r$ -direction and  $L$  in the  $\theta$ -direction. The system of equations has now been transformed to a matrix eigenvalue problem of the form

$$\mathbf{A}\mathbf{x} = \lambda\mathbf{B}\mathbf{x} \quad (2.17)$$

where  $\mathbf{A}, \mathbf{B}$  are the matrices formed from the finite difference equations, and

$$\mathbf{x} = (\mathbf{v}^{1,1}, \dots, \mathbf{v}^{1,L-1}, \dots, \mathbf{v}^{N-1,1}, \dots, \mathbf{v}^{N-1,L-1}), \quad (2.18)$$

where

$$\mathbf{v}^{i,j} = (u_r^{i,j}, b_r^{i,j}, b_\theta^{i,j}, \vartheta^{i,j}) \quad (2.19)$$

The eigenvalue problem was solved by two methods. Firstly the LR algorithm [Peters and Wilkinson (1971a)] was used on the system with the variable  $u_r$  eliminated. This reduces the system to a problem of the form  $\mathbf{C}\mathbf{y} = \lambda\mathbf{y}$ . The LR algorithm finds all the eigenvalues of the system, but requires a large amount of storage and CPU time so is limited to a low numerical resolution. To determine the eigenvalues at higher resolution we then use the method of inverse iteration [Peters and Wilkinson (1971b), Fearn (1991)]. This method requires an initial estimate for the eigenvalue, and we use the eigenvalue corresponding to

the most unstable mode found at low resolution by LR. Inverse iteration outputs the eigenvalue closest to the input guess and its corresponding eigenvector. Our finite-difference matrices are banded in structure, and the method of inverse iteration can take advantage of this to reduce storage and CPU time, and allow a much higher numerical resolution.

### 2.2.3 Boundary conditions

If we assume that the basic magnetic field is either symmetric, ( $B = 0$ ), or antisymmetric, ( $B = 1$ ), then the problem splits into two parities of solution, namely Dipole ( $b_r$  antisymmetric,  $b_\theta$  symmetric,  $u_r B_0$  and  $\vartheta B_0$  antisymmetric), and Quadrupole ( $b_r$  symmetric,  $b_\theta$  antisymmetric,  $u_r B_0$  and  $\vartheta B_0$  symmetric). We need only to solve the problem then in the region  $r_{ib} < r < 1$ ,  $0 < \theta < \pi/2$ , provided that we satisfy the following boundary conditions.

(a)  $\theta = \frac{\pi}{2}$

$$\begin{array}{l}
 \text{DIPOLE :} \quad b_r = \frac{\partial b_\theta}{\partial \theta} = 0 \quad \left\{ \begin{array}{l} \frac{\partial u_r}{\partial \theta} = \frac{\partial \vartheta}{\partial \theta} = 0 \quad (B = 0) \\ u_r = \vartheta = 0 \quad (B = 1) \end{array} \right. \\
 \\
 \text{QUADRUPOLE :} \quad \frac{\partial b_r}{\partial \theta} = b_\theta = 0 \quad \left\{ \begin{array}{l} u_r = \vartheta = 0 \quad (B = 0) \\ \frac{\partial u_r}{\partial \theta} = \frac{\partial \vartheta}{\partial \theta} = 0 \quad (B = 1) \end{array} \right.
 \end{array} \quad (2.20)$$

We also require the following boundary conditions at  $\theta = 0$ ,  $r = r_{ib}$  and  $r = 1$ .

(b)  $\theta = 0$

$$\begin{array}{l}
 b_r = \frac{\partial b_\theta}{\partial \theta} = u_r = \vartheta = 0 \quad (m = 1) \\
 \\
 b_r = b_\theta = u_r = \vartheta = 0 \quad (m > 1)
 \end{array} \quad (2.21)$$

(c)  $r = 1$

$$\mathbf{b} = \mathbf{b}^{\text{ex}}, \quad \mathbf{u} \cdot \mathbf{1}_r = 0, \quad \vartheta = 0. \quad (2.22)$$

where  $\mathbf{b}^{\text{ex}}$  is an external potential field.

(d)  $r = r_{ib}$

(i)  $r_{ib} = 0$

$m > 1$  :

$$b_r = b_\theta = u_r = \vartheta = 0 \quad (2.23)$$

$m = 1$  :

$$\vartheta = 0 \quad (\text{both parities}), \quad (2.24)$$

$$\begin{array}{l} \text{DIPOLE :} \\ \text{QUADRUPOLE :} \end{array} \quad \begin{array}{l} b_r = b_\theta = 0 \\ b_r, b_\theta \text{ constant} \end{array} \quad \left\{ \begin{array}{ll} u_r \text{ constant} & (B = 0) \\ u_r = 0 & (B = 1) \end{array} \right. \quad \left\{ \begin{array}{ll} u_r = 0 & (B = 0) \\ u_r \text{ constant} & (B = 1) \end{array} \right. \quad (2.25)$$

(ii)  $r_{ib} > 0$

$$b_r = u_r = \vartheta = 0, \quad \frac{\partial}{\partial r}(rb_\theta) = 0. \quad (2.26)$$

## 2.2.4 Choice of temperature distribution

Our choice of temperature distribution must satisfy the heat conduction equation

$$\frac{\partial T}{\partial t} + (\mathbf{U} \cdot \nabla)T = \kappa \nabla^2 T + H \quad (2.27)$$

If we choose  $\mathbf{U} = U(r, \theta)\mathbf{1}_\phi$ ,  $T = T(r)$  then this equation has solution

$$T = -\frac{A}{r} - \frac{H}{6\kappa}r^2 + B \quad (2.28)$$

where  $A$  and  $B$  are arbitrary constants to be determined by the boundary conditions. To allow  $r_{ib} = 0$ , we require that  $A = 0$ , and by specifying  $T$  at  $r = 1$  we determine  $B$ . We produce a temperature gradient

$$\frac{dT}{dr} = -\frac{H}{3\kappa}r \quad (2.29)$$

and this represents a temperature distribution as would be produced by a uniform distribution of heat sources for a full sphere ( $r_{ib} = 0$ ).

If we have a non-zero inner boundary radius, then to allow comparison with the  $r_{ib} = 0$  case we want to have the same temperature gradient. In addition to the uniform heating  $H$ , we require differential heating between the inner and outer core boundaries. By doing this we can make  $A = 0$  and keep the same gradient as before.

## 2.3 NUMERICAL RESULTS

### 2.3.1 Finding unstable modes.

In the course of this chapter we are mainly interested in finding the most unstable mode of solution (i.e., the mode with the lowest critical Rayleigh number  $R_c$ ), for particular choices of the parameters, but we also look at the higher modes when required, as we find that the order of modes can be altered as we change

the parameters. In order to find these modes, we first use the LR algorithm with a specified Rayleigh number  $R$ . This finds all the eigenvalues, although limited in resolution to a maximum of  $N = L = 16$  grid points. If an eigenvalue is found with a positive growth rate, then this corresponds to a mode which is unstable for the chosen value of  $R$ . If none are found then  $R$  is increased and we repeat the process. When we have found the eigenvalue corresponding to the most unstable mode according to LR, we then input this value as the required initial estimate for the Inverse Iteration method, which produces one eigenvalue and its corresponding eigenvector at a higher numerical truncation. Having found the most unstable mode at the specified Rayleigh number  $R$ , we then iterate from this to find the point of marginal stability where the growth rate is zero, and obtain the critical Rayleigh number for the mode.

### 2.3.2 Initialisation

In order to solve our problem we must prescribe the basic field and flow, and values for some of the parameters. Initially we choose

$$\mathbf{B}_0 = 8r^2(1 - r^2) \sin \theta \cos \theta \mathbf{1}_\phi, \quad \mathbf{U}_0 = 0. \quad (2.30)$$

This choice allows us to make comparisons with previous work of Fearn and Proctor (1983a) on a model without an inner sphere, and this provides an essential check for the numerical code used here, as we can compare our calculations for a zero inner boundary radius, ( $r_{ib} = 0$ ), with their results. In this section we choose our basic temperature distribution to be that of a uniform distribution of heat sources in the core (see Section 2.2.4), the distribution used in previous studies of convection in a sphere ( Fearn and Proctor 1983a, Roberts 1968, Eltayeb and Kumar 1977).

We initially choose  $q = 10^{-6}$  since this is a good approximation for the molecular diffusivity ratio of the Earth, and consider only the case when the azimuthal wave number  $m = 2$ . For the domain of magnetic field strengths that we are interested in [ $\Lambda = O(1-10)$ ], the most unstable mode occurs for azimuthal

wave number  $m = 1$ . However when  $m = 1$ , there can be interference from magnetically driven instabilities (Fearn and Weiglhofer 1991a,b). These magnetic instabilities occur for magnetic field strengths above a certain critical value  $\Lambda_c$ , which is dependent on the azimuthal wave number  $m$ . By choosing  $m = 2$ , we find that  $\Lambda_c$  becomes higher than the values of  $\Lambda$  considered here, and so we can avoid the magnetically driven instabilities and concentrate on the thermal instabilities which are the subject of this study.

### 2.3.3 Plotting the eigenfunctions

Our model produces the eigenfunctions of the perturbation variables, namely  $b_r, b_\theta, u_r, u_\theta$  and  $\vartheta$ . These variables are normalised such that  $b_r(r = 1, \theta = \frac{\pi}{2}) = 1$  with quadrupole parity of solution, or  $b_\theta(r = 1, \theta = \frac{\pi}{2}) = 1$  with dipole parity, and then split into real and imaginary parts. This normalisation can occasionally lead to problems as we follow the same mode of solution while changing the parameters, in that the sign of the variables can be reversed from one picture to the next. This is not a common problem though, and is easily dealt with. The eigenfunction solutions that we obtain are with respect to an  $r, \theta$ -grid. We must first interpolate into a regular rectangular grid, before plotting the eigenfunctions as contour maps.

### 2.3.4 Comparison with Fearn and Proctor (1983a)

We can check our numerical code by comparing our results from our model with an inner boundary radius  $r_{ib} = 0$  with the calculations of Fearn and Proctor (1983a) who considered the same problem but without an inner core. As an example we illustrate the eigenfunctions for the most unstable mode with field (2.30),  $q = 10^{-6}$ , azimuthal wave number  $m = 2$ , magnetic field strength  $\Lambda = 1$  and with the quadrupole parity of solution (see Section 2.2.3), in Figure 2.1. This corresponds to Figure 3 of Fearn and Proctor (1983a). We find good agreement between the two models.

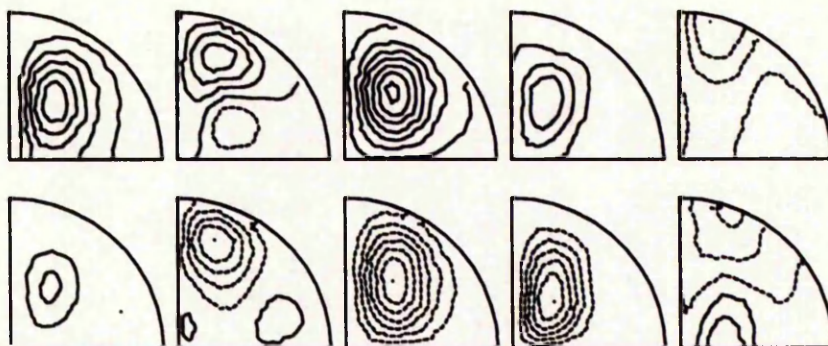


Figure 2.1: Contour plots of the eigenfunctions of the most unstable mode with zero inner boundary radius,  $q = 10^{-6}$ ,  $m = 2$ ,  $\Lambda = 1$ , basic state (2.30) and quadrupole parity of solution. The truncation here is  $N = L = 20$ . These eigenfunctions are from left to right  $b_r, b_\theta, v, u_r$ , and  $u_\theta$  with real parts on the top row and imaginary parts on the bottom.  $R_c$  here is 316.711.

### 2.3.5 Convergence of Solutions

To check that the modes that we find are well resolved, we check the convergence with increasing truncation. We show graphs of the convergence of critical Rayleigh number and critical frequency with increasing number of grid points for basic state (2.30),  $r_{ib} = 0$ ,  $\Lambda = 1$ ,  $q = 10^{-6}$ ,  $m = 2$  in Figure 2.2 (with dipole parity of solution) and Figure 2.3 (with quadrupole parity). These show that for a truncation of  $N = L = 20$  the solution is well resolved. This together with the clarity of the eigenfunctions, gives us confidence in our results at this resolution. Hence for all results in this chapter, we use a truncation of  $N = L = 20$ .

### 2.3.6 Variation of $R_c$ with $r_{ib}$

The first case that we consider is the effect on the solution of varying the inner boundary radius. We initially choose a magnetic field strength,  $\Lambda = 1$  with the quadrupole parity of solution. We then look for the onset of convection for a zero inner boundary radius. The three most unstable modes were found and their progress followed as the inner boundary radius,  $r_{ib}$ , was gradually increased. The effect of this increase on the critical Rayleigh number,  $R_c$ , is shown in Figure 2.4. At first, increasing  $r_{ib}$  reduces  $R_c$  very slightly, but after a minimum is reached there is a continual increase which, after  $r_{ib}$  reaches  $\sim 0.5$ , becomes very rapid. The behaviour of the three modes is very similar, although mode 1, which is initially the most unstable mode, becomes strongly inhibited well before the other two modes do. Indeed the most unstable mode for  $r_{ib} \gtrsim 0.5$  is mode 2.

The eigenfunctions of  $b_r$ , the radial component of  $\mathbf{b}$ , for the three modes are shown in Figure 2.5. These are characteristic of the eigenfunctions of the other perturbation variables. The eigenfunctions for each mode show differing behaviours as  $r_{ib}$  is increased. Mode 1 shows a tendency for convection to move towards  $\theta = \pi/2$ , whereas mode 2 shows a preference towards  $\theta = 0$  at higher  $r_{ib}$  values. Clearly mode 1 is becoming quite restricted by the inner boundary growth when  $r_{ib} = 0.3$ , whereas mode 2 is still relatively uninhibited by this point. This is a likely reason why mode 2 becomes the preferred mode at  $r_{ib} \sim 0.5$ .

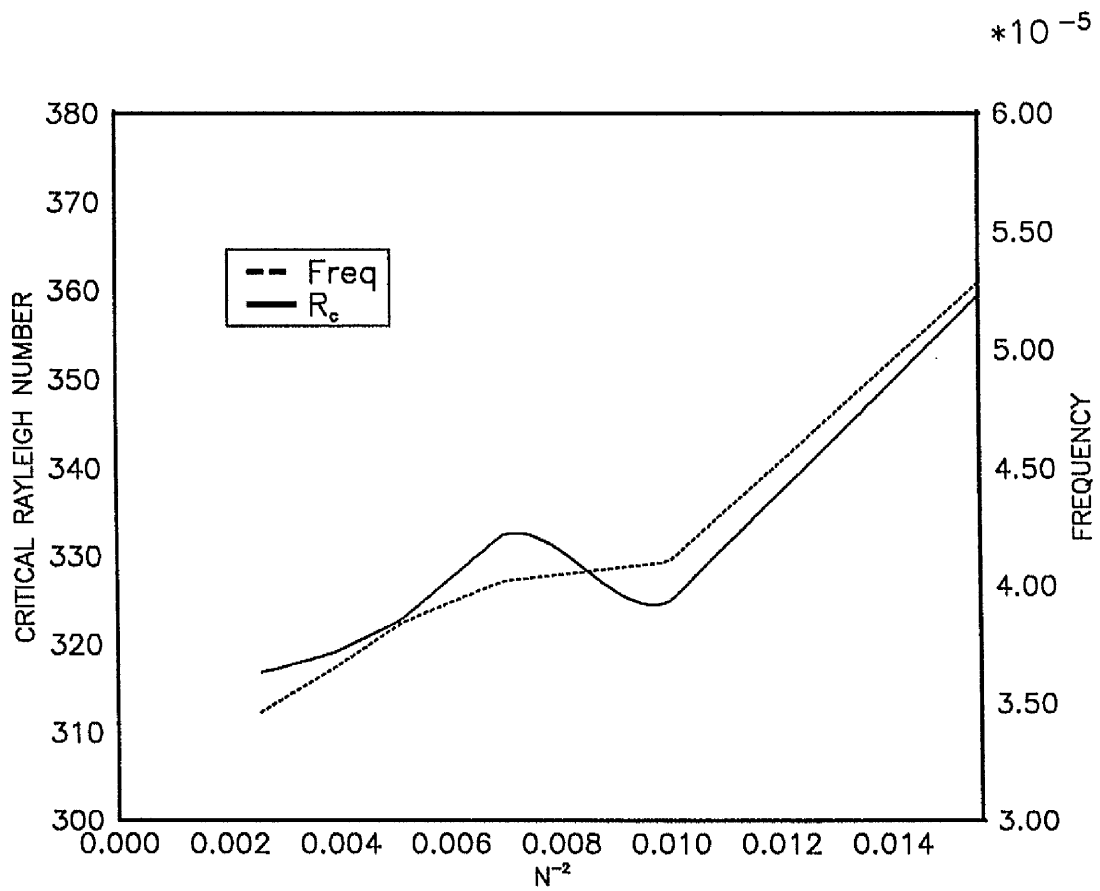


Figure 2.2: Graph of the convergence of  $R_c$  and critical frequency with the number of grid points. This is for basic state (2.30),  $r_{ib} = 0$ ,  $\Lambda = 1$ ,  $m = 2$ ,  $q = 10^{-6}$  and quadrupole parity.

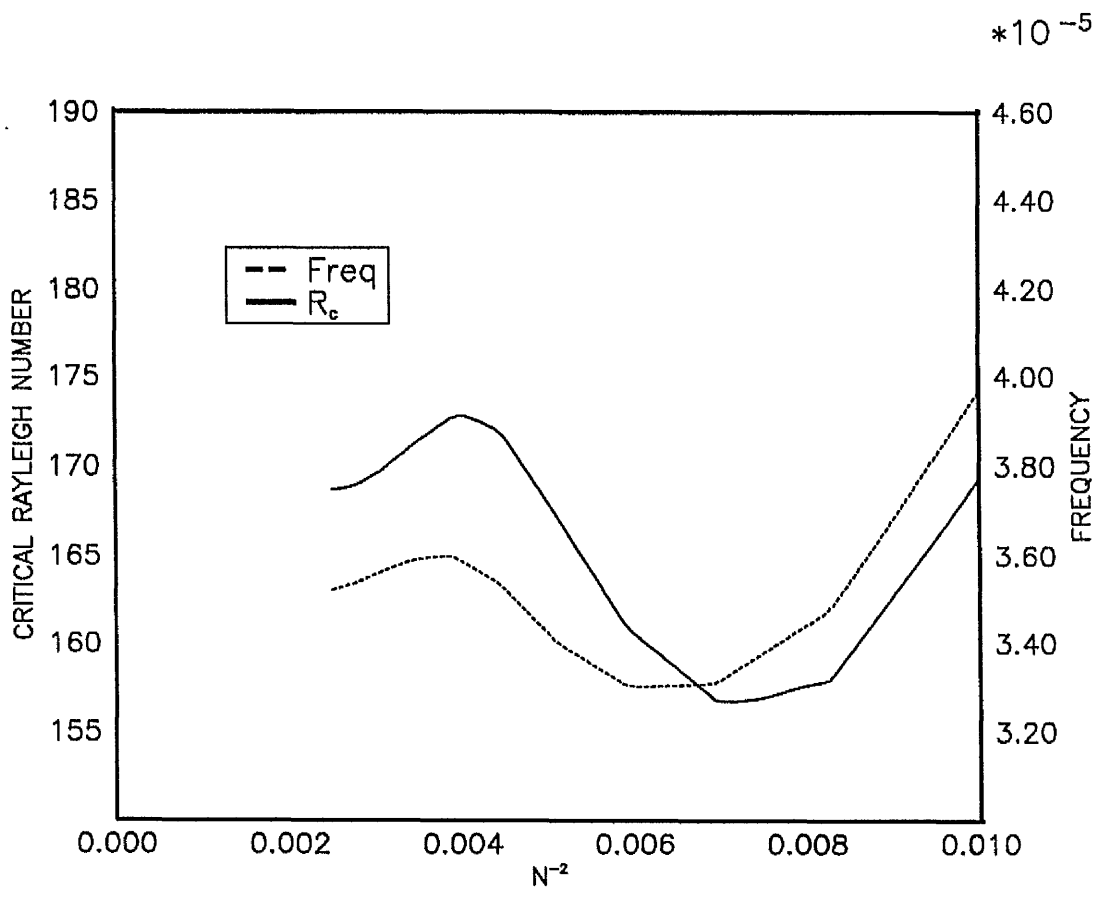


Figure 2.3: As Figure 2.2 but with dipole parity.

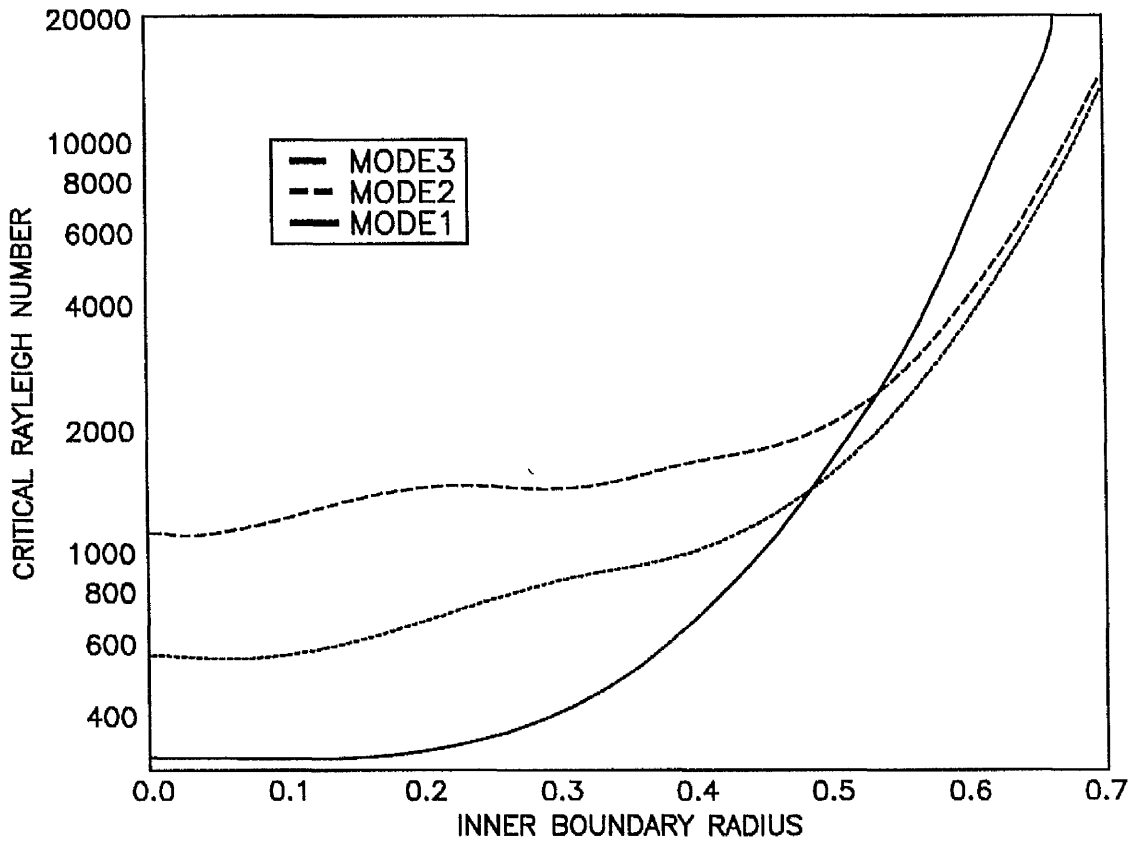


Figure 2.4: Graph of  $R_c$  against  $r_{ib}$  for the three most unstable modes with  $\Lambda = 1, m = 2, q = 10^{-6}$  and quadrupole parity.

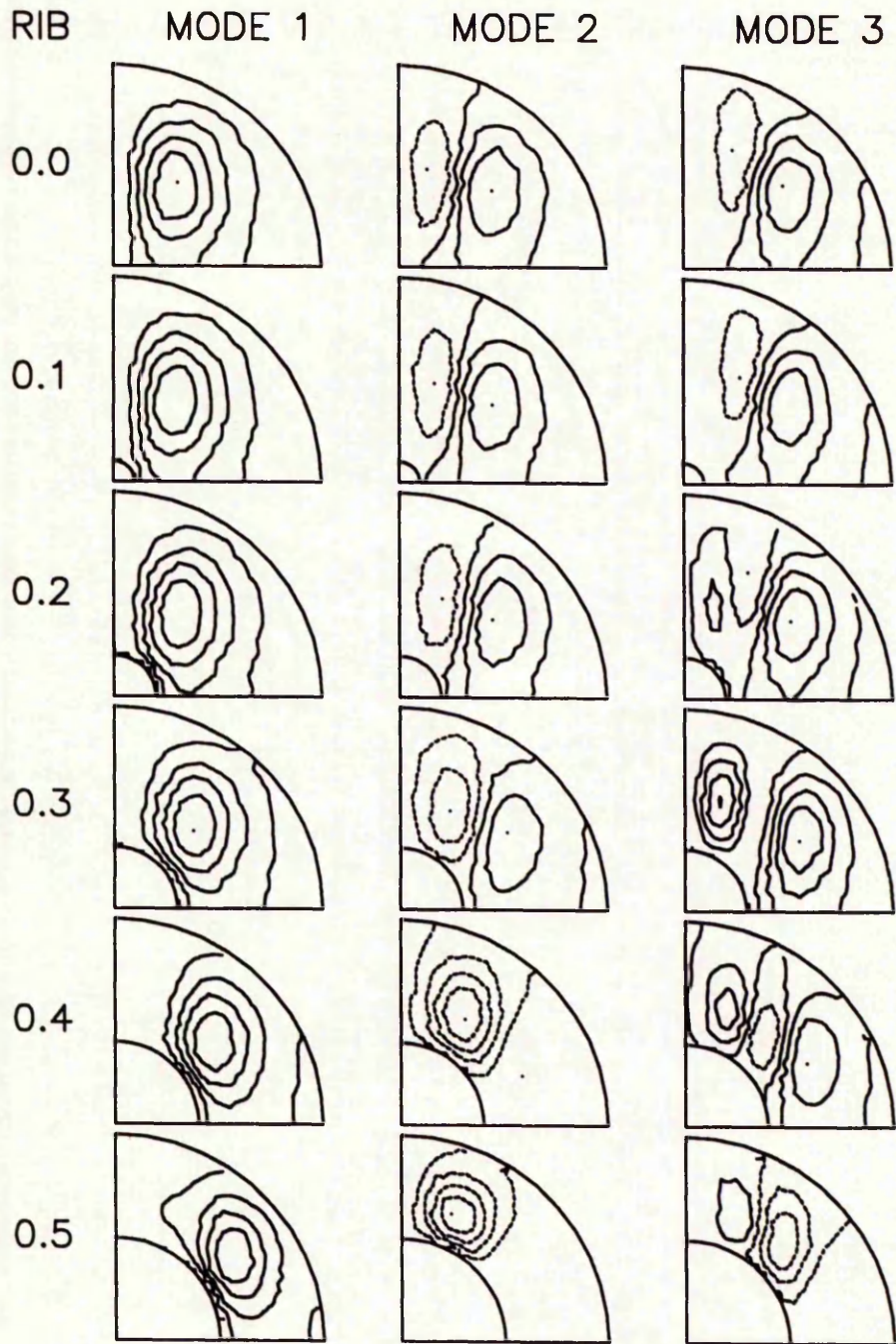


Figure 2.5: Eigenfunctions of the real part of  $b_r$  for the three modes of Figure 2.4.

The third mode is a shorter lengthscale mode. It, too, is not very restricted at  $r_{ib} = 0.3$  and it also becomes more unstable than mode 1, but remains more stable than mode 2.

Repeating the above with a higher magnetic field strength,  $\Lambda = 10$ , produced similar results. As before the three most unstable modes were found and followed as  $r_{ib}$  was increased from zero. The relationship between  $R_c$  and  $r_{ib}$  is shown, for this case, in Figure 2.6. This picture is very similar to Figure 1. Again there is a small initial decrease in  $R_c$  followed by an increase which becomes marked after  $r_{ib}$  reaches 0.5. The third mode shows a kink which is probably due to a change to another mode. This was investigated by trying to separate the two, but it was not possible to resolve. The decrease in  $R_c$  is much more noticeable for the higher magnetic field strength, and this is explained in Section 2.3.7. The eigenfunctions (Figure 2.7) also exhibit the behaviour seen before, and mode 1 is again superseded by the other two modes, although at a higher value of  $r_{ib}$  than before ( $\sim 0.6$  as compared with  $\sim 0.5$ ).

The magnetic field strengths  $\Lambda = 1, 10$  used in these calculations were chosen because they may be representative of the Earth's field. Field strengths higher than these were not considered because we would then be entering the domain of magnetic instabilities which could confuse the picture.

### 2.3.7 Variation of $R_c$ with $\Lambda$

Using the three modes found for  $\Lambda = 1$ , quadrupole parity in Section 2.3.6 as a starting point,  $\Lambda$  was increased gradually from 1 to 10 for constant values of  $r_{ib}$  of 0, 0.1, ..., 0.5. The variation of  $R_c$  with  $\Lambda$  is shown, for mode 1, in Figure 2.8. This picture shows some interesting behaviour. The general tendency observed is for  $R_c$  to fall to a minimum and then increase, which is consistent with the expected minimum for  $\Lambda = O(1)$  (see Fearn, Roberts and Soward 1988). However, it is the variation of this behaviour with  $r_{ib}$  which is of most interest. Initially, when  $\Lambda = 1$ , it is the lower  $r_{ib}$  values which are preferred, with  $R_c$  increasing as  $r_{ib}$  increases. As we increase  $\Lambda$ , though, higher values of  $r_{ib}$  become optimal, as

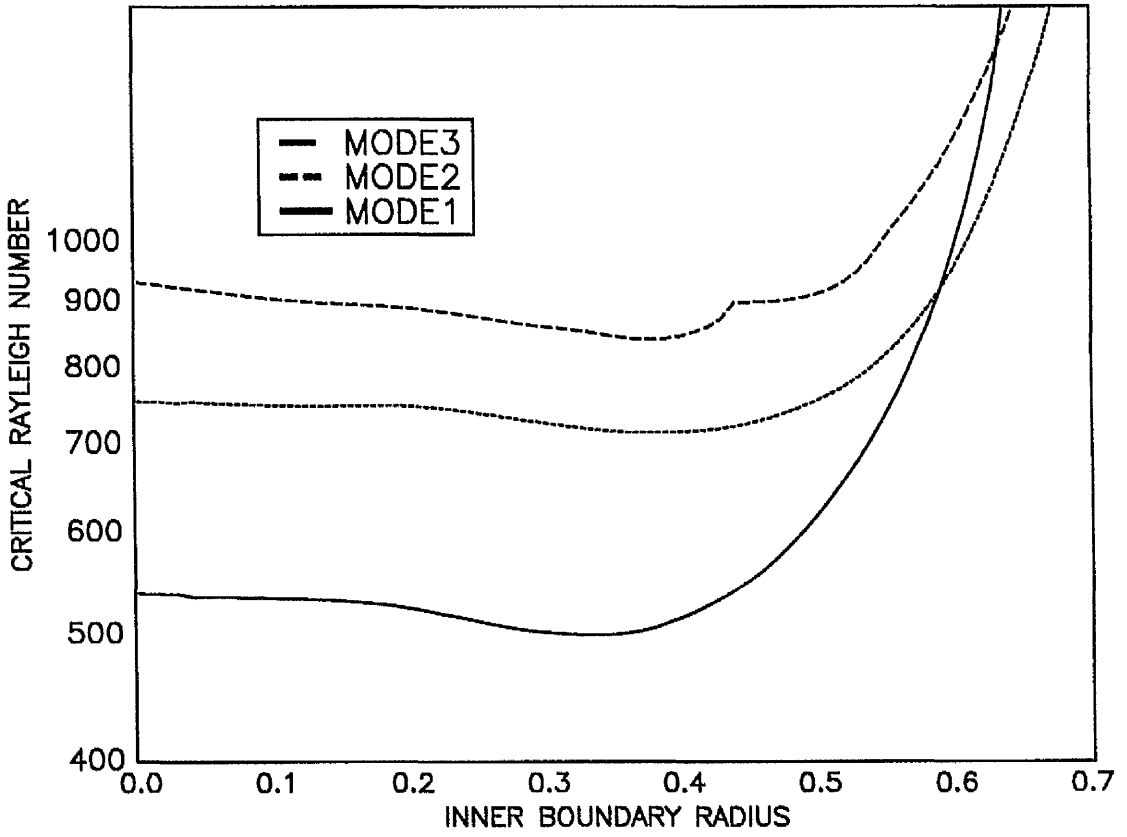


Figure 2.6: As Figure 2.4 but with  $\Lambda = 10$ .

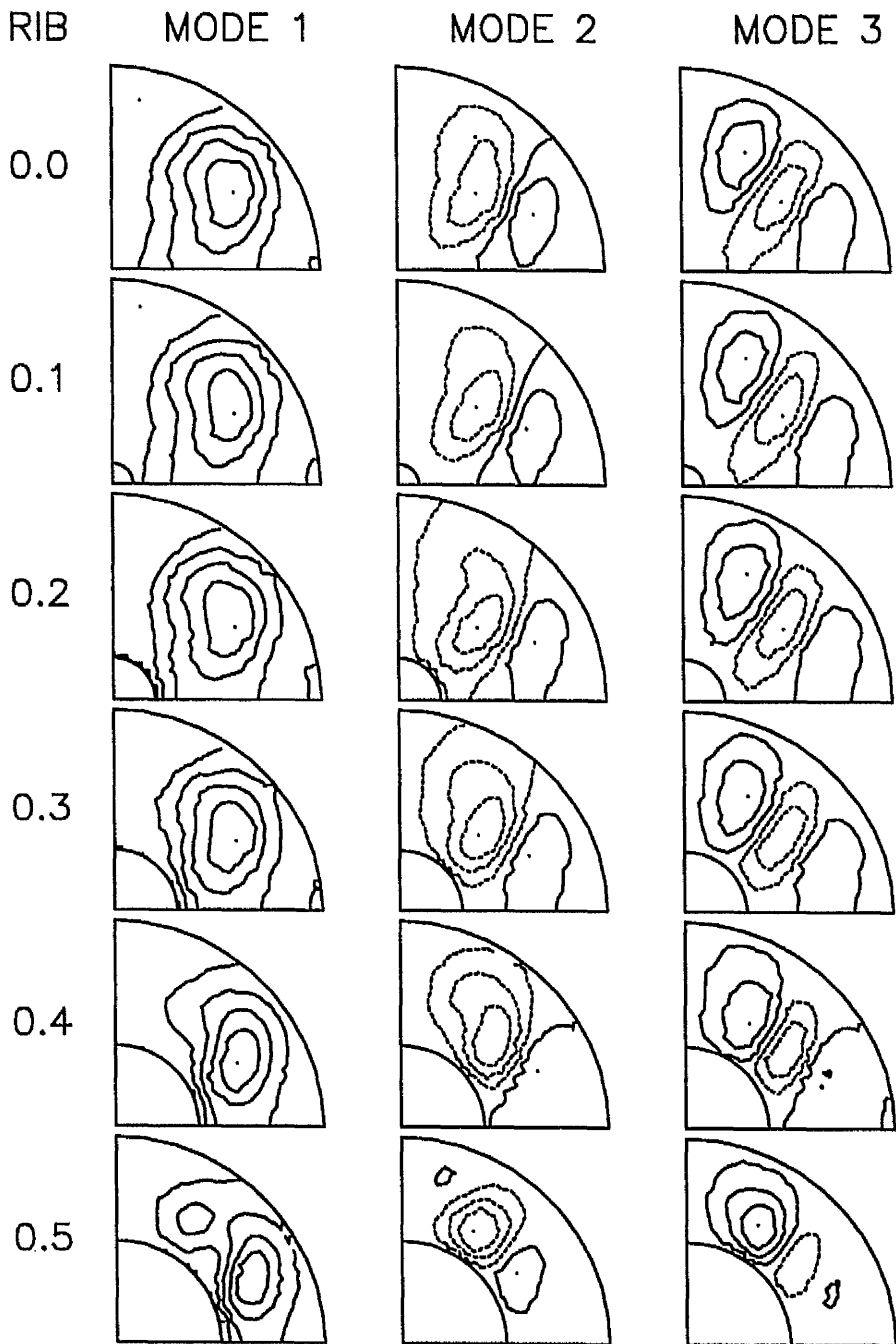


Figure 2.7: Eigenfunctions of the real part of  $b_r$  for the three modes of Figure 2.6.

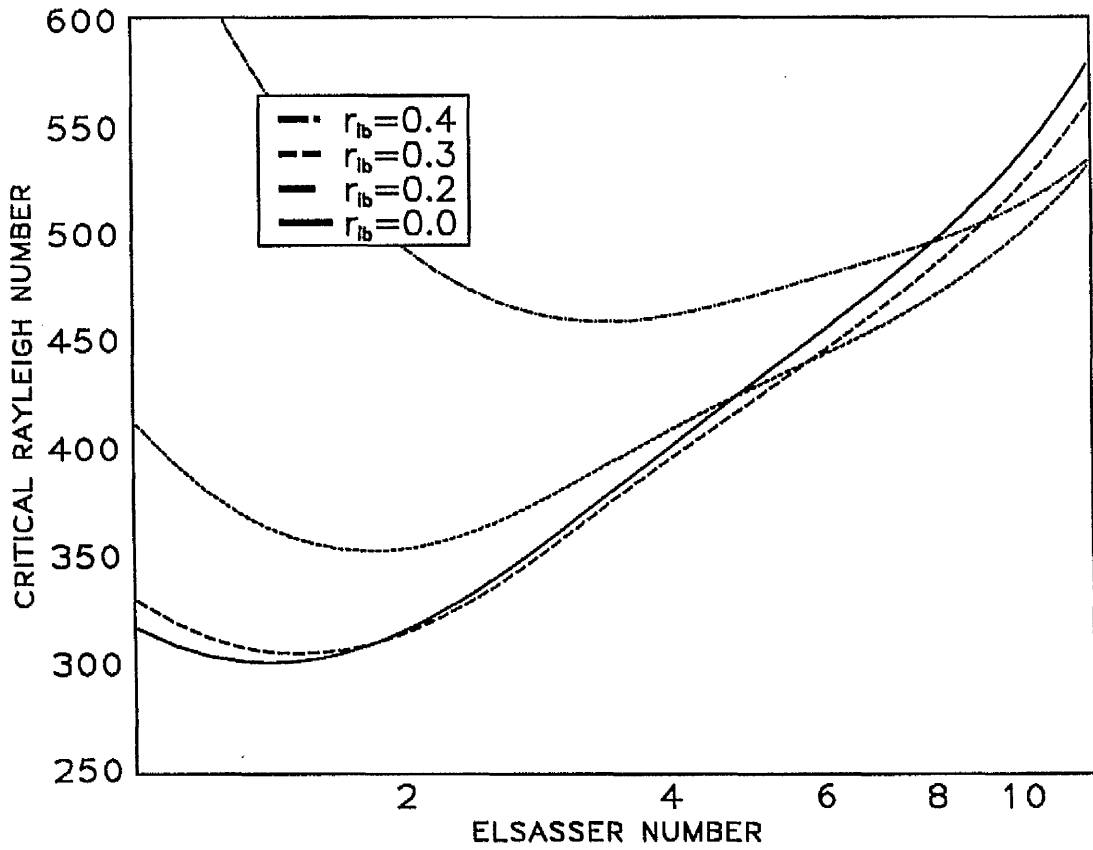


Figure 2.8: Variation of  $R_c$  with  $\Lambda$  of the most unstable mode for  $m = 2, q = 10^{-6}$  and quadrupole parity at different values of  $r_{ib}$ .

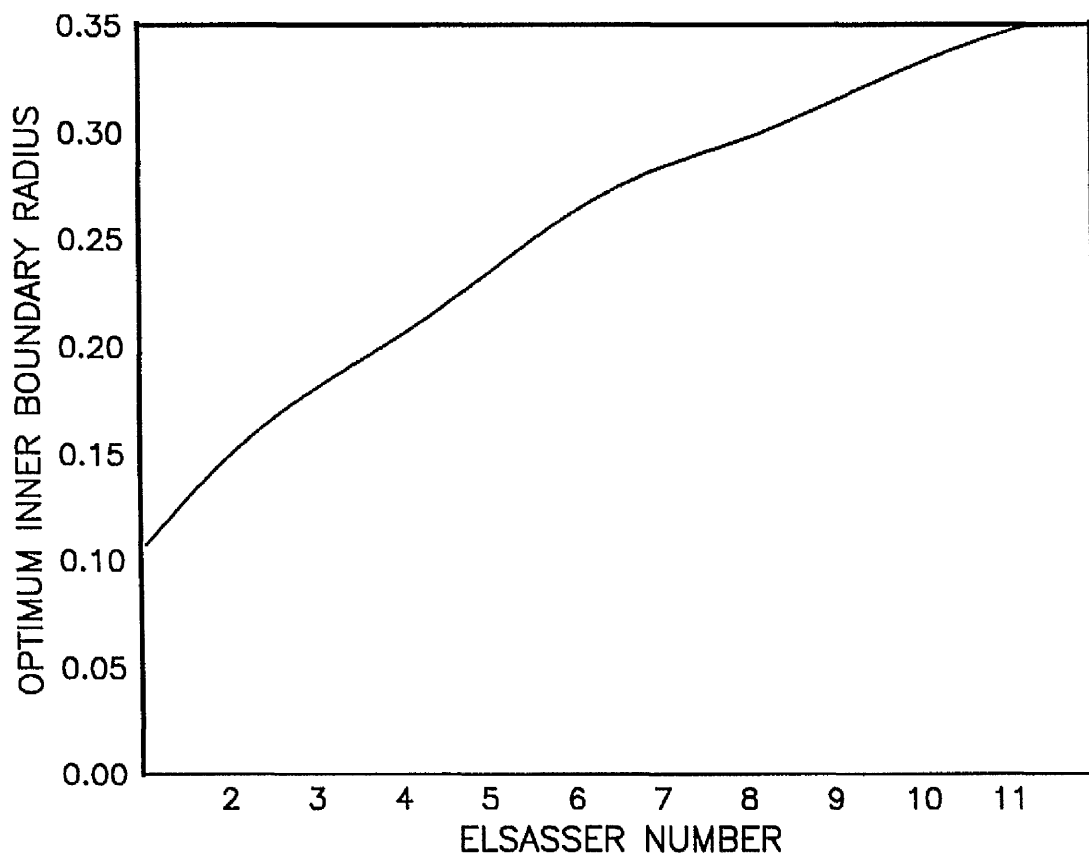


Figure 2.9: Optimum  $r_{ib}$  versus  $\Lambda$  for the mode of Figure 2.8.

shown in Figure 2.9. This explains why the initial decrease in  $R_c$  in Figure 2.6 is more evident than in Figure 1, as with higher field strength  $\Lambda = 10$ ,  $r_{ib}$  can be increased to a greater extent before convection is inhibited.

The eigenfunctions, in this case, show a tendency to move away from the rotation axis  $\theta = 0$  as  $\Lambda$  is increased. This can be seen by comparing the respective eigenfunctions in Figures 2.5 and 2.7. This also allows  $r_{ib}$  to be increased more before inhibiting convection, further explaining the stronger initial decrease of  $R_c$  with  $r_{ib}$  for  $\Lambda = 10$ .

### 2.3.8 Dipole parity

If we repeat the calculations performed previously, but with dipole parity we find similar behaviour, although at slightly higher magnetic field strength. Here we consider  $\Lambda$  values between 10 and 30. As earlier we look for the onset of convection for a zero inner boundary radius, and follow the modes as the inner boundary radius,  $r_{ib}$  is gradually increased. The variation of  $R_c$  with  $\Lambda$  for the most unstable modes for  $\Lambda = 10$  and  $\Lambda = 30$  is shown in Figure 2.10. As for the quadrupole parity case, we first see a slight decrease in  $R_c$  as  $r_{ib}$  is increased, with this decrease being more noticeable for higher  $\Lambda$ . When  $r_{ib}$  becomes large ( $\sim 0.5-0.6$ ),  $R_c$  increases rapidly with any further increase in  $r_{ib}$ . Figure 2.11 shows eigenfunctions of the real part of  $b_r$  for  $\Lambda = 10$  and  $\Lambda = 30$ . The behaviour of the other eigenfunctions is similar. Initially, as  $r_{ib}$  is increased there is little effect on the eigenfunctions, but when  $r_{ib}$  becomes large the modes are becoming quite restricted, which explains (as with the quadrupole parity) why  $R_c$  increases rapidly with  $r_{ib}$  here. Comparing the  $\Lambda = 10$  and  $\Lambda = 30$  eigenfunctions, we see that increasing the magnetic field strength has caused the eigenfunctions to move away from  $\theta = 0$  and towards  $\theta = \frac{\pi}{2}$ . As we suggested for the quadrupole case, this means  $r_{ib}$  can be increased to greater values before convection is restricted, explaining why the initial decrease of  $R_c$  with  $r_{ib}$  is more pronounced at higher  $\Lambda$ .

The main reason why we are looking at higher  $\Lambda$  values here than for the

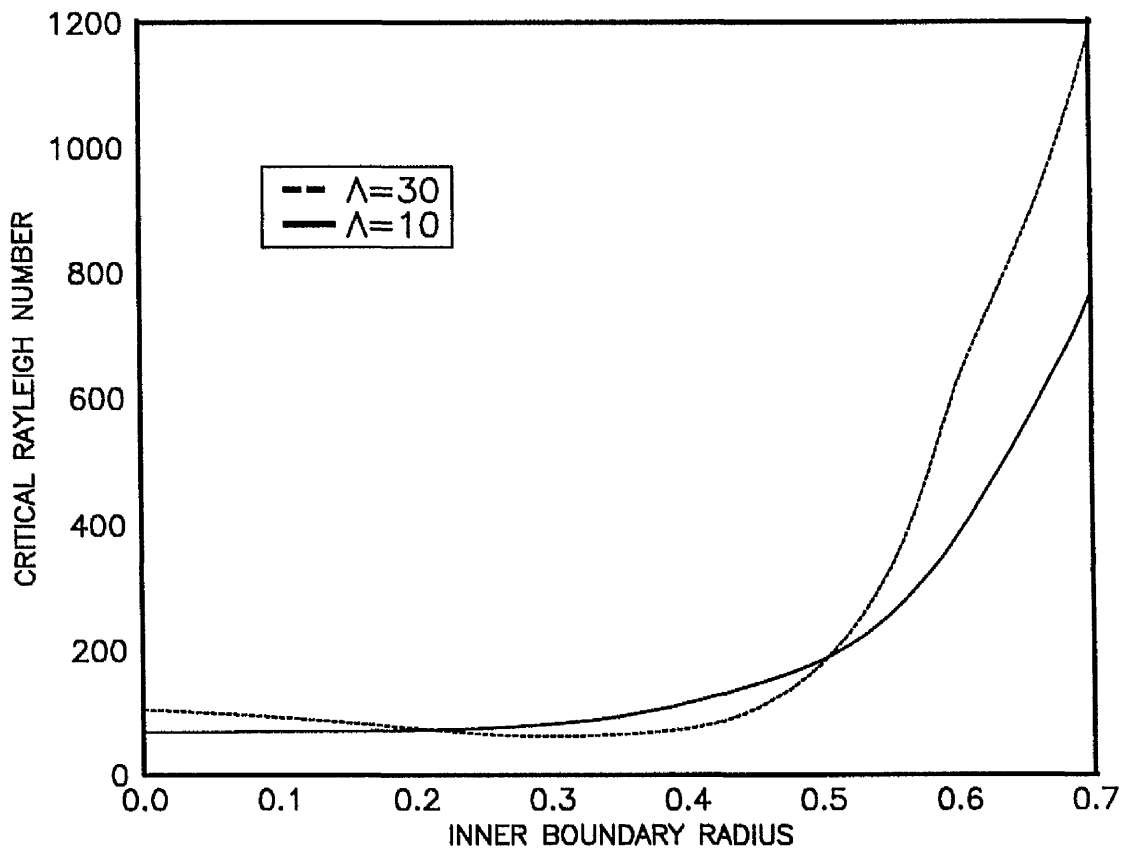


Figure 2.10: Graph of  $R_c$  against  $r_{ib}$  for the most unstable modes with  $m = 2$ ,  $q = 10^{-6}$  and dipole parity for both  $\Lambda = 10$  and  $\Lambda = 30$ .

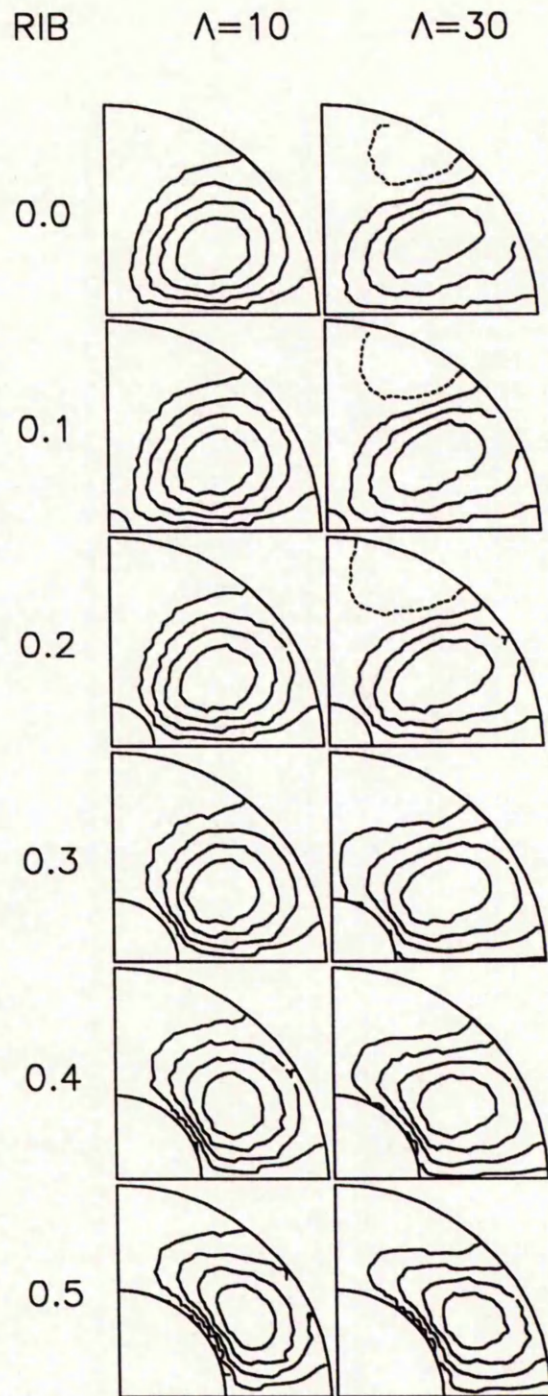


Figure 2.11: Eigenfunctions of the real part of  $b_r$ , for the modes of Figure 2.10.

quadrupole parity, is that the minimum turning point in the graph of  $R_c$  versus  $\Lambda$  occurs here for  $\Lambda = O(20)$  as opposed to  $\Lambda = O(2)$  in the quadrupole case. As in Figure 2.8, we find that the position of this minimum changes with  $r_{ib}$ . Figure 2.12 shows the variation of  $R_c$  with  $\Lambda$  for different constant values of  $r_{ib}$ . When  $\Lambda = 10$  we find that the lowest  $r_{ib}$  values have the lowest  $R_c$ , with  $R_c$  increasing with  $r_{ib}$ . As  $\Lambda$  is increased, however, higher values of  $r_{ib}$  become preferred as is shown in Figure 2.13. This is the same behaviour we found with the quadrupole parity.

With dipole parity, the higher modes were sometimes found to be slightly erratic and difficult to follow, but they were never found to become the preferred mode. All the results in this section were for the most unstable mode which behaved as expected.

### 2.3.9 Effect of changing basic state $B_0$

Although a good choice for comparison with previous work, the basic field, (2.30), considered thus far does not satisfy the boundary condition

$$\frac{\partial}{\partial r}(rB_\phi) = 0 \quad (r = r_{ib}). \quad (2.31)$$

when  $r_{ib} \neq 0$ , which is the appropriate boundary condition to apply at the boundary between the outer core and a perfectly conducting inner core. In order to determine whether or not this was affecting the results, a similar field was chosen which does satisfy the boundary condition,

$$B_0 = \frac{2}{C}(r - r_{ib})^2(1 - r^2) \sin \theta \cos \theta \mathbf{1}_\phi. \quad (2.32)$$

where

$$C = ((r_{ib} + (r_{ib}^2 + 8)^{1/2})/4 - r_{ib})^2(1 - (r_{ib} + (r_{ib}^2 + 8)^{1/2})^2/16), \quad (2.33)$$

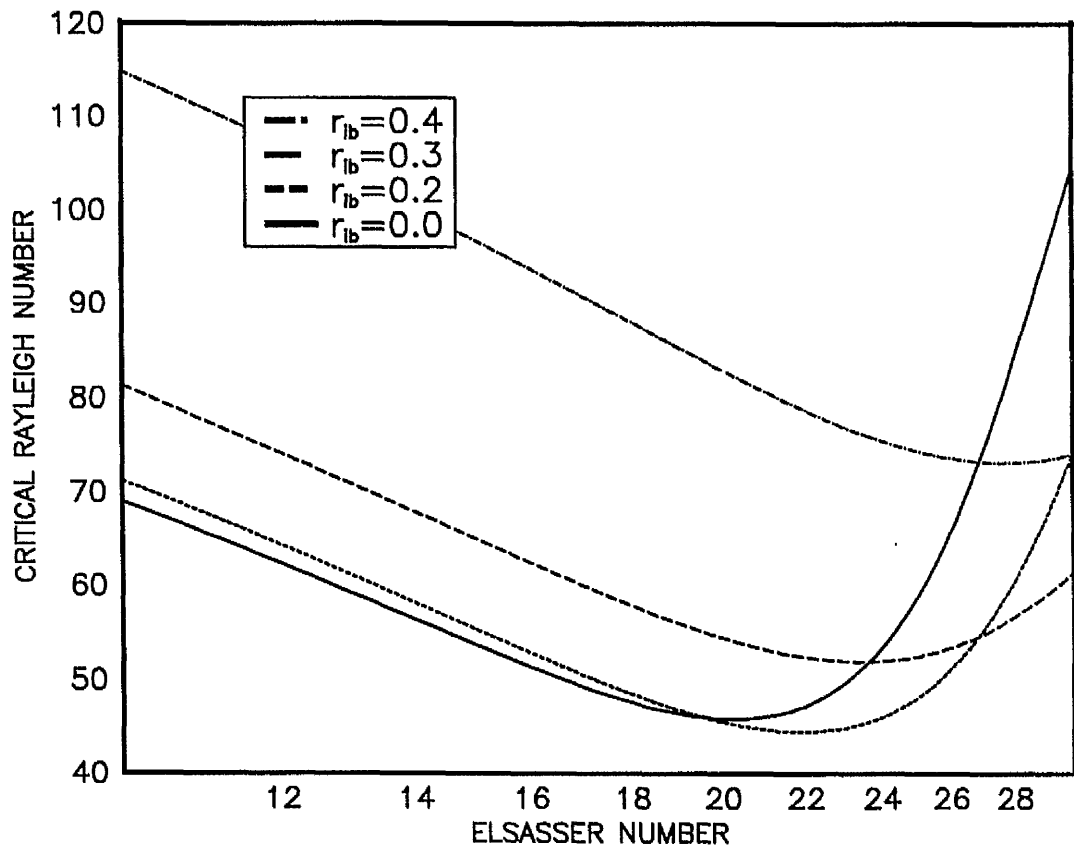


Figure 2.12: As Figure 2.8 but with dipole parity.

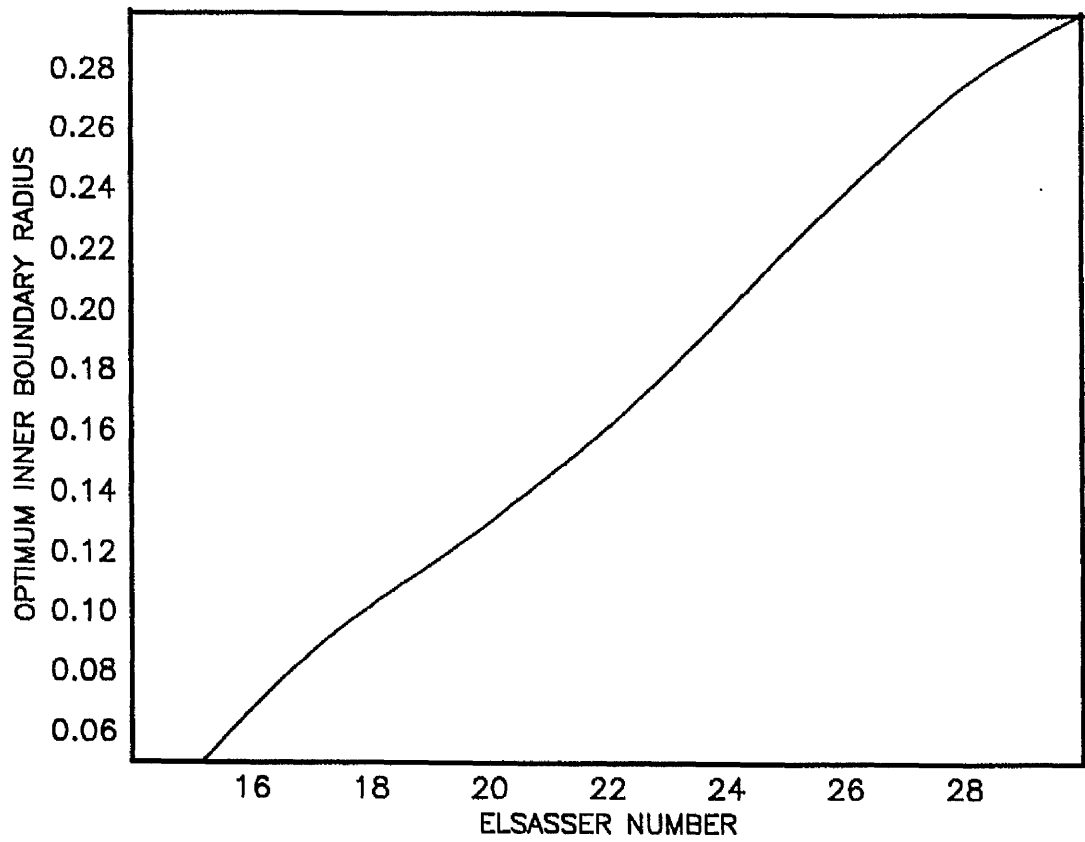


Figure 2.13: Optimum  $r_{ib}$  against  $\Lambda$  for the mode of Figure 2.12.

was chosen to normalise the field to have maximum value 1. This field reduces to (2.30) when  $r_{ib} = 0$ .

Calculations were performed as before and the results obtained with this field exhibited the same trends as the original field (2.30). We looked for the three most unstable modes with a non-zero inner boundary radius for  $m = 2$ ,  $q = 10^{-6}$  and quadrupole parity. The effect of increasing  $r_{ib}$  on  $R_c$  is graphed in Figure 2.14 for  $\Lambda = 1$  and Figure 2.15 for  $\Lambda = 10$ . On increasing  $r_{ib}$  there is an initial drop in  $R_c$  followed by a sharp increase at higher  $r_{ib}$ . We also see a changeover between modes 2 and 3 in Figure 2.14, although the preferred mode remains so here. For  $\Lambda = 10$ , the initial decrease of  $R_c$  with  $r_{ib}$  is much more marked, the stronger field allowing  $r_{ib}$  to be increased to higher values before convection becomes inhibited. This also is what we found for the field (2.30). Eigenfunctions of the real part of  $b_r$  for both  $\Lambda = 1$  and  $\Lambda = 10$  are shown in Figure 2.16. These are similar to those with the original field, and indeed we see that for a higher magnetic field strength the eigenfunctions have moved away from the rotation axis  $\theta = 0$ . This further echos the results with the original field.

Since the results for fields (2.30) and (2.32) are qualitatively the same, it was decided to continue with the original field (2.30).

## 2.4 EFFECT OF DIFFERENTIAL ROTATION

We now consider the effect of differential rotation on the problem by increasing the magnetic Reynolds number,  $R_m$ , from zero. We choose as our basic flow

$$U_0 = 64r^3(1 - r^2)^2 \cos^2 \theta \sin \theta \mathbf{1}_\phi \quad (2.34)$$

This choice of  $U_0$  is such that  $U_0/s = (B_0/s)^2$ , and this flow was also considered in Fearn and Proctor (1983a). It provides a fairly typical differential rotation, with both  $r$  and  $\theta$  dependence, in addition to being a check for our results. We look at the case  $\Lambda = 1$ ,  $m = 2$ , and choose  $r_{ib} = 0.35$ , which is

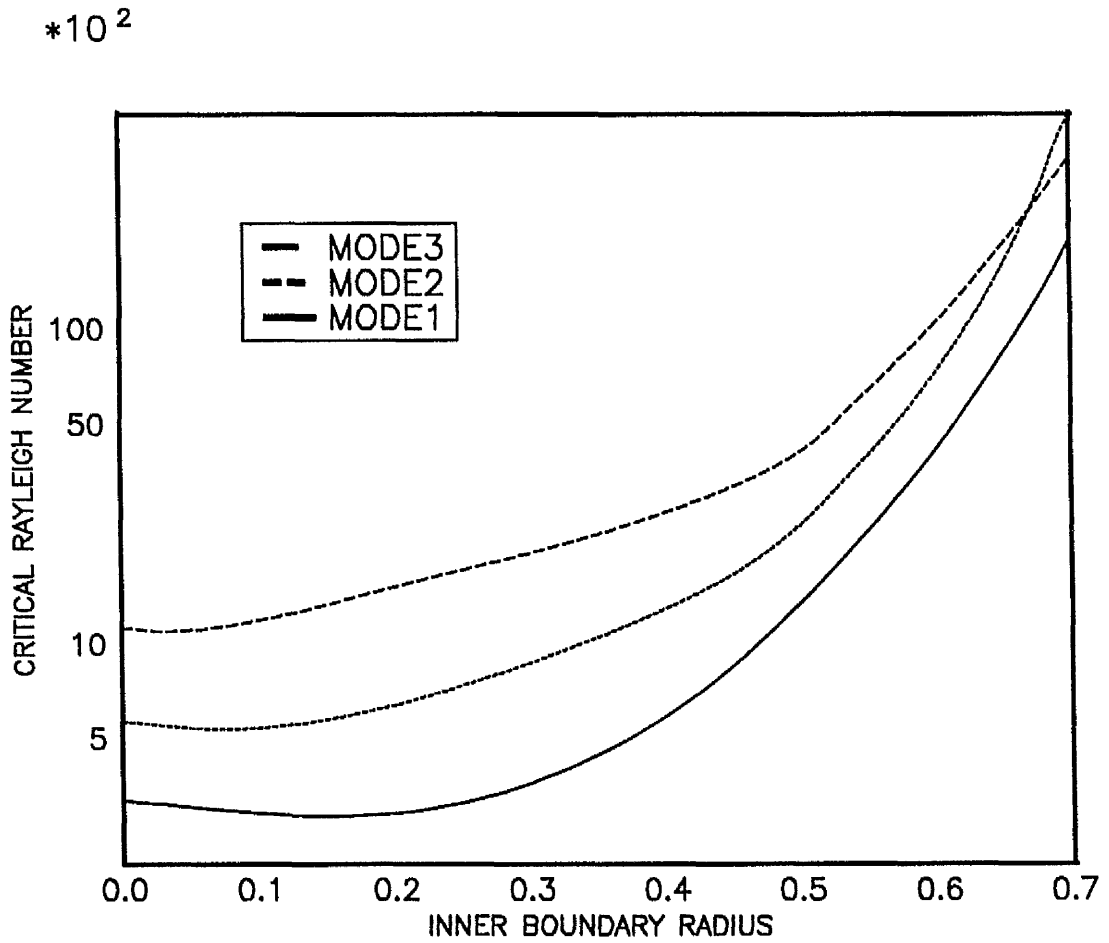


Figure 2.14: Graph of  $R_c$  against  $r_{ib}$  for the three most unstable modes with basic field (2.32),  $\Lambda = 1, m = 2, q = 10^{-6}$  and quadrupole parity.

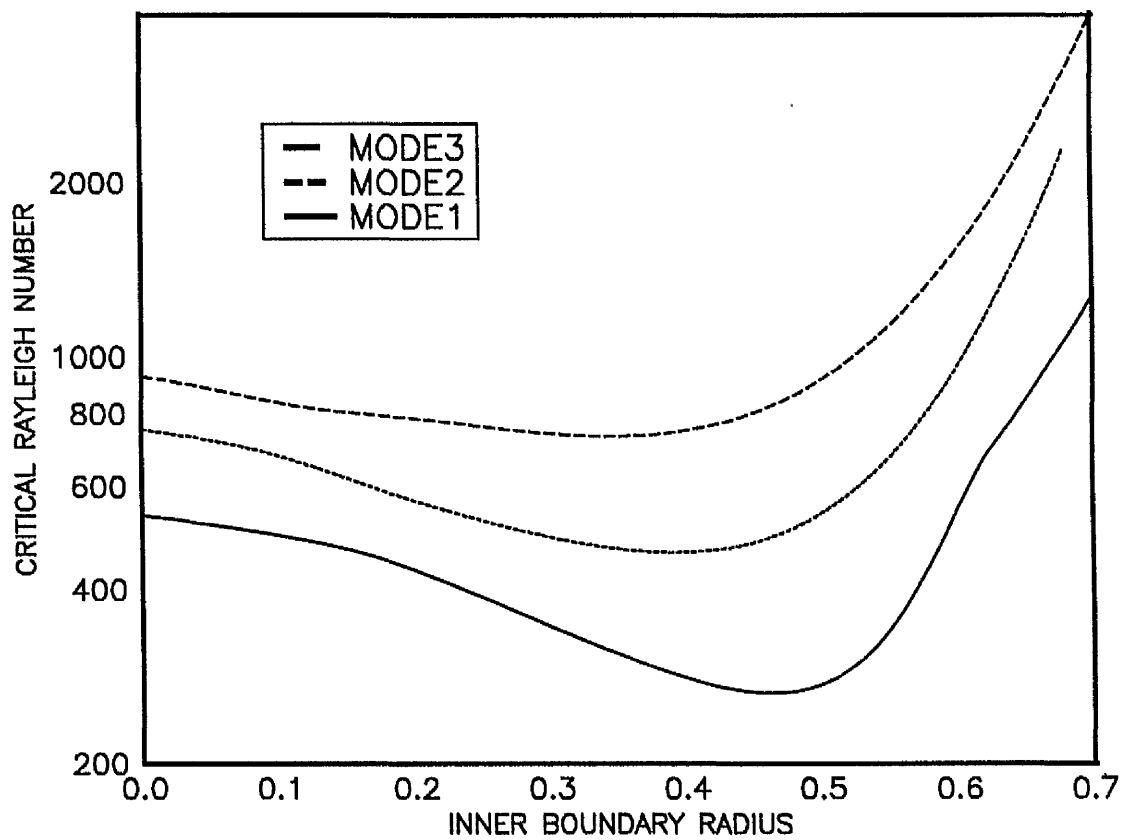


Figure 2.15: As Figure 2.14, but with  $\Lambda = 10$ .

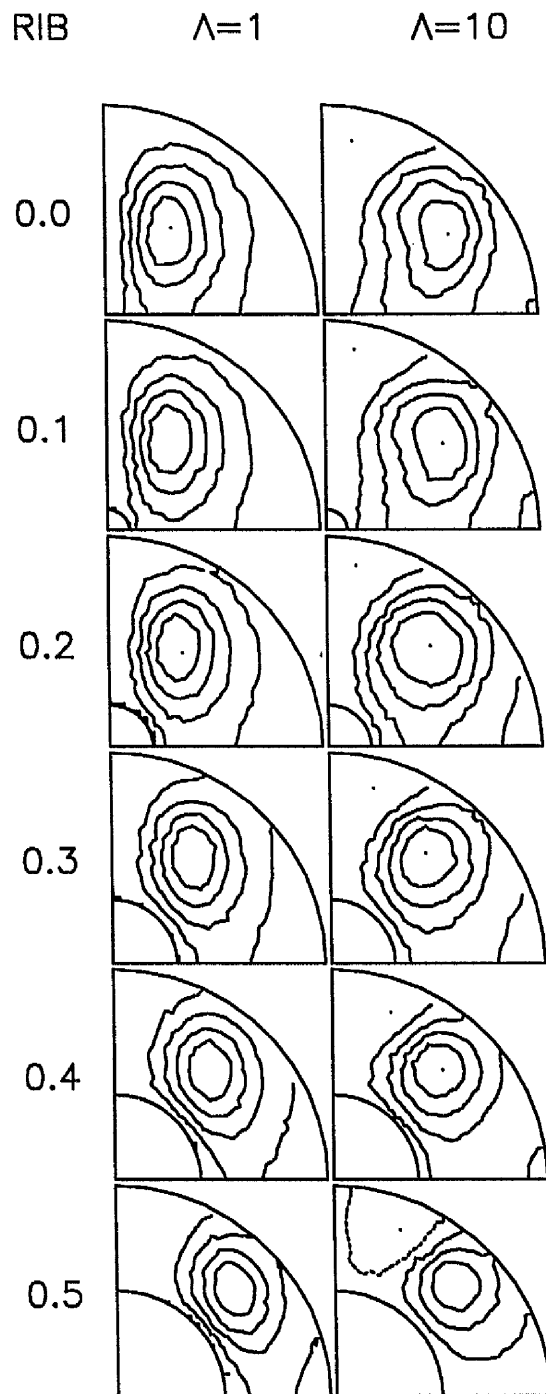


Figure 2.16: Eigenfunctions of the real part of  $b_r$ , for the most unstable modes from Figures 2.14 and 2.15.

close to the ratio of the radii of the Earth's inner and outer cores. We consider  $q = 10^{-6}$  as before and also look at the case  $q = 1$  where the effects of thermal and magnetic diffusion are comparable.

#### 2.4.1 $q = 10^{-6}$

Using the three modes found in Section 2.2.5 for  $\Lambda = 1, r_{ib} = 0.35$  and quadrupole parity we gradually increase  $R_m$ . Figure 2.17 shows the effect on  $R_c$  of this increase. At first there is a very small decrease in  $R_c$ , but when  $R_m$  becomes  $O(q)$  there is a sharp rise. This is in accordance with Fearn and Proctor (1983a) and with work done in plane layer and cylindrical geometries (Fearn and Proctor 1983b, Fearn 1989a).

As the effect of the differential rotation becomes stronger, we see that convection becomes increasingly localised. The temperature perturbation in particular becomes very concentrated at the place where the shear is minimum for  $R_m \gg O(q)$ . For our choice of flow (2.34), the minimum for  $r$  is at  $r \sim 0.58$  and we see concentration at about this radius, but the  $\theta$ -minimum is at the edges  $\theta = 0, \frac{\pi}{2}$  so the concentration can take place at any latitude  $\theta$ , as we see later with other parameter choices. This behaviour is also in agreement with Fearn and Proctor (1983a). This concentration of convection occurs because the instability tends to be carried along with the flow. The competing effects of shear and diffusion determine the width of the region of concentration. For the case studied here of  $q = 10^{-6}$ , the thermal diffusion timescale is much longer than the magnetic diffusion timescale. The magnetic field is thus more able to diffuse, and so there is no concentration of the perturbed magnetic field. Because thermal diffusion is much weaker, the temperature perturbation is localised in the region where it can match the effects of the shear. Eigenfunctions of  $\vartheta$  and  $b_r$  are shown in Figure 2.18. The concentration of the perturbations suggest that in such a case the presence of an inner boundary would have little effect. This is seen to be true if we hold  $R_m$  fixed at  $10^{-3}$ , and iterate  $r_{ib}$  back to 0. The eigenfunctions are found to be very similar, and the critical Rayleigh numbers are quite close

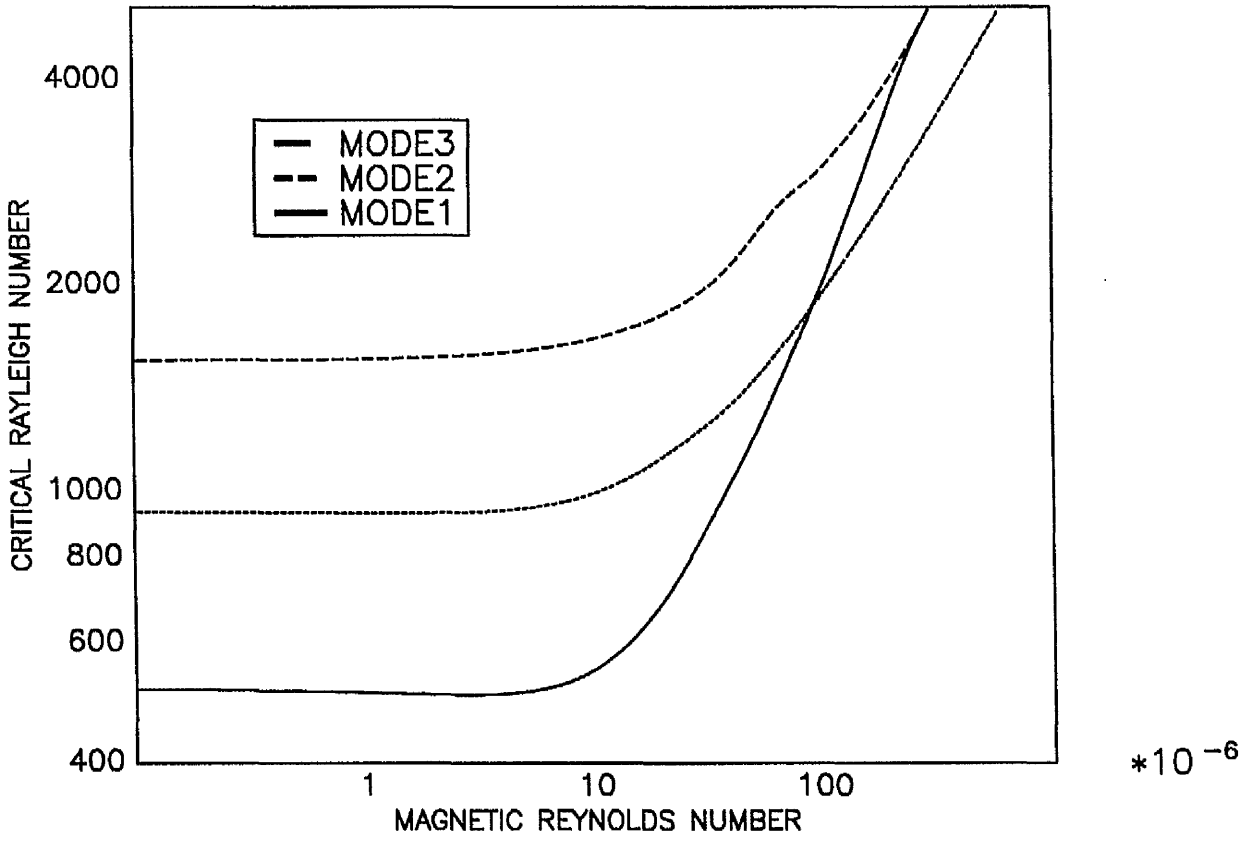


Figure 2.17: Graph of  $R_c$  against  $R_m$  of the three most unstable modes for basic field (2.30),  $r_{ib} = 0.35$ ,  $\Lambda = 1$ ,  $m = 2$ ,  $q = 10^{-6}$  and quadrupole parity.

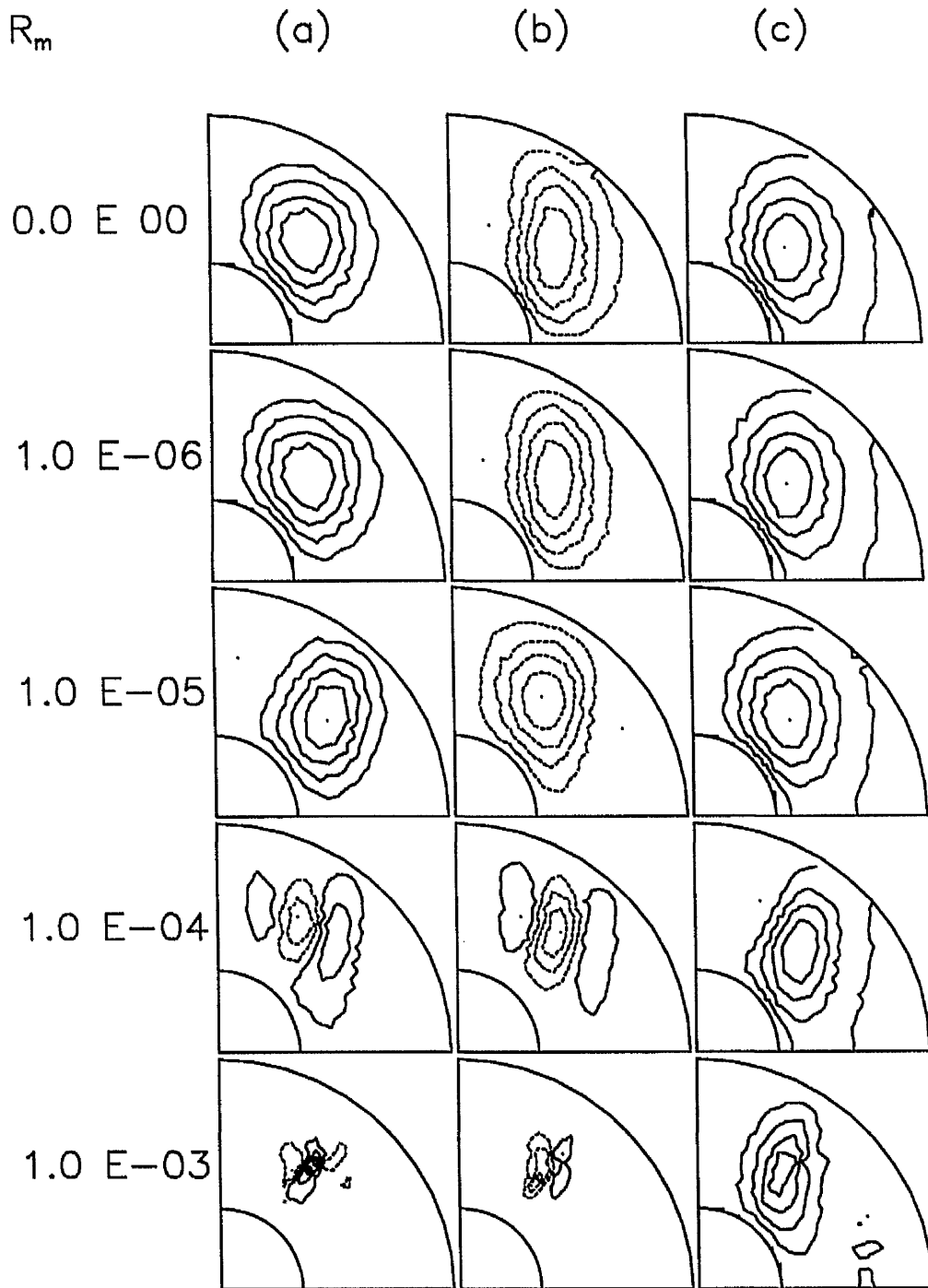


Figure 2.18: Eigenfunctions of (a) real part of  $\vartheta$ , (b) imaginary part of  $\vartheta$  and (c) real part of  $b_r$  for the most unstable mode of Figure 2.17.

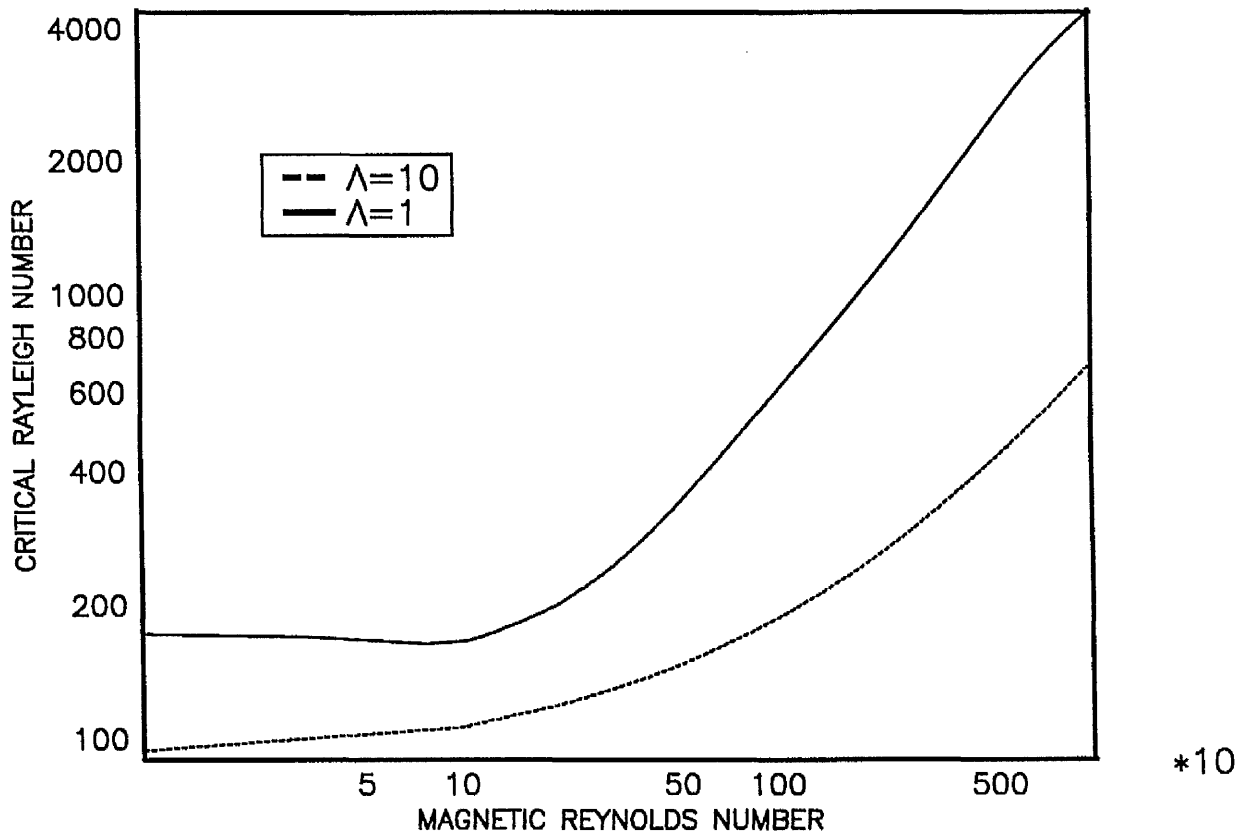


Figure 2.19: Graph of  $R_c$  against  $R_m$  for the most unstable modes with  $r_{ib} = 0.35$ ,  $m = 2$ ,  $q = 10^{-6}$  and dipole parity for both  $\Lambda = 1$  and  $\Lambda = 10$ .

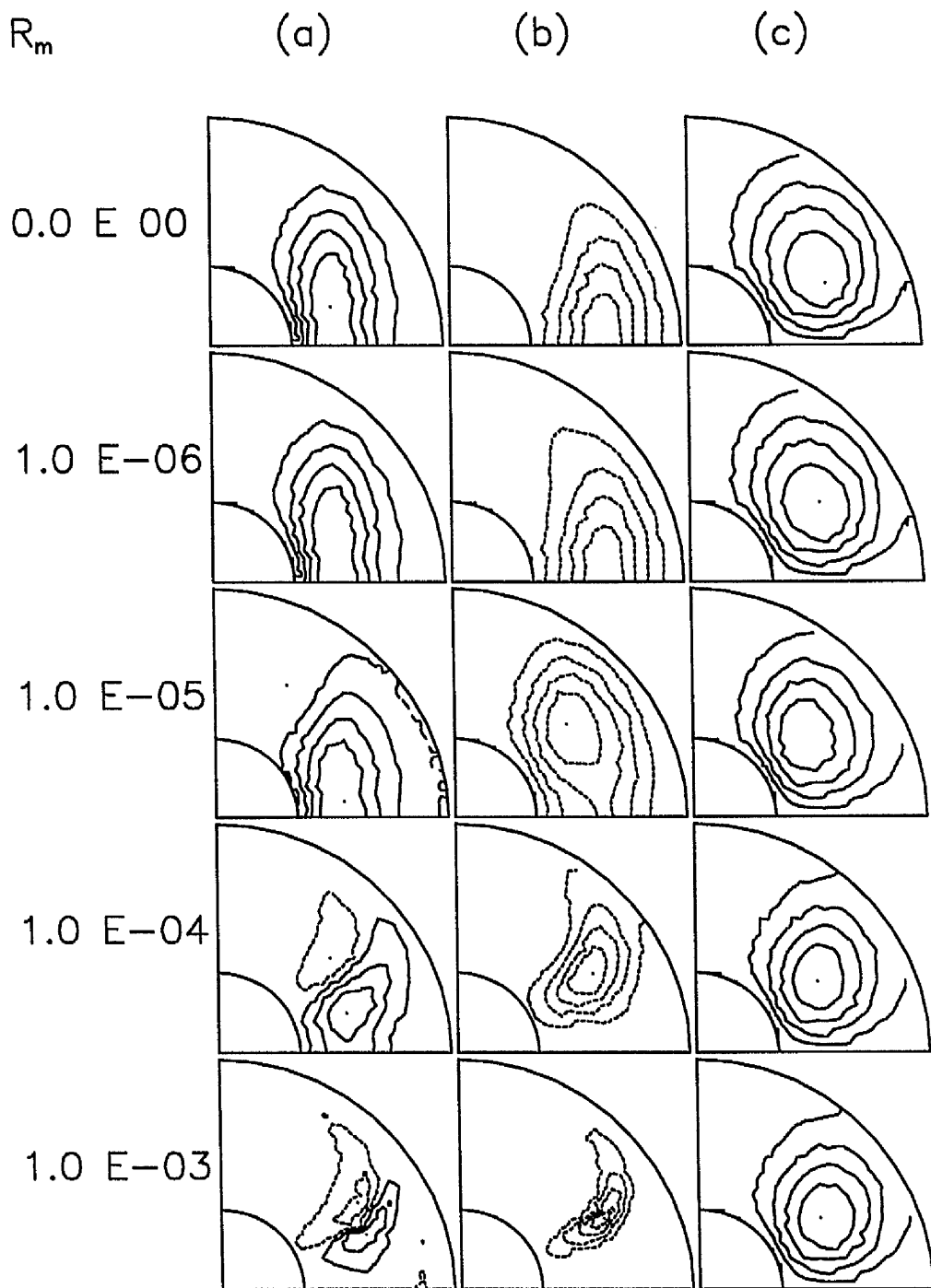


Figure 2.20: As Figure 2.18 but for the most unstable mode with  $\Lambda = 1$  of Figure 2.19.

( $R_c = 8892.07$  for  $r_{ib} = 0$  and  $R_c = 8709.29$  for  $r_{ib} = 0.35$ ).

If we repeat these calculations with dipole parity of solution we find similar behaviour. Figure 2.19 shows the relationship between  $R_c$  and  $R_m$  for the most unstable mode with both  $\Lambda = 1$  and  $\Lambda = 10$ , and eigenfunctions of  $\vartheta$  and  $b_r$  are shown in Figure 2.20. Again we see that the  $\vartheta$  perturbations become concentrated for  $R_m \gg O(q)$ , while the other perturbations do not. This is the same behaviour as was noted with quadrupole parity.

#### 2.4.2 $q = 1$

We considered in Section 2.4.1 the diffusivity ratio  $q = 10^{-6}$  which is a relevant value for the Earth if we take molecular values for the diffusivities. If, however, thermal and magnetic diffusivity are of the same order, i.e. if  $q = 1$ , then we find slightly different behaviour. The graph of  $R_c$  against  $R_m$  is shown in Figure 2.21 for the most unstable mode with  $m = 2$ ,  $r_{ib} = 0.35$  and quadrupole parity for  $\Lambda = 1$  and  $\Lambda = 10$ . For the case when  $\Lambda = 1$ , the most unstable mode at first shows familiar behaviour. After an initial decrease in  $R_c$ , convection becomes inhibited when  $R_m = O(1)$ . This decrease is more evident for  $\Lambda = 10$ . If we continue to increase  $R_m$ , we find the picture complicated by instabilities due to the shear itself (see e.g., Fearn 1989; Fearn and Weiglhofer 1992b), but we do not concern ourselves with these in this study.

The eigenfunctions for the  $\Lambda = 1$  case are shown in Figure 2.22. Here all the perturbation variables become concentrated for  $R_m \gg O(q)$ . This mirrors for a spherical shell what was found in other geometries (Fearn, Roberts and Soward 1988; Fearn 1989a). In this case of  $q = 1$ , thermal and magnetic diffusivity are comparable, and this is why all the perturbation variables become concentrated here.

Repeating the above but with dipole symmetry again results in similar findings. The graph of  $R_c$  against  $R_m$  for the most unstable modes with  $\Lambda = 1$  and  $\Lambda = 10$  is shown in Figure 2.23. Here we see that as  $R_m$  is increased there is a drop in  $R_c$  initially, although for  $\Lambda = 1$  there is a sharp dip when  $R_m = O(5)$ . After

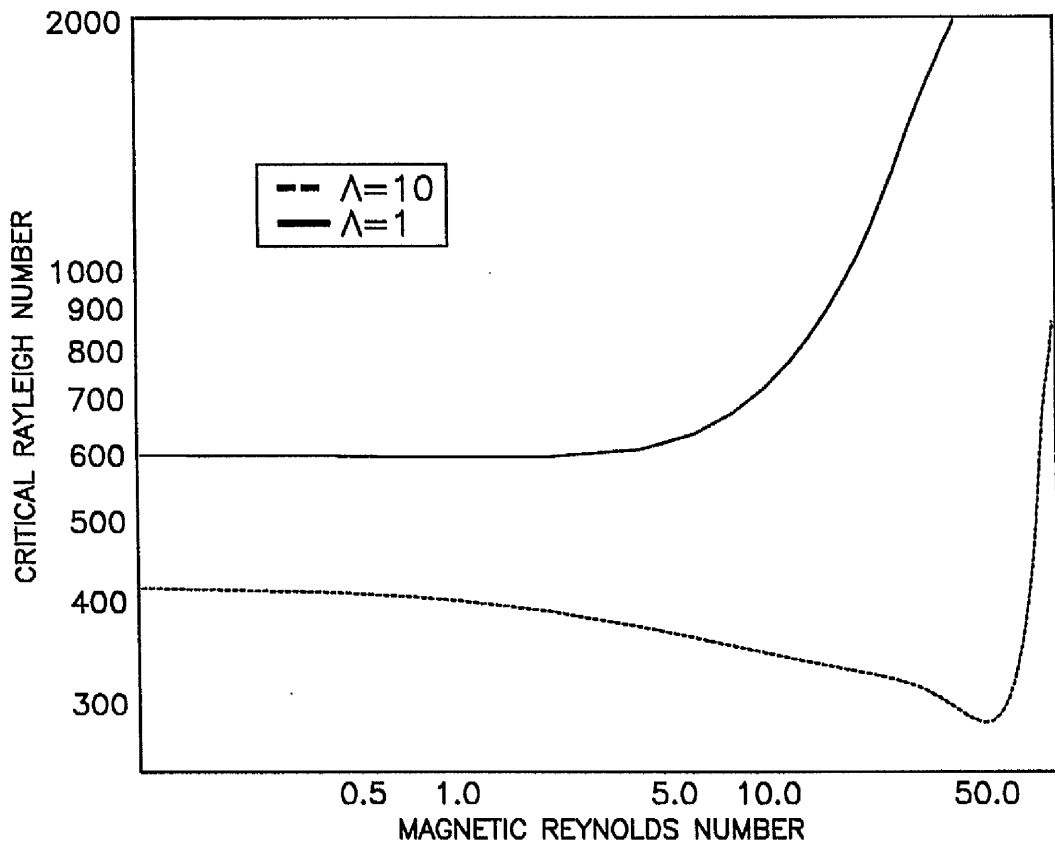


Figure 2.21: As Figure 2.19 but with  $q = 1$  and quadrupole parity.

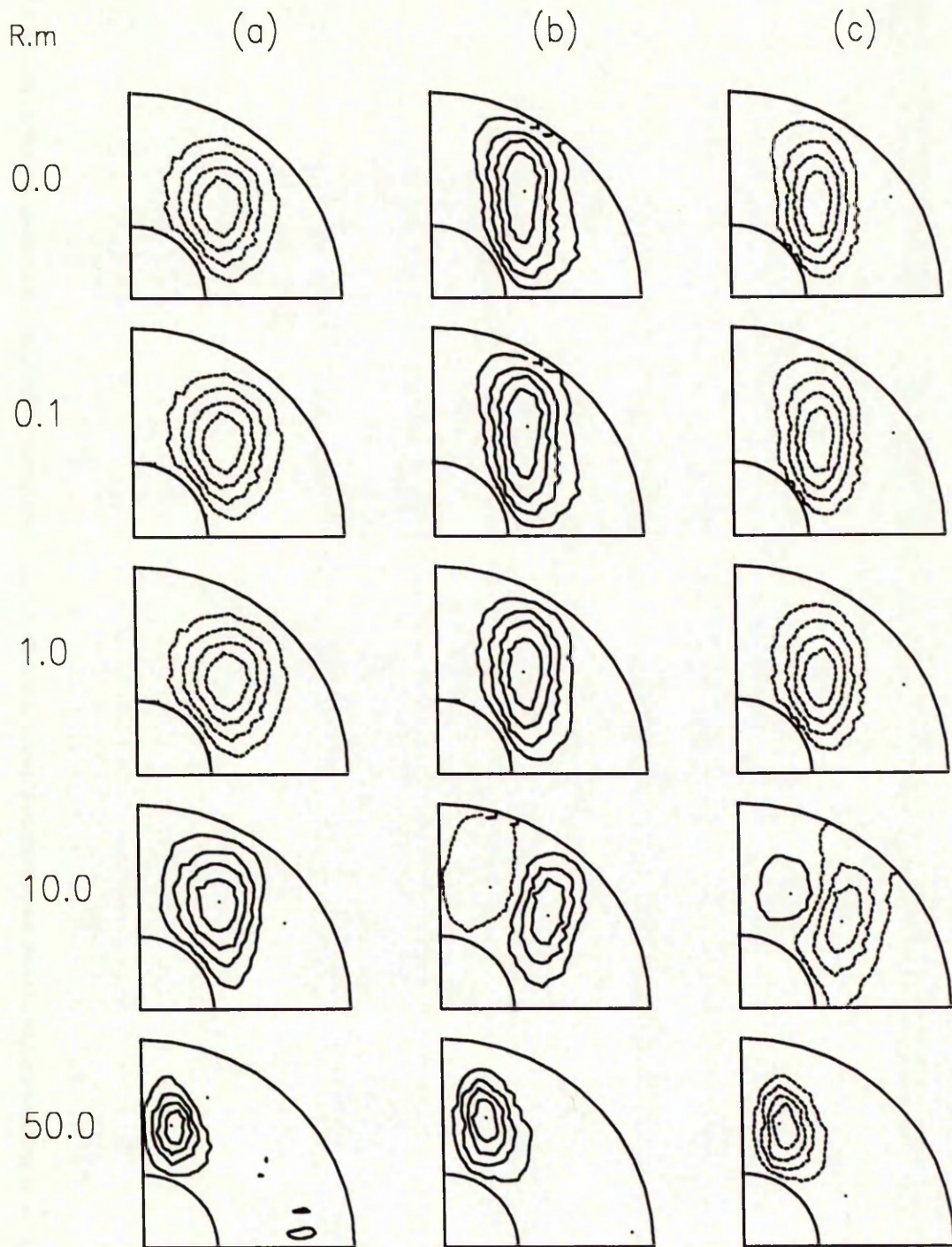


Figure 2.22: As Figure 2.18 but for the most unstable  $\Lambda = 1$  mode of Figure 2.21.

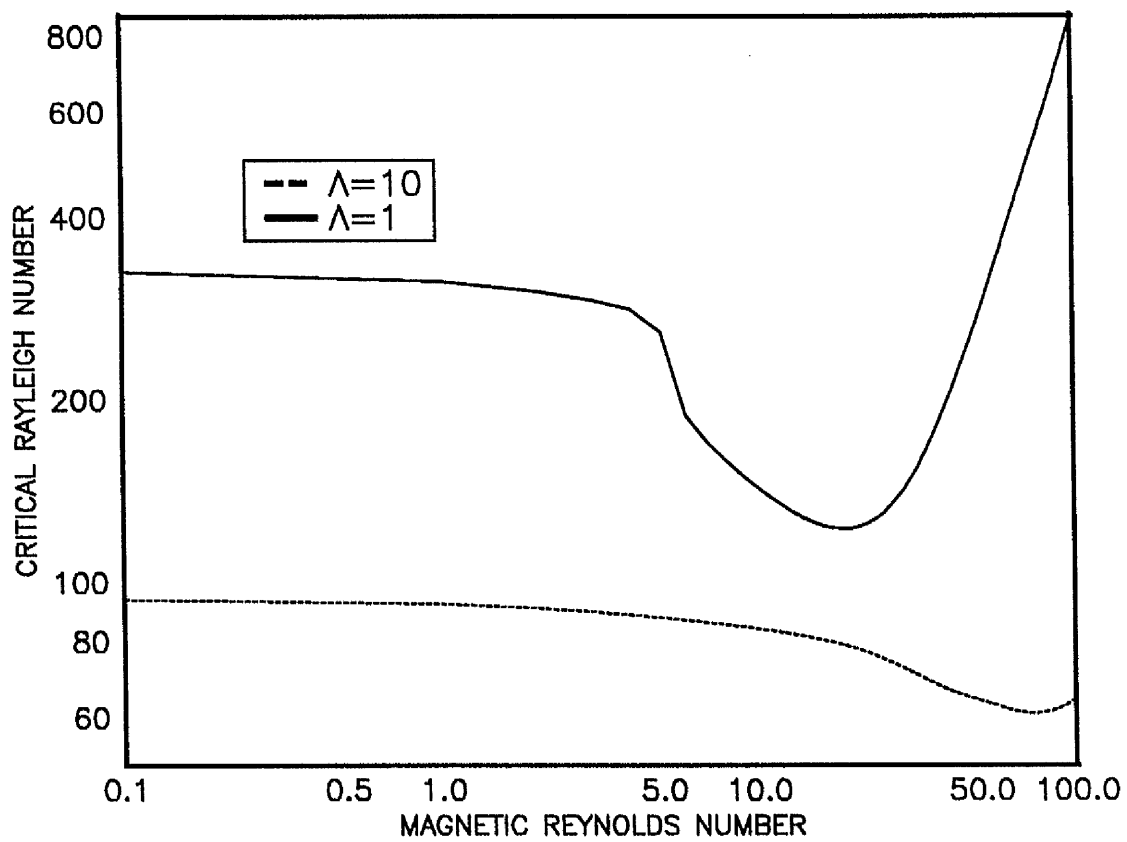


Figure 2.23: As Figure 2.19 but with  $q = 1$ .

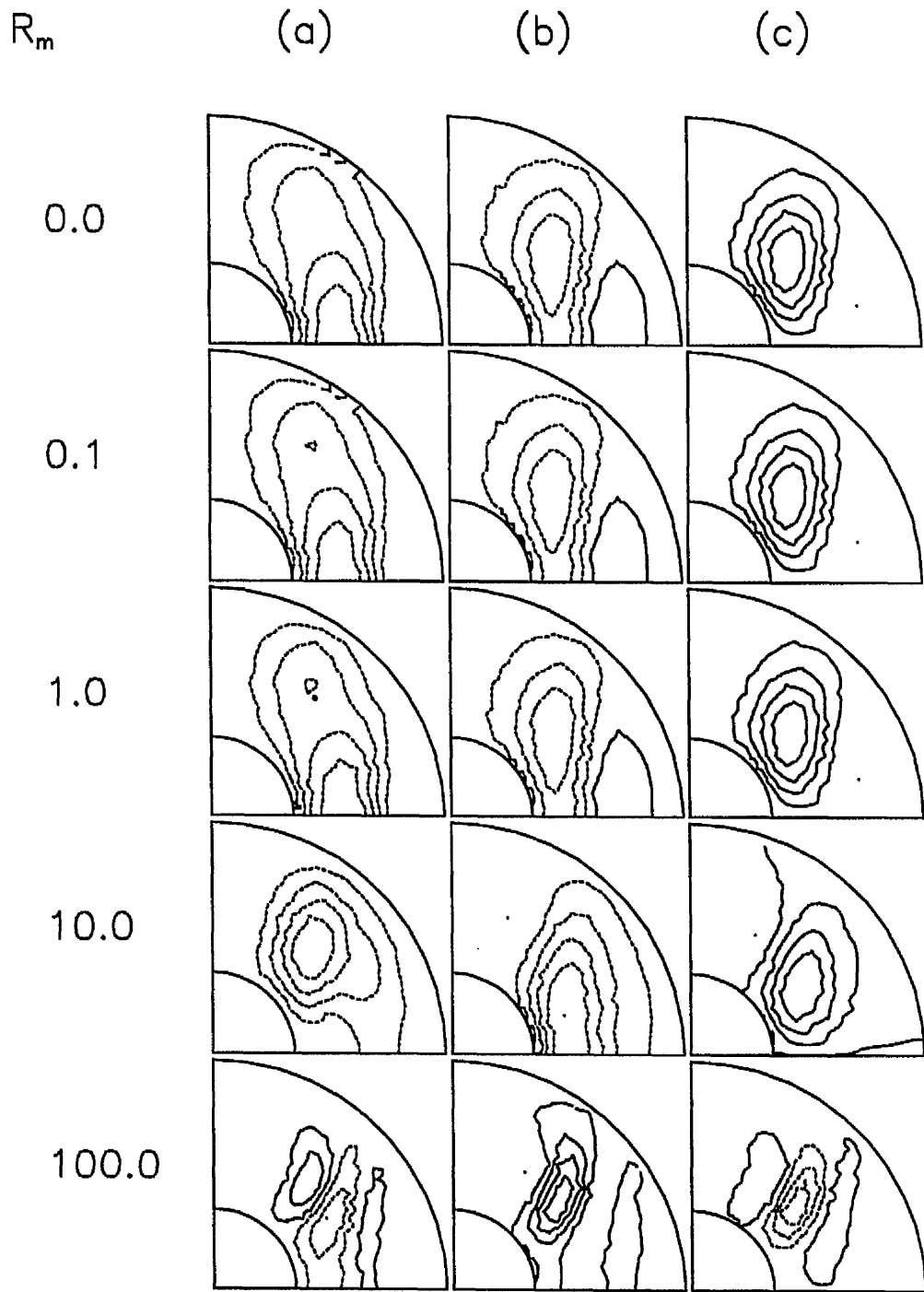


Figure 2.24: As Figure 2.18 but for the most unstable  $\Lambda = 1$  mode of Figure 2.23.

this though we find convection becoming strongly inhibited as before. Eigenfunctions of  $\vartheta$  and  $b_r$  for the  $\Lambda = 1$  case are shown in Figure 2.24. As for the quadrupole parity, we see that all the perturbation variables become concentrated for  $R_m \gg O(q)$ .

### 2.4.3 Initial decrease of $R_c$ with $R_m$

We have noted above that in many cases, increasing  $R_m$  initially results in a decrease in  $R_c$ . This behaviour was not seen by Fearn and Proctor (1983a) who studied the  $r_{ib} = 0$  case with the same flow and parameters. This was felt to be worthy of further investigation, so we considered three other flows, namely

$$\mathbf{U}_0 = -\frac{25}{16}\sqrt{5}r(1-r^2)^2 \sin\theta \mathbf{1}_\phi, \quad (2.35)$$

which was also studied in Fearn and Proctor (1983a),

$$\mathbf{U}_0 = \frac{4}{C^2 r}(r-r_{ib})^4(1-r^2)^2 \cos^2\theta \sin\theta \mathbf{1}_\phi, \quad (2.36)$$

and,

$$\mathbf{U}_0 = -\frac{25\sqrt{5}}{256C^2 r^3}(r-r_{ib})^4(1-r^2)^2 \sin\theta \mathbf{1}_\phi. \quad (2.37)$$

Flow (2.35) was used in conjunction with basic magnetic field (2.30), but the other two flows were used with the basic magnetic field (2.32) used in Section 2.3.9, which included the parameter  $C$  used above, defined by (2.33). The same parameters were used as with our first flow, i.e.,  $r_{ib} = 0.35$ ,  $m = 2$ ,  $q = 10^{-6}$  and  $\Lambda = 1$ , and we considered quadrupole parity. With each of the three flows (2.35)–(2.37) no decrease in  $R_c$  was seen on increasing  $R_m$ . Increasing the field strength to  $\Lambda = 10$  resulted in similar findings - a slight initial decrease in  $R_c$  with flow (2.34) but not with any of the other three flows (2.35)–(2.37). We then looked at a case where the initial decrease in  $R_c$  was more marked, namely

the  $r_{ib} = 0.35$ ,  $\Lambda = 10$ ,  $m = 2$ ,  $q = 1$  and quadrupole parity case which was graphed in Figure 2.21. Again, only flow (2.34) resulted in the initial decrease in  $R_c$ . Although we are unable to explain the decrease seen with this choice of flow (2.34), it does seem to be characteristic of that flow, and does not otherwise affect the behaviour seen due to the addition of differential rotation.

## 2.5 VARYING THE TEMPERATURE DISTRIBUTION

Up to now we have considered a temperature distribution appropriate to a uniform distribution of radioactive heat sources in the core. This enabled us to make comparison with other work, but this mechanism is no longer believed to be the primary energy source for the dynamo. Instead it is the latent heat and compositionally buoyant material released by the freezing process at the inner core boundary that is the primary source of outer core convection (Fearn 1989b). We now consider a temperature distribution appropriate to a source of buoyancy at the inner core boundary.

### 2.5.1 Compositional Convection type distribution

In order to simulate compositional convection, we require a source of buoyancy at the inner core boundary, and since no light material passes into the mantle there must be a sink throughout the core. We choose a uniform sink, and produce a temperature gradient

$$\frac{dT}{dr} = r - \frac{1}{r^2} \quad (2.38)$$

This gradient is an admissible solution of the heat conduction equation (see Section 2.2.4). Clearly this is only a reasonable choice if we have a non-zero inner boundary radius, and so we consider  $r_{ib} = 0.35$  as in Section 2.4. We further require the boundary condition

$$\frac{d\vartheta}{dr} = 0 \quad (r = 1) \quad (2.39)$$

since no light material flows out into the mantle. Thus thermally we can model this essentially compositionally driven process, albeit in a somewhat crude manner.

As before we look for the onset of convection. We choose as parameters  $m = 2$ ,  $r_{ib} = 0.35$ ,  $q = 10^{-6}$  and quadrupole parity. The three most unstable modes were found and followed as the magnetic field strength  $\Lambda$  was increased (Figure 2.25). The eigenfunctions found with our new distribution are very similar to those found for the heat source distribution (see Figure 2.26). Although the convection patterns may be similar, by averaging the temperature gradients over the region, taking

$$\int_{r_{ib}}^1 r^2 \frac{dT}{dr} dr \quad (2.40)$$

we find that, with the same mean amount of driving, the compositional type distribution is more efficient, with a much lower critical Rayleigh number than for a distribution of heat sources. This is not really surprising, for when we look at the eigenfunctions (Figure 2.26), we see that convection is located more towards  $r = r_{ib}$  where the driving is strongest for our compositional type distribution and weakest for heat sources, with less convective motion at  $r = 1$  where most of the driving for the distribution of heat sources is located.

If we replace the  $r = 1$  thermal boundary condition, (2.39) with that used earlier ( $\vartheta = 0$ ), as would be appropriate for convection driven thermally by the release of latent heat at the inner boundary, then there is very little change in the calculations. Figure 2.27 shows the relationship between  $R_c$  and  $\Lambda$  with this distribution. This is very similar to Figure 2.25, the main difference being that the  $R_c$  values are  $\sim 20$  higher in this case. The eigenfunctions are similar to those of both the heat sources, and compositional type temperature distributions, and are also shown in Figure 2.26.

If we consider the dipole parity of solution, then we find similar results. The graph of  $R_c$  against  $\Lambda$  for the three most unstable modes with the latent

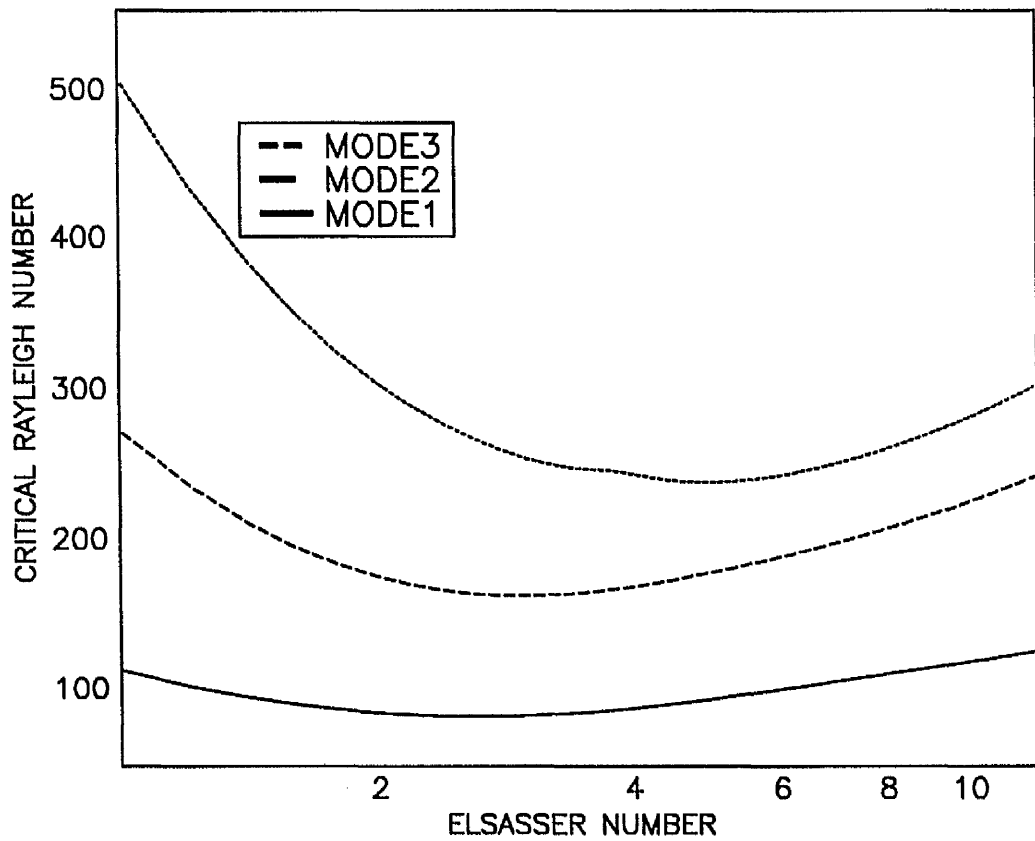


Figure 2.25: Variation of  $R_c$  with  $\Lambda$  for the three most unstable modes with compositional convection type heat distribution,  $r_{ib} = 0.35$ ,  $q = 10^{-6}$ ,  $m = 2$  and quadrupole parity.

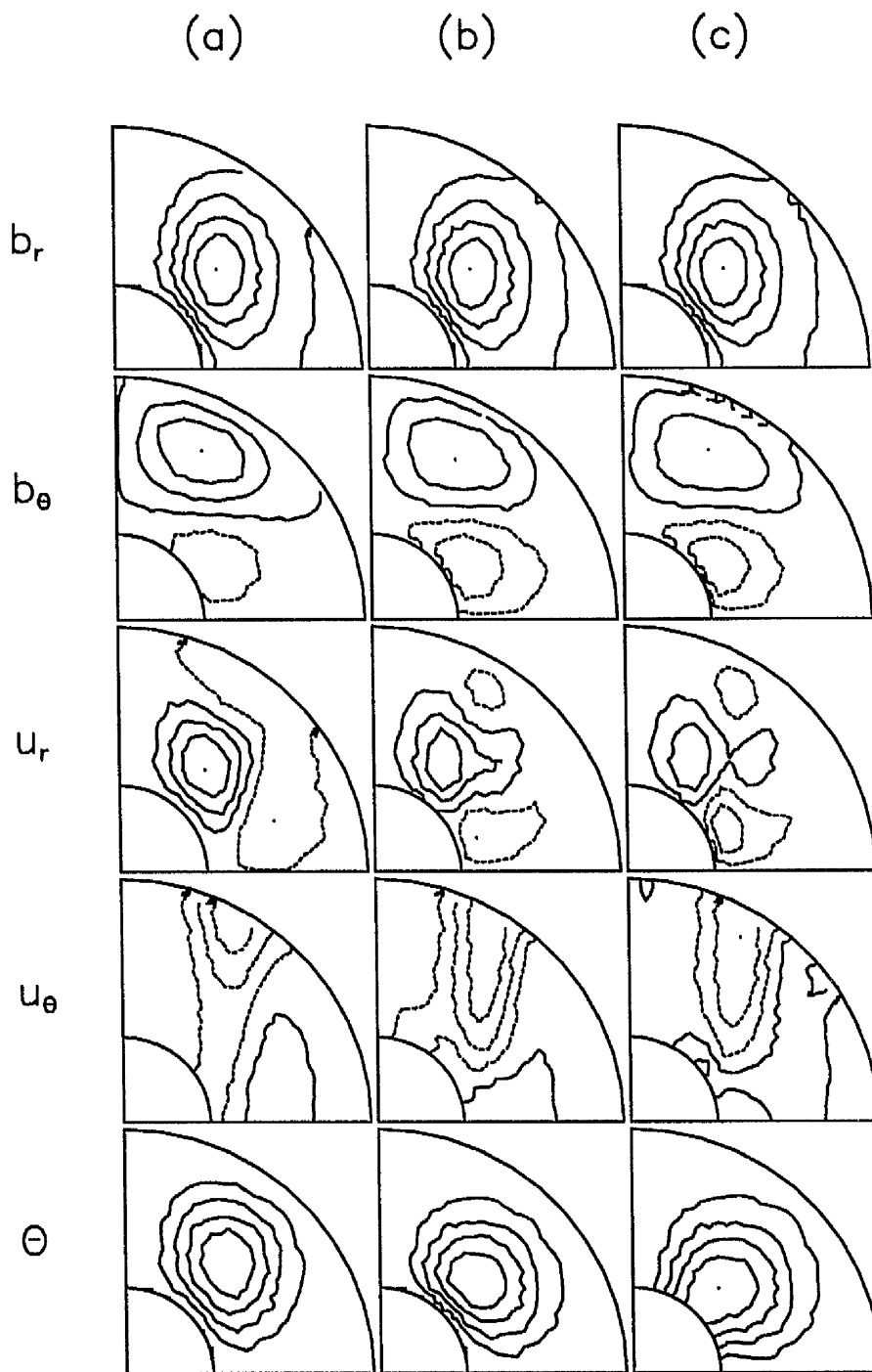


Figure 2.26: Eigenfunctions of the real parts of  $b_r$ ,  $b_\theta$ ,  $u_r$ ,  $u_\theta$  and  $\vartheta$  for (a) heat source, (b) latent heat, (c) compositional type distributions, for the most unstable modes with  $\Lambda = 1$ ,  $r_{ib} = 0.35$ ,  $m = 2$ ,  $q = 10^{-6}$  and quadrupole parity.  $R_c$  for these modes are (a) 508.450 (b) 141.365 (c) 111.905.

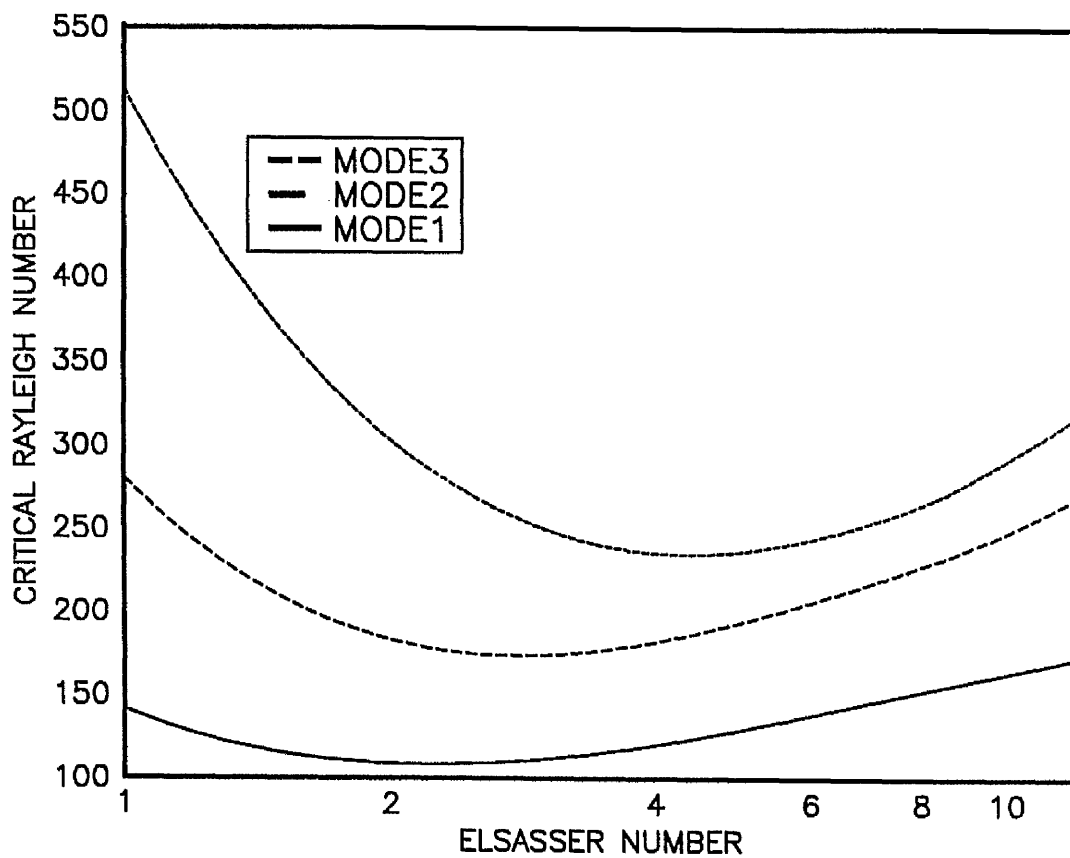


Figure 2.27: As Figure 2.25 but with latent heat distribution.

heat distribution is shown in Figure 2.28, and the eigenfunctions for all three distributions are shown in Figure 2.29. Again the eigenfunctions are very similar for all distributions, but the compositional type modes have much lower critical Rayleigh numbers than the heat sources distribution ones. This is what we found with the quadrupole parity results.

## 2.6 DISCUSSION AND CONCLUSIONS

We have seen that the growth of an inner core can have a marked effect on convection. One might expect that an increase in inner boundary radius would inhibit convection since the space available for convection is being reduced. This constriction clearly does have an important effect, particularly at higher  $r_{ib}$ . Initially, however, we see a slight decrease in  $R_c$  as  $r_{ib}$  increases from zero. As we so increase  $r_{ib}$ , though, we are introducing an inner core into a region where the temperature gradient is very small. In this region the main influence on the motion of the fluid here is the motion of the fluid at larger radius, which is driven by strong temperature gradient. By increasing  $r_{ib}$  here, we effectively remove this weakly driven fluid, and the available driving can concentrate solely on the remaining fluid, thus aiding convection. This process would explain the observed initial decrease in  $R_c$ . After this decrease, we do however see the expected increase in  $R_c$ , and, once  $r_{ib}$  reaches  $\sim 0.5$ , convection is strongly inhibited.

The above mechanism may also be behind the observed behaviour when  $\Lambda$  is increased. We have seen from Figures 2.5 and 2.7 for quadrupole symmetry of solution, and Figure 2.11 for dipole, that an increase in  $\Lambda$  moves convection away from the rotation axis. This allows  $r_{ib}$  to be increased to a greater extent before inhibiting convection, and this explains why the optimal  $r_{ib}$  value increases with  $\Lambda$ . Clearly there must be a limit to the maximum value of  $r_{ib}$  which can become optimal as eventually the constriction in space will become dominant. However, Figure 2.9 shows that this limit must be for  $r_{ib} > 0.35$ , which is about the present inner core radius. Thus, given a strong enough magnetic field, the growth of the inner core may not yet be seriously inhibiting convection.

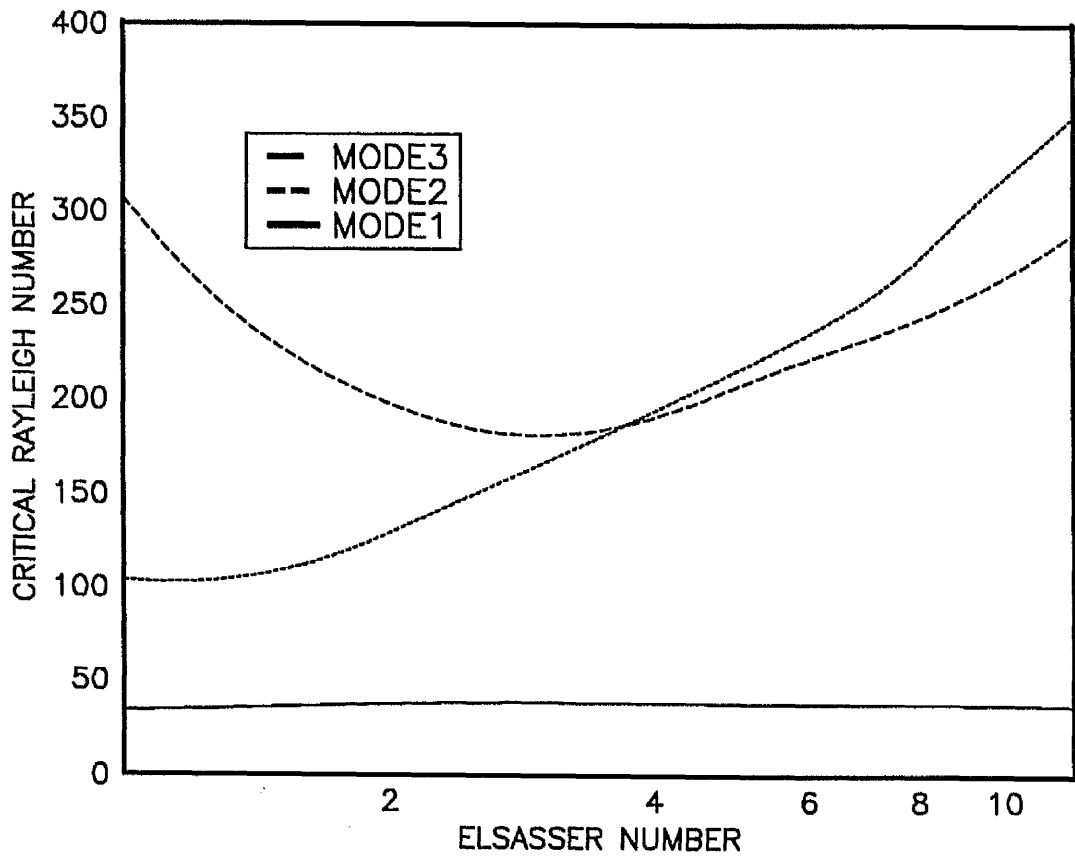


Figure 2.28: As Figure 2.25 but with latent heat distribution and dipole parity.

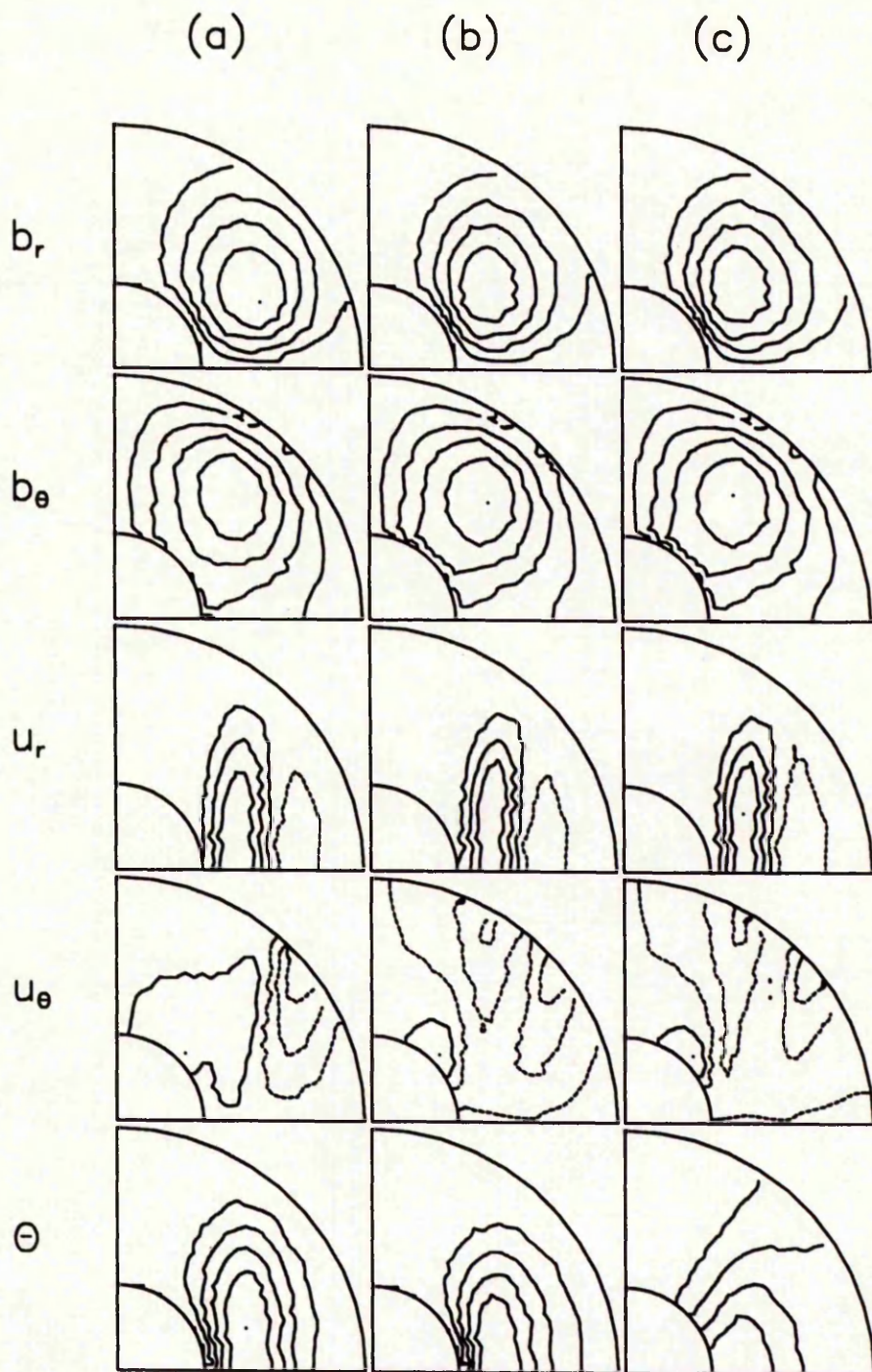


Figure 2.29: As Figure 2.26 but with dipole parity.  $R_c$  values are (a) 179.625 (b) 33.8148 (c) 18.3277

Overall we have seen that a growing inner core plays an important part in the development of convection in the outer core. Clearly, though, the extent to which it does affect the convective process is very much dependent on the strength of the toroidal magnetic field. Unfortunately this strength is not known with any great certainty for the Earth.

When we introduce differential rotation into the problem we see results for our spherical model which are qualitatively the same as in other geometries. We find that convection becomes increasingly localised as the strength of the shear is increased, this localisation occurring in the region of minimum shear. In this regime of concentrated convection it would certainly seem that convection is insensitive to inner core radius.

The results obtained here are strongly influenced by our choice of temperature distribution. The choice of that of a uniform distribution of heat sources allows us, as we said earlier, to make a comparison with other work, but is perhaps not an ideal choice. We have seen that a compositional type distribution is a more efficient driving agent for convection, although producing similar convection patterns. Apart from being a less energetic mechanism, there is no other obvious difference between the two.

## Chapter 3

# The effect of a stable layer at the core-mantle boundary on thermal convection

### 3.1 INTRODUCTION

As in Chapter 2, in this chapter we study, as a model for convection in the Earth's core, the linear stability of a rapidly rotating electrically conducting spherical fluid shell, permeated by a toroidal magnetic field  $\mathbf{B}$ . We now look at the effect of introducing a stably stratified layer into the fluid adjacent to the core-mantle boundary (CMB). We investigate three regimes of magnetic field strength. Firstly the weak field case  $\Lambda \ll O(1)$ , then the case  $\Lambda = O(1)$  and finally we consider the case of  $\Lambda \gg 1$ , comparing our work with that done previously in simpler geometries.

The question of whether or not some of the Earth's outer core is stably stratified has been studied in much detail. Evidence for the existence of a stably stratified layer adjacent to the core-mantle boundary (CMB), was found by Whaler (1980), and this was supported theoretically by the analyses of Fearn and Loper (1981) and Gubbins, Thomson, and Whaler (1982). This led to studies of convection in a rapidly rotating electrically conducting fluid with a stably stratified region. Boda (1988) and Ševčík (1989) studied convection in a horizontal fluid layer with the upper part stably stratified. Fearn and Richardson (1991) studied the problem using a cylindrical annulus model, with a stable region next to the outer boundary. We extend these results here to the more relevant geometry of a sphere.

The results found by these authors are dependent on the strength of the magnetic field, measured by the Elsasser number  $\Lambda$ . Boda studied the limit  $q \rightarrow 0$ . He found that for  $\Lambda \lesssim 1$  thermal instabilities could penetrate significantly into the stably stratified layer. As  $\Lambda$  is increased, however, convection becomes suppressed in the stable layer, and concentrates more in the unstably stratified region. Ševčík considered  $q \lesssim 1$  and found the same behaviour. Fearn and Richardson found that convection became concentrated in the unstable layer for both  $\Lambda < O(1)$  and  $\Lambda \gg 1$ , with a significant penetration into the stable region only for  $\Lambda = O(1)$ . This difference with Boda and Ševčík's results for  $\Lambda < O(1)$  was explained by the limitations on the azimuthal wave number values considered by Boda and Ševčík; they considered only  $m \leq 5$ . For  $\Lambda < O(1)$  the most unstable modes correspond to higher  $m$ . For example, Fearn and Richardson found  $m_c \sim 27$  for  $\Lambda = 0.1$ . They suggested that had Boda and Ševčík considered higher  $m$  then they too might have seen a suppression of convection in the stable layer. The results presented here, although finding the most unstable modes over all wavenumbers  $m$ , do not show this behaviour for  $\Lambda < O(1)$ . For  $\Lambda = 0.01, 0.1$  and  $1$ , there is significant penetration of convection into the stable layer. Only when  $\Lambda > O(1)$  do we find convection concentrating in the unstably stratified layer. We discuss this further in Section 3.4.

### 3.2 MODEL

The model considered here is that used in Chapter 2. We have an electrically conducting fluid outer sphere with a solid perfectly conducting inner core. The system is rapidly rotating with angular velocity  $\boldsymbol{\Omega}_0 = \Omega_0 \mathbf{1}_z$ , and the fluid is permeated by a toroidal magnetic field  $\mathbf{B} = B(r, \theta) \mathbf{1}_\phi$ . The outer boundary is taken to be electrically insulating. The linear stability analysis that we employ is identical to that of Section 2.2, and so we do not repeat the details here, but simply refer to equations in Chapter 2 when necessary.

The one change to the model of the previous chapter is to allow a stably stratified layer to exist adjacent to the CMB. We achieve this by modifying our

temperature gradient (2.38) to

$$\frac{dT}{dr} = \gamma r - \frac{1}{r^2} \quad (3.1)$$

where  $\gamma$  is an arbitrary constant. The choice of  $\gamma$  determines the size of the stable layer. Our default value  $\gamma = 1$  corresponds to no stable layer. Increasing  $\gamma$  from 1 introduces a stable layer increasing in size with  $\gamma$ . In this chapter we consider further values of  $\gamma$  of 2, 3 and 4 which correspond to stable layers from the core-mantle boundary down to  $r \sim 0.8, 0.7$  and  $0.63$  respectively. This choice of temperature gradient is an admissible solution of the heat conduction equation (see Section 2.2.4), and is produced by having an appropriate differential heating with a uniform heat sink throughout the fluid. We apply thermal boundary conditions appropriate to this type of heating, namely

$$\vartheta = 0, \quad (r = r_{ib}, 1) \quad (3.2)$$

### 3.3 RESULTS

In all our calculations we use an inner boundary radius,  $r_{ib} = 0.35$ , where we have non-dimensionalised the outer core radius to be 1. This is representative of the actual inner core radius. We choose  $q = 10^{-6}$ , which is representative of the diffusivity ratio of the Earth. We are always looking for the most unstable mode of solution for a particular field strength, i.e. the mode with the lowest critical Rayleigh number  $R_c$ . When this corresponds to an azimuthal wave number  $m = 1$ , there can be interference from magnetically driven instabilities (see Section 2.3.2). If we choose  $m \geq 2$  then for the values of  $\Lambda$  considered here, these magnetic instabilities are no longer present, and we observe only the thermal instabilities which are the subject of this study.

As our basic state we use that of (2.30), namely

$$\mathbf{B}_0 = 8r^2(1 - r^2) \sin \theta \cos \theta \mathbf{1}_\phi, \quad \mathbf{U}_0 = 0 \quad (3.3)$$

### 3.3.1 $\Lambda \ll 1$

We first consider the case of small magnetic field strength,  $\Lambda \ll 1$ . For our results in Chapter 2 we used a numerical resolution of  $20 \times 20$  grid points, and this gave us well resolved modes. In the low magnetic field strength regime, though, we expect to find a shortening in the lengthscales in both  $r$  and  $\phi$  directions (Fearn; 1979a). To ensure that we still have good resolution we increase truncation to  $32 \times 32$  grid points. Figure 3.1 shows the graph of the critical Rayleigh number and frequency as the number of grid points is increased for field strength  $\Lambda = 0.01$ . Comparison of the eigenfunctions for different truncations also shows that our solutions are reasonably well resolved.

We first consider the quadrupole parity of solution, and we consider here  $\Lambda = 0.1$  and  $\Lambda = 0.01$ , and note the effect on convection as a stable layer is introduced. As  $\Lambda$  is decreased, convection becomes increasingly columnar in structure. Also, the value of the azimuthal number,  $m$ , corresponding to the most unstable mode increases as  $\Lambda$  decreases. The value of  $m_c$  also depends on  $\gamma$ ; for  $\Lambda = 0.1$ ,  $m_c$  is 9 or 10, and for  $\Lambda = 0.01$ ,  $m_c$  is between 29 and 31. We introduce a stably stratified layer by increasing the parameter  $\gamma$  in (3.1) above 1. We choose values of  $\gamma$  of 1,2,3 and 4. We show contour plots of the eigenfunctions of some of the perturbation variables, and also graph the kinetic energy of radial flow,  $u_r^2$  as a function of radius. We obtain these graphs by first averaging  $u_r^2$  over  $\theta$  at different values of  $r$ , and then normalising this to have maximum value unity. In Figure 3.2 we illustrate for  $\Lambda = 0.1$  and increasing stable layer size, the radial component of the perturbation of magnetic field  $\mathbf{b}$ , the temperature perturbation  $\vartheta$  and the induced e.m.f.  $E_\phi$ , which is defined by

$$E_\phi = \langle \mathbf{u} \times \mathbf{b} \rangle \cdot \mathbf{1}_\phi, \quad (3.4)$$

where  $\langle .. \rangle$  denotes the azimuthal average, and in Figure 3.3 we graph the kinetic energy of radial flow. Similarly Figure 3.4 shows  $b_r$ ,  $u_r$  and  $\vartheta$  for  $\Lambda = 0.01$ , and Figure 3.5 graphs  $u_r^2$  against  $r$ . In each case the behaviour of the other

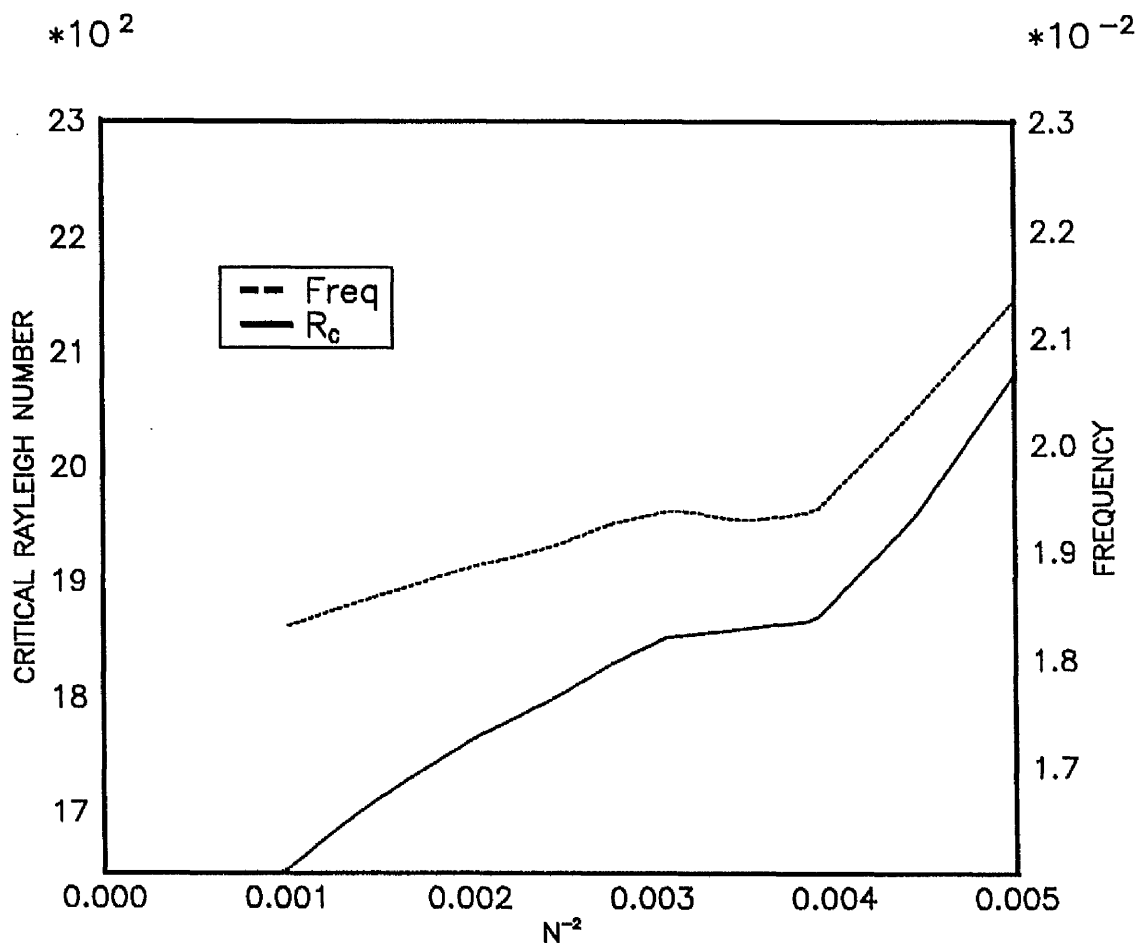


Figure 3.1: Graph of the convergence of  $R_c$  and critical frequency with the number of grid points for  $\Lambda = 0.01$ ,  $m_c = 29$ ,  $r_{ib} = 0.35$ ,  $q = 10^{-6}$  and quadrupole parity.

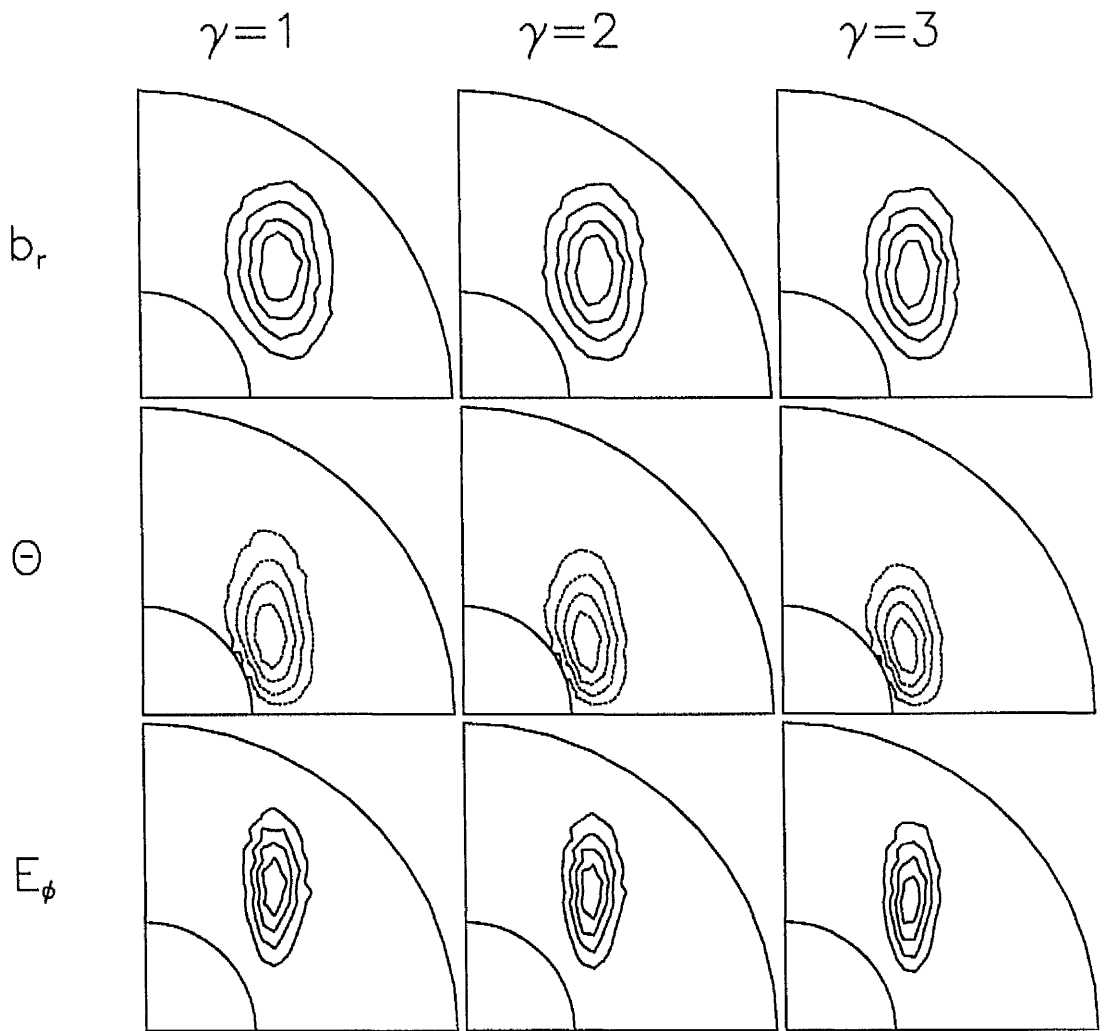


Figure 3.2: Eigenfunctions of the real part of  $b_r$ , the imaginary part of  $\vartheta$  and  $E_\phi$  for  $\Lambda = 0.1$ , quadrupole parity and for  $\gamma = 1, 2$  and  $3$ , corresponding to increasing stable layer size. The critical Rayleigh numbers for these modes are 260.261, 347.744 and 490.733 and the critical wave numbers are 9, 9 and 10 for  $\gamma = 1, 2$  and  $3$  respectively.

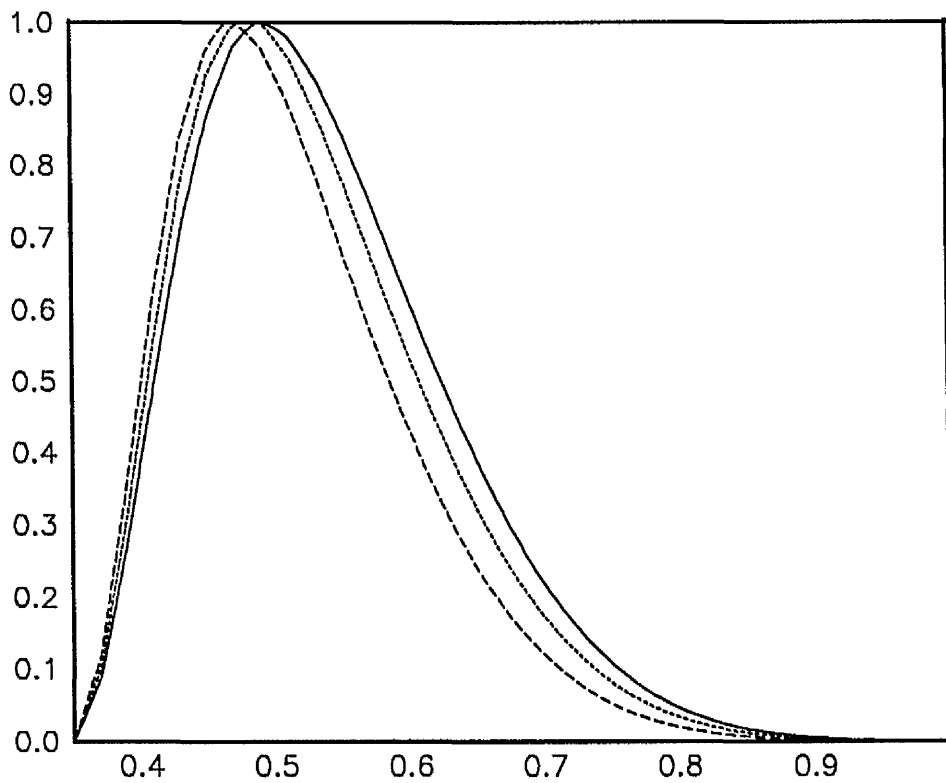


Figure 3.3: Graphs of the kinetic energy of radial flow,  $u_r^2$  as a function of radius for the cases  $\gamma = 1$  (full line), 2 (short dashed line) and 3 (long dashed line) of Figure 3.2.

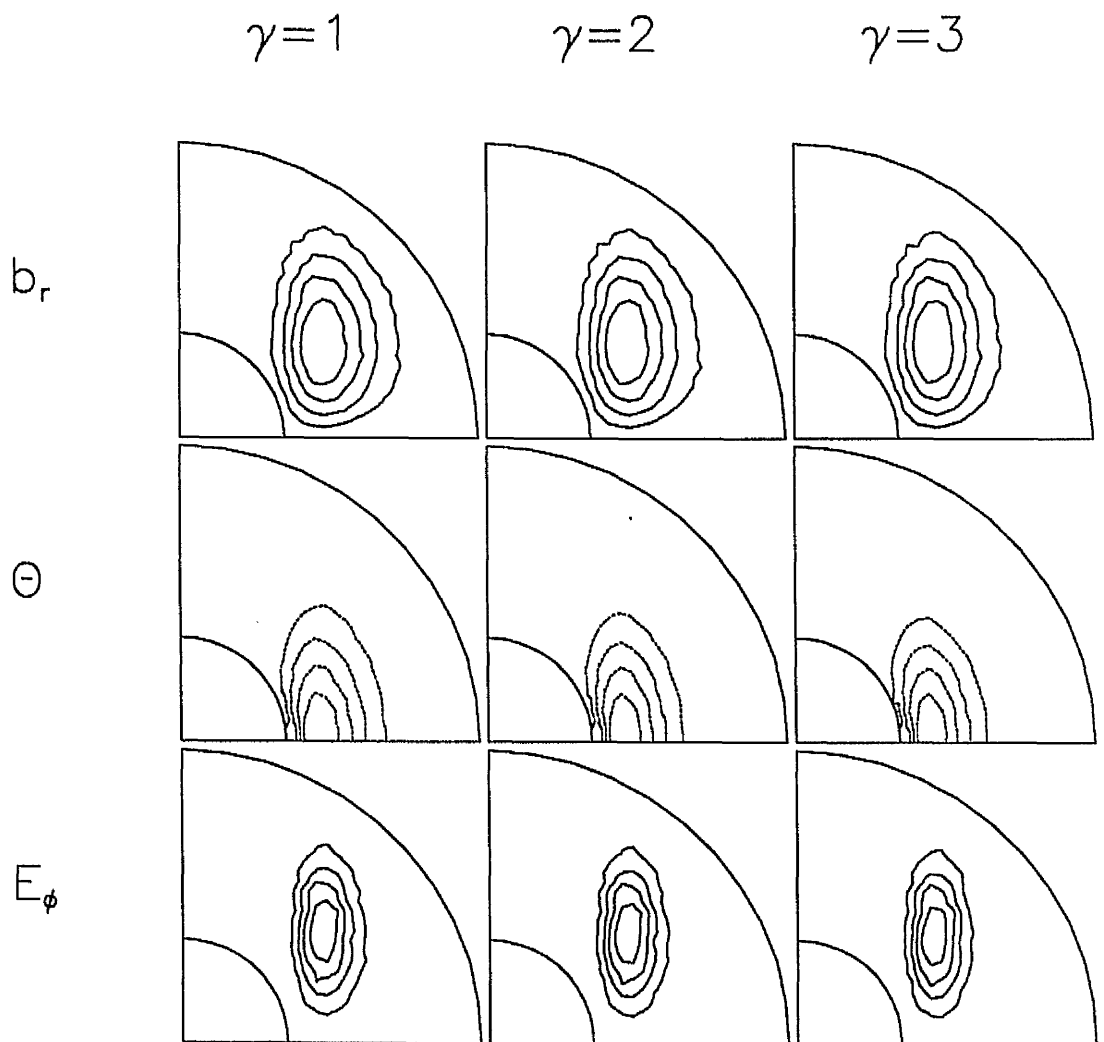


Figure 3.4: As Figure 3.2 but with dipole parity.  $R_c$  values here are 31.9196, 39.8086 and 52.0811 for  $\gamma = 1, 2$  and 3 respectively.  $m_c = 7$  in each case.

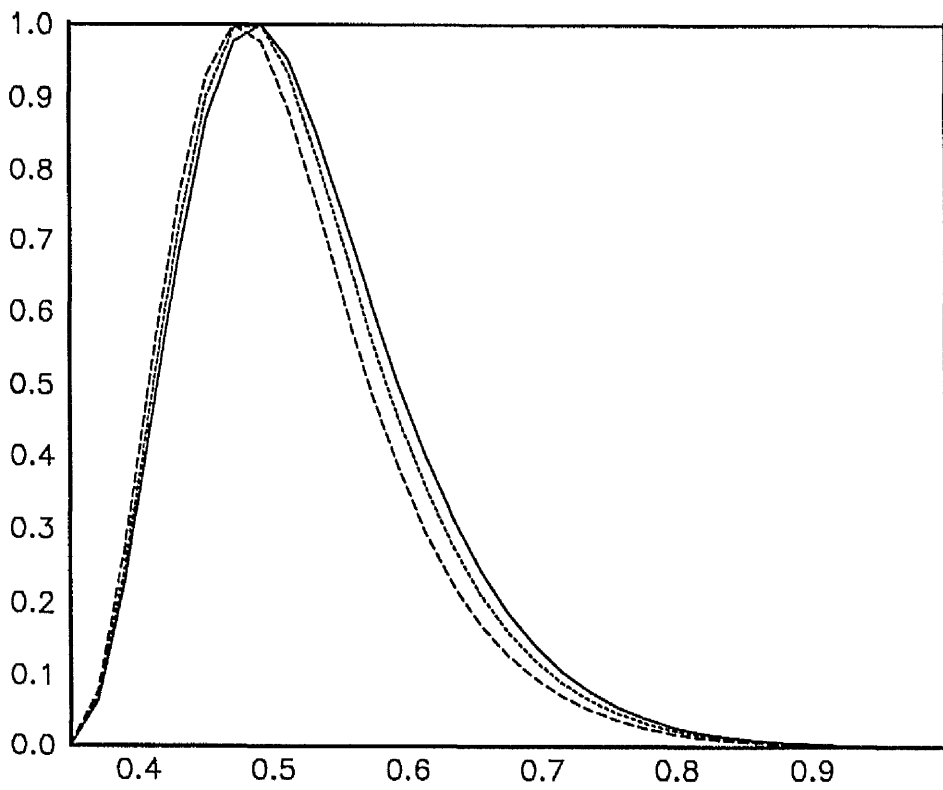


Figure 3.5: As Figure 3.3 but for the cases  $\gamma = 1, 2$  and  $3$  of Figure 3.4.

perturbation variables is the same as for  $b_r$ . We see that introducing a stable layer has very little effect on convection, except for the  $\vartheta$  perturbation which does concentrate in the unstable layer. This is not surprising as by introducing the stable layer we are removing the thermal driving from the upper part of the fluid, and increasing the heating in the stable layer. Looking at the other perturbations we find that as the size of the layer is increased there is only a very small movement towards the unstable layer, with a significant amount of the perturbations remaining in the stable part. This is not what was found in the cylindrical problem. In the cylindrical case, Fearn and Richardson investigated the competing roles of temperature gradient and magnetic field strength. For our choice of  $\mathbf{B}$ , not only is the fluid stable at the CMB, but  $\mathbf{B}$  is relatively weak. Both of these effects act to inhibit convection near the CMB in the cylinder, but for the sphere, the effect of the Taylor-Proudman theorem overcomes both (see discussion in Section 3.4).

If we repeat the above but with dipole symmetry, we find similar results. We show eigenfunctions and graphs of  $u_r^2$  against  $r$  for  $\Lambda = 0.1$  in Figures 3.6 and 3.7, and for  $\Lambda = 0.01$  in Figures 3.8 and 3.9. Again we see that as  $\Lambda$  becomes small, convection becomes columnar in structure, and that the addition of a stable layer has little effect on the perturbation variables. It is difficult to see any difference in the  $\vartheta$  perturbation in this case, but this is due to it being concentrated well away from the core-mantle boundary and hence also from any stable layer. The most unstable modes were found for azimuthal wave numbers  $m_c = 7$  for  $\Lambda = 0.1$  and  $m_c = 23$  or  $24$  for  $\Lambda = 0.01$ , which is also consistent with the quadrupole parity results.

### 3.3.2 $\Lambda = O(1)$

We now consider a field strength  $\Lambda = 1$ , and find the most unstable mode as before. This mode occurs for  $m = 1$ , but to avoid magnetic instabilities we consider the case  $m = 2$ . Eigenfunctions of  $b_r$  and the temperature perturbation  $\vartheta$  together with graphs of the kinetic energy of radial flow are shown in Figures

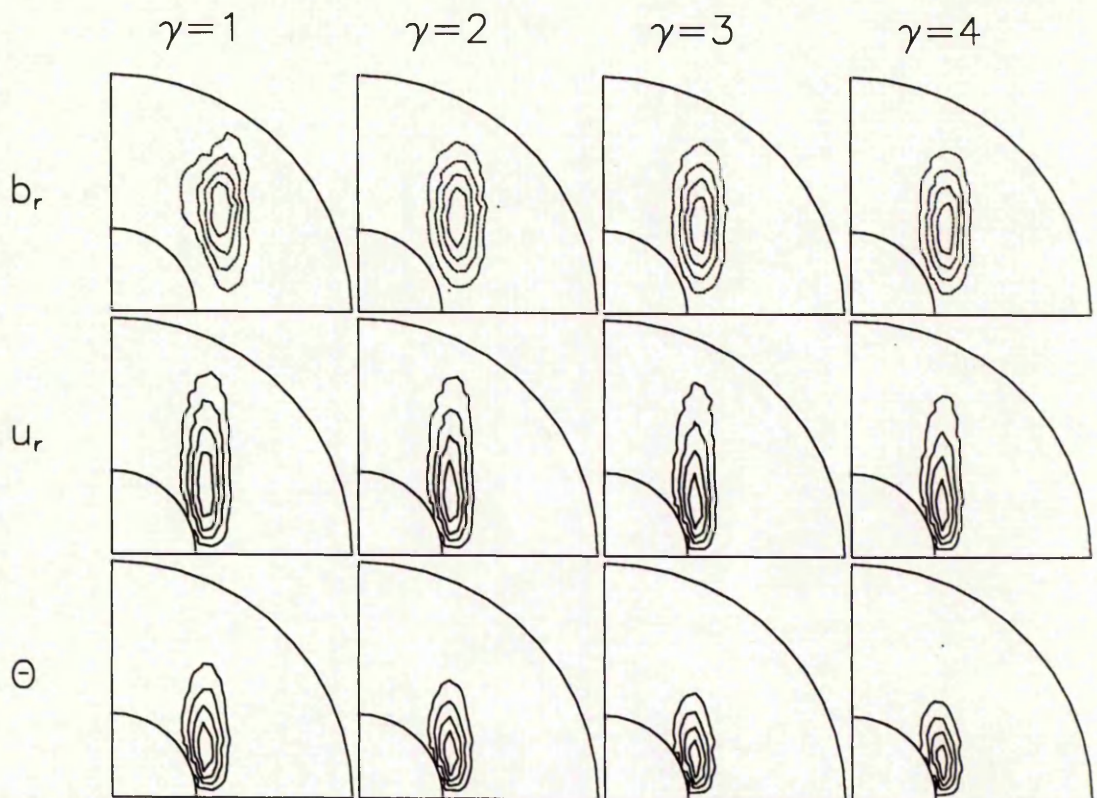


Figure 3.6: Eigenfunctions of  $b_r$ ,  $u_r$  and  $\vartheta$  for  $\Lambda = 0.01$  and quadrupole parity, as in Figure 3.2 but including a yet larger stable layer,  $\gamma = 4$  (dot-dashed line).  $R_c$  values in this case are 1646.22, 2133.26, 2900.76 and 4157.01, corresponding to  $\gamma = 1, 2, 3$  and 4. The critical wave numbers here are 29, 29, 30 and 31.

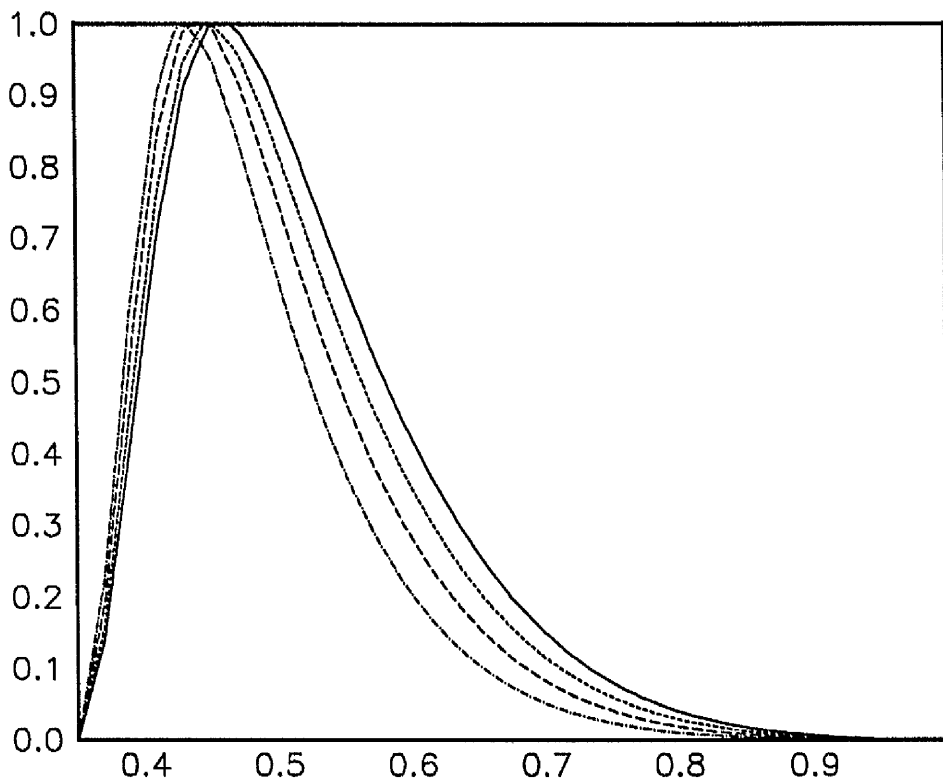


Figure 3.7: As Figure 3.3 but for the cases  $\gamma = 1, 2, 3$  and 4 of Figure 3.6.

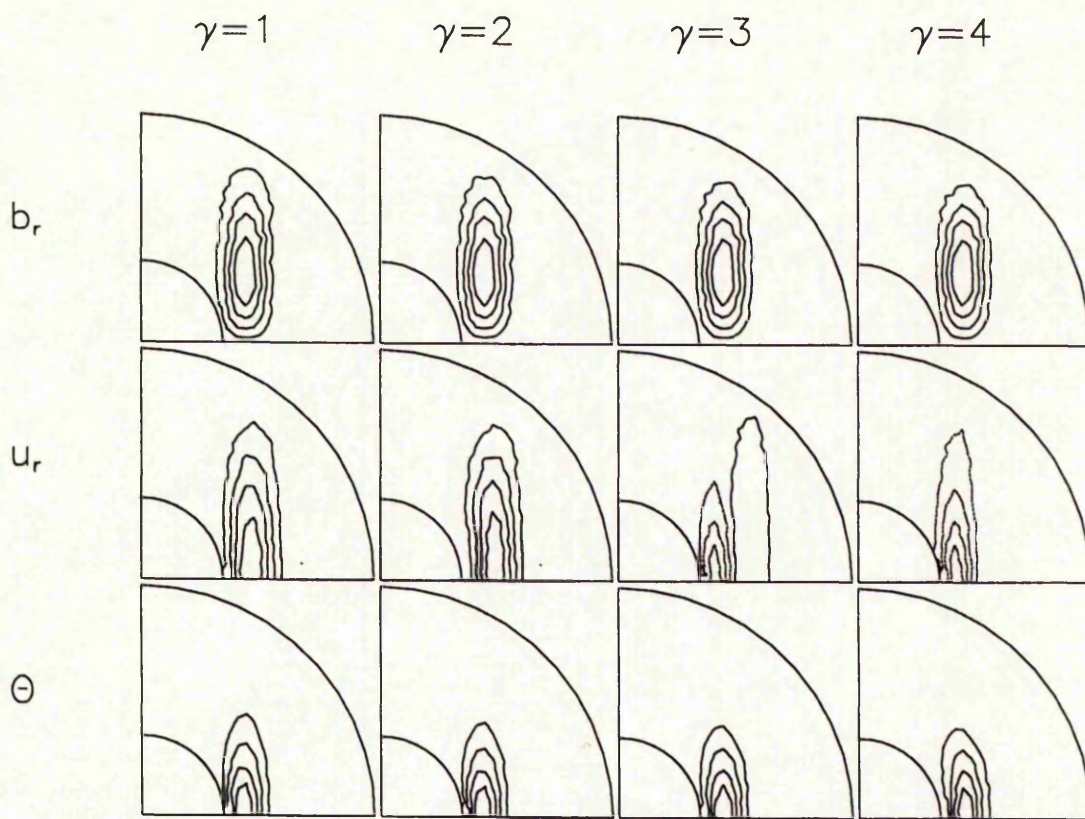


Figure 3.8: As Figure 3.6 but with dipole parity.  $R_c$  values here are 139.955, 171.848, 218.587 and 289.564, with  $m_c = 23, 23, 24$  and  $24$  for  $\gamma = 1, 2, 3$  and  $4$  respectively.

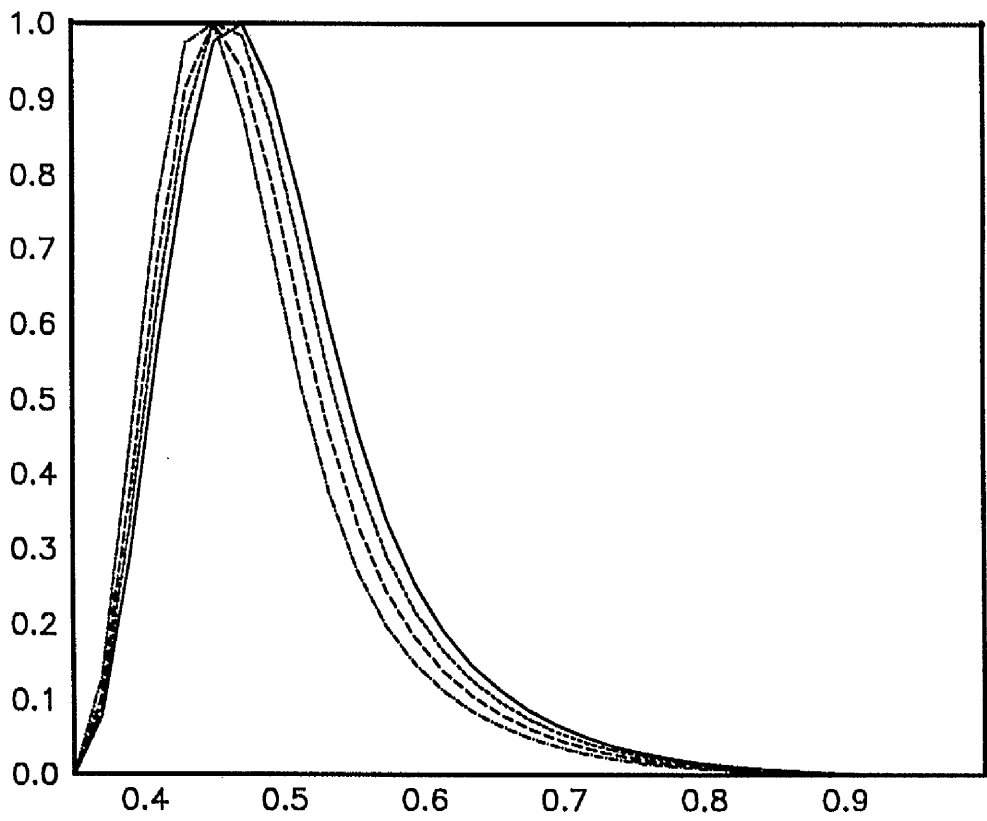


Figure 3.9: As Figure 3.3 but for the cases  $\gamma = 1, 2, 3$  and 4 of Figure 3.8.

3.10 and 3.11 (quadrupole parity), and Figures 3.12 and 3.13 (dipole). As in Section 3.3.1 the perturbation variables are not affected by the introduction of a stable layer, except for the  $\vartheta$  perturbation, which does concentrate in the unstable region for the same reasons as in Section 3.3.1.

### 3.3.3 $\Lambda \gg 1$

We now consider the large magnetic field case, taking values of  $\Lambda$  of 10, 20 and 50. In this regime we find that magnetic instabilities become more dominant, and indeed it was not possible to consider field strengths higher than  $\Lambda = 50$  because of this. The most unstable modes occur for  $m = 1$ , but with a strong magnetic field we found  $m = 1$  and  $m = 2$  instabilities to be magnetic in origin. We wish to study only thermal instabilities here, and we were able to do this by choosing  $m = 3$ . We show in Figures 3.14 and 3.15 (quadrupole) and Figures 3.16 and 3.17 (dipole), eigenfunctions of  $b_r$  and  $\vartheta$ , for  $\gamma = 1$  and  $\gamma = 3$  corresponding to the model without and with a stable layer, and graphs of  $u_r^2$  against  $r$ . For all values of  $\Lambda$  the addition of a stable layer causes convection to concentrate in the unstably stratified part as we expected. As  $\Lambda$  is increased, we find that this localisation of convection in the unstable layer becomes increasingly associated with a compression in the  $\theta$  direction. We comment further on this in Section 3.4.

## 3.4 DISCUSSION

We have studied the effect on thermal convection of adding a stably stratified layer adjacent to the core-mantle boundary. On the whole our results agree with the work of previous authors. Where using a spherical geometry has produced different results, though, is in the case of a small magnetic field strength. For  $\Lambda \ll 1$ , the primary force balance is between the Coriolis force and the pressure gradient. By the Taylor-Proudman theorem, convective motions will try to be independent of the  $z$ -direction, where the  $z$ -axis is the axis of rotation. This results in a tendency for convection to become elongated in  $z$ , leading towards a Taylor column structure (Busse 1978), as can be seen in Figures 3.6 and 3.8. Introduc-

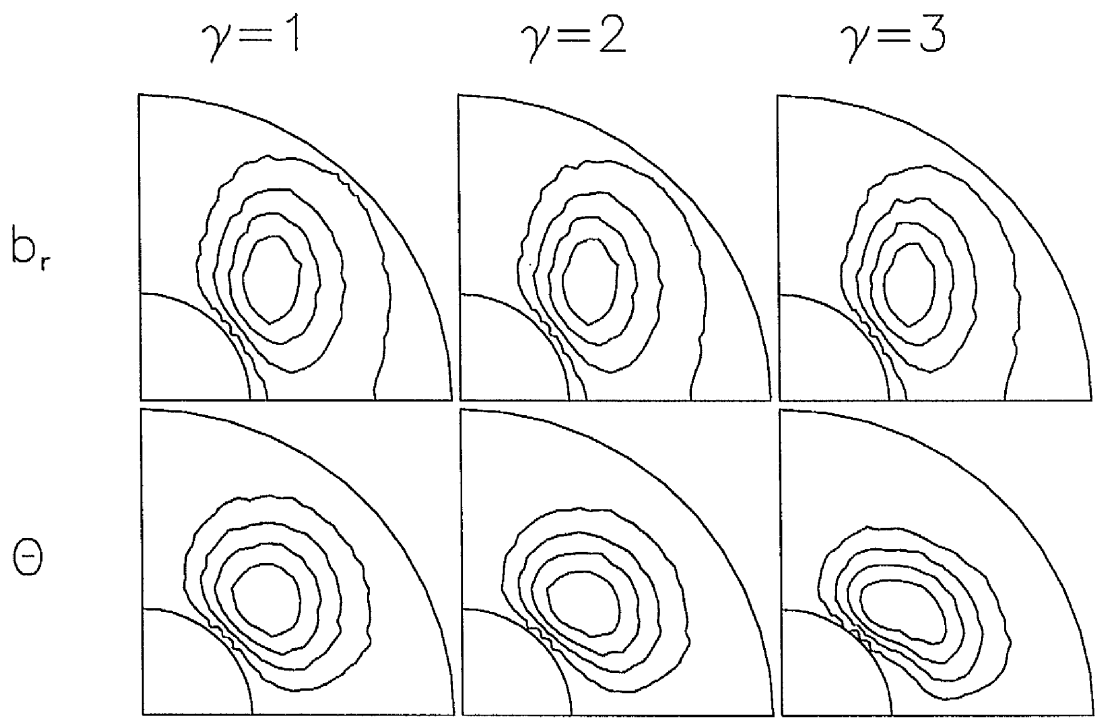


Figure 3.10: Eigenfunctions of  $b_r$  and  $\vartheta$  for  $\Lambda = 1, m = 2$  and quadrupole parity, and with  $\gamma = 1, 2$  and  $3$  for which  $R_c = 131.506, 183.720$  and  $297.551$  respectively.

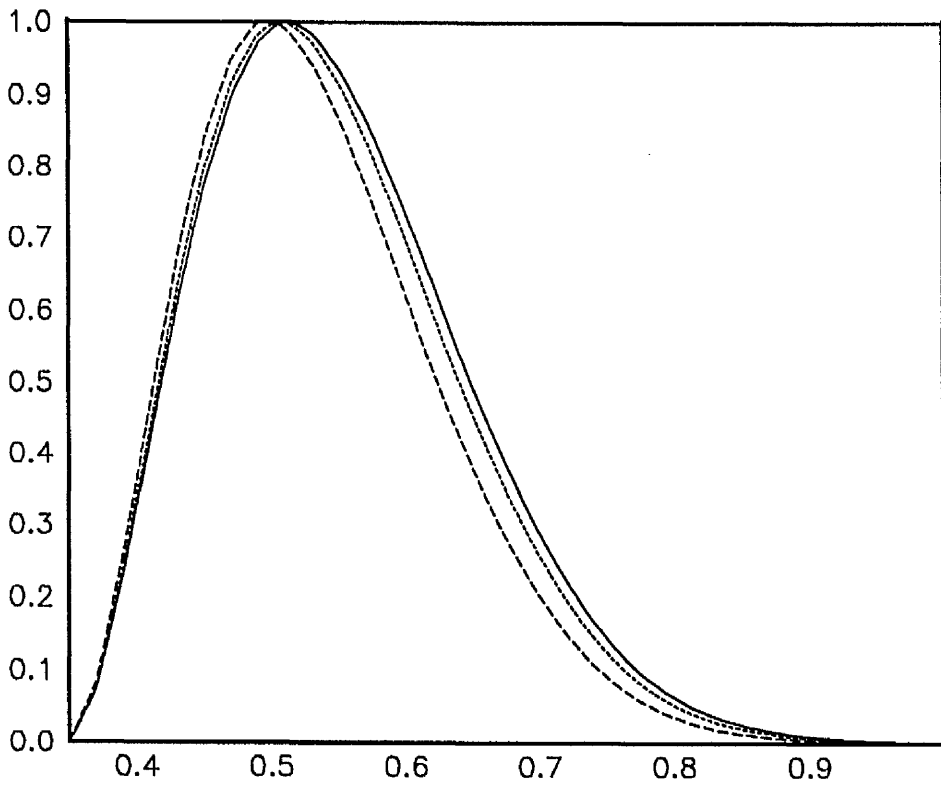


Figure 3.11: As Figure 3.3 but for the cases  $\gamma = 1, 2$  and  $3$  of Figure 3.10.

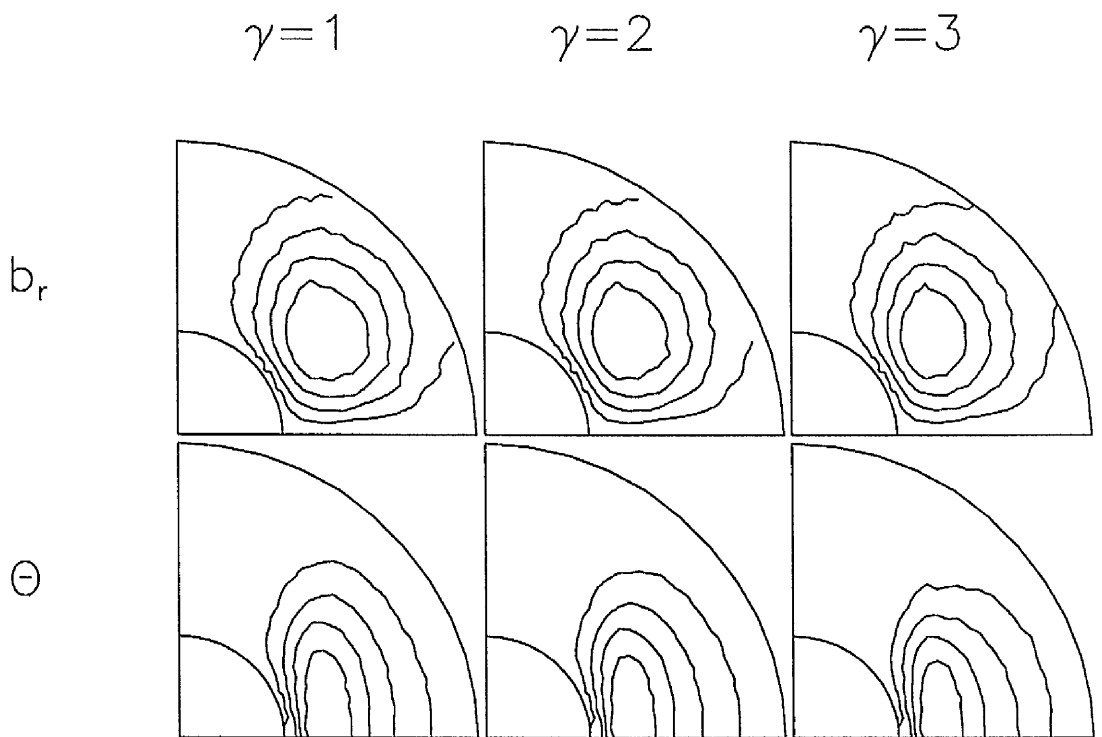


Figure 3.12: As Figure 3.10 but with dipole parity.  $R_c$  values here are 36.5689, 45.8098 and 61.9000 for  $\gamma = 1, 2$  and 3 respectively.

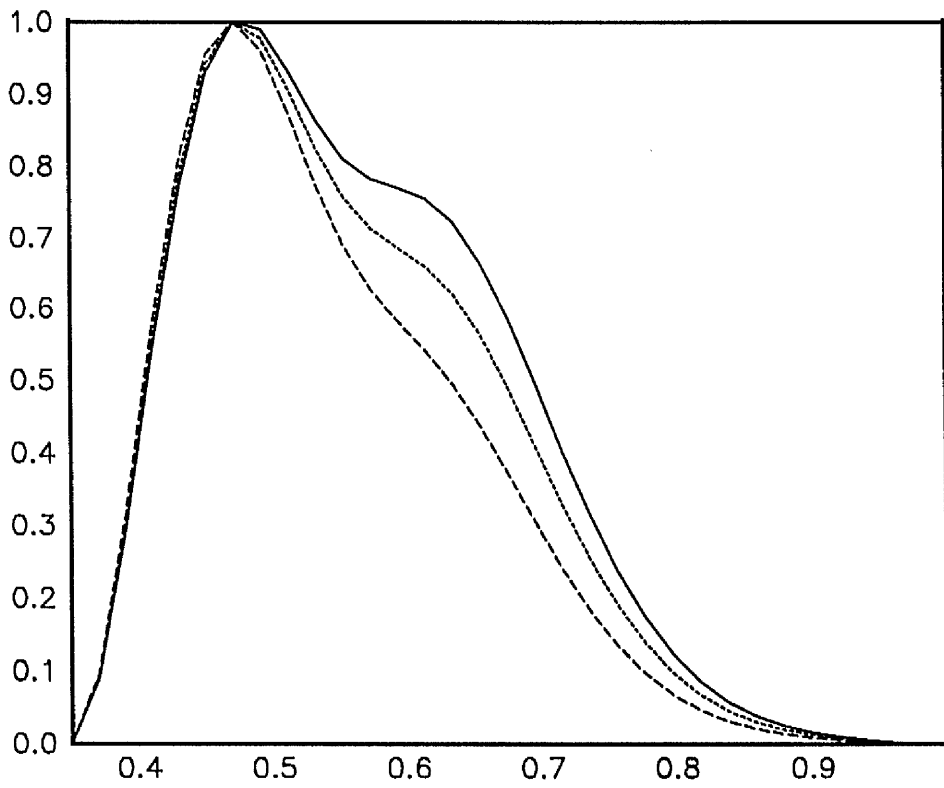


Figure 3.13: As Figure 3.3 but for the cases  $\gamma = 1, 2$  and  $3$  of Figure 3.12.

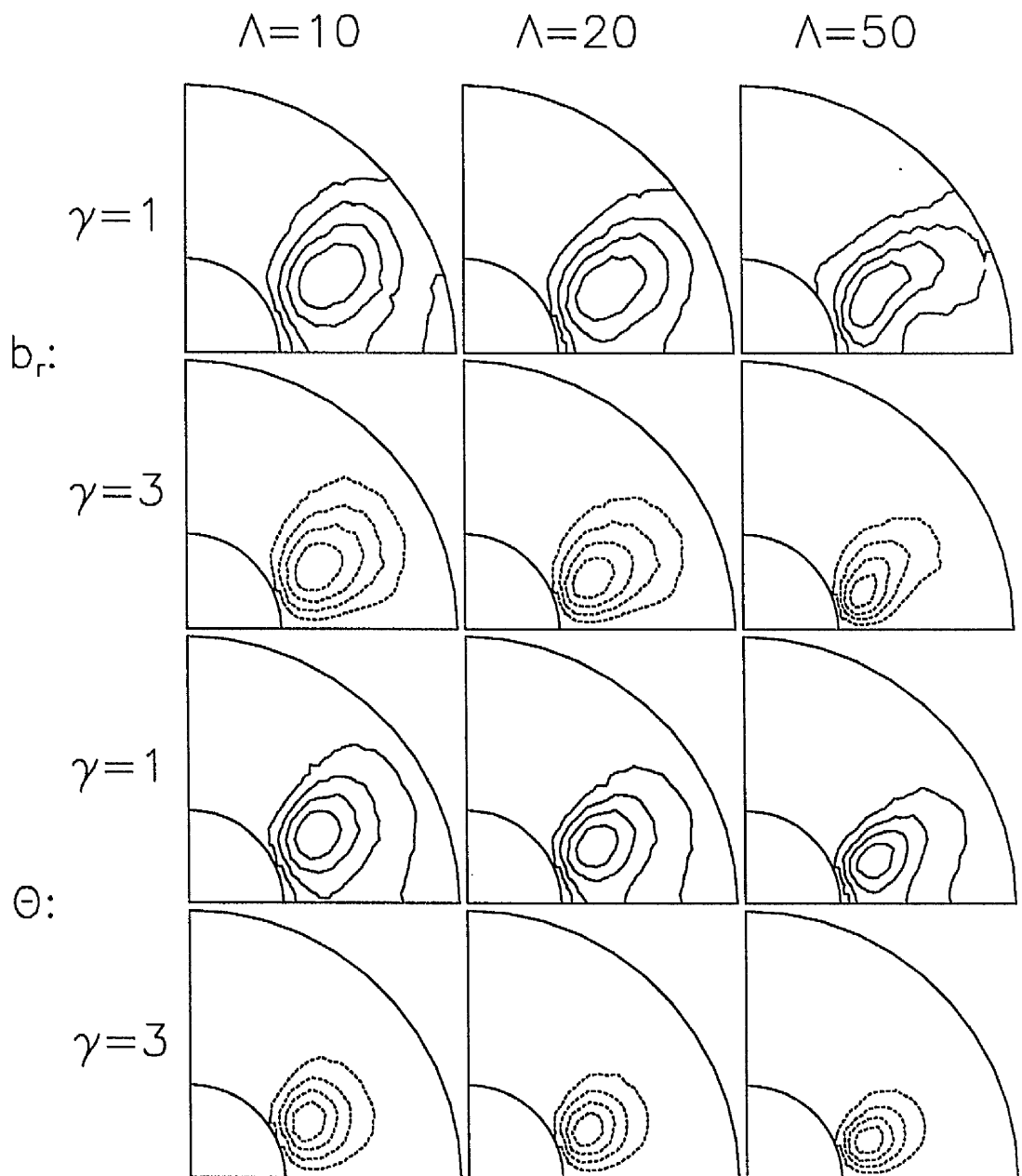


Figure 3.14: Eigenfunctions of  $b_r$  and  $\vartheta$  with  $\gamma = 1$  (full line) and  $\gamma = 3$  (dashed line), for magnetic field strengths  $\Lambda = 10, 20$  and  $50$ ,  $m = 3$  and quadrupole parity. These have  $R_c$  values of 206.683, 273.304 and 405.855 ( $\gamma = 1$  and increasing  $\Lambda$ ), and 358.550, 440.309 and 586.344 ( $\gamma = 3$  and increasing  $\Lambda$ ).

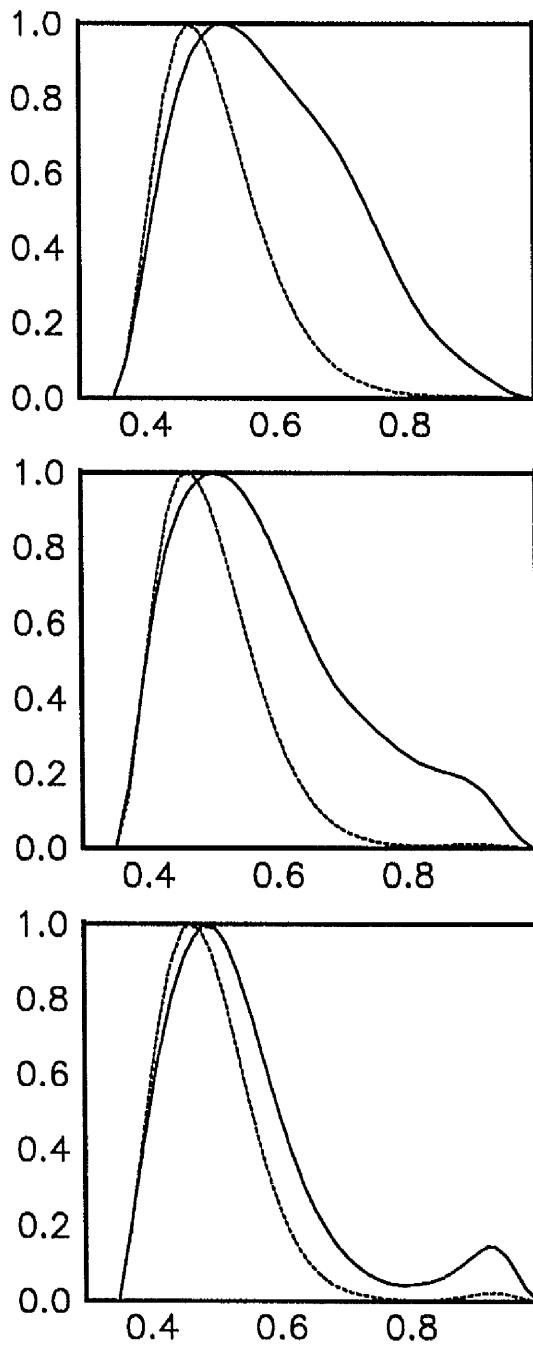


Figure 3.15: Graphs of  $u_r^2$  against  $r$  for from top to bottom  $\Lambda = 10, 20$  and  $50$  respectively, for the modes of Figure 3.14.

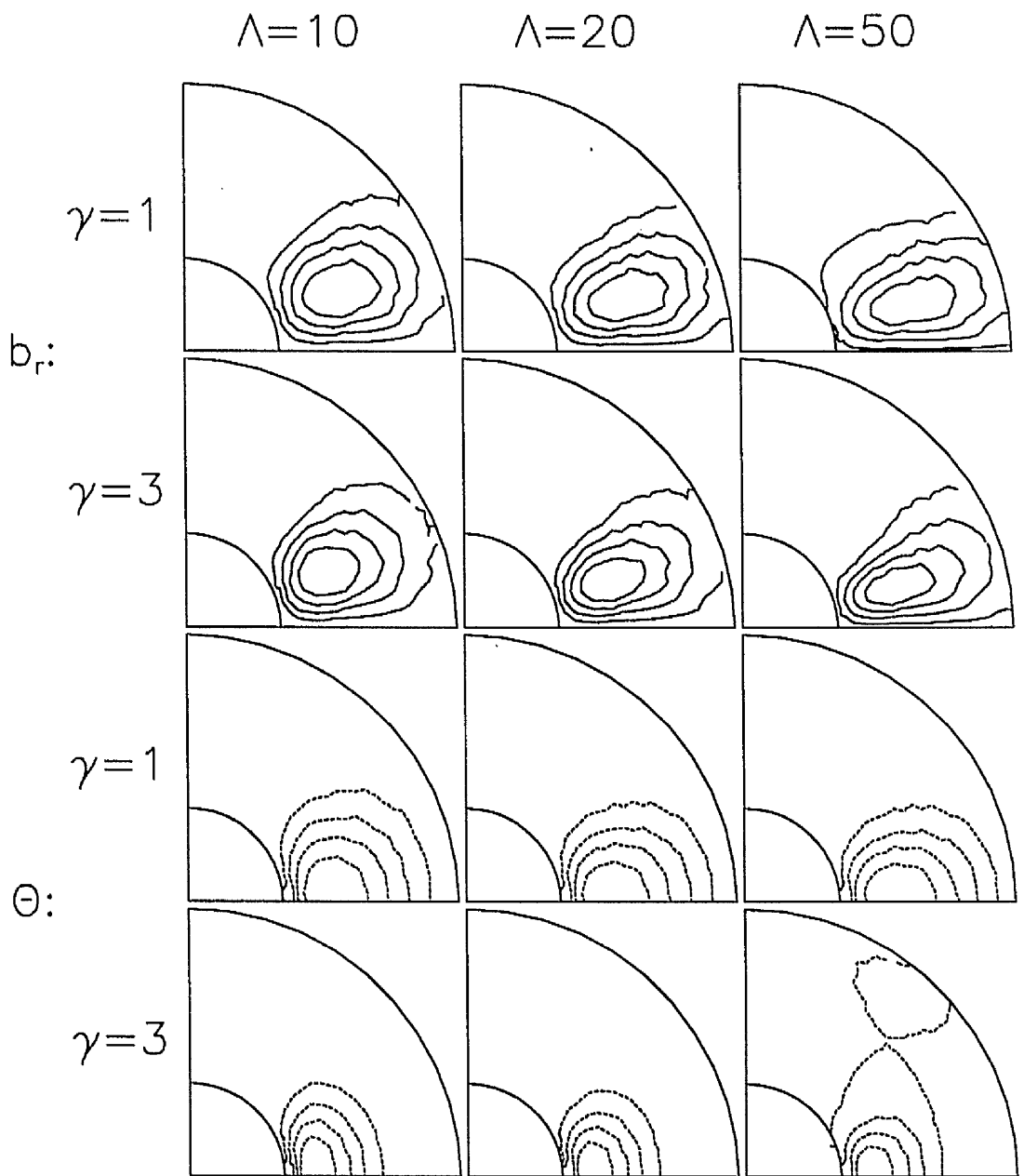


Figure 3.16: As Figure 3.14 but with dipole parity.  $R_c$  values here are 42.5965, 46.4757 and 40.0365 ( $\gamma = 1$  and increasing  $\Lambda$ ), and 98.0094, 118.052 and 151.365 ( $\gamma = 3$  and increasing  $\Lambda$ ).

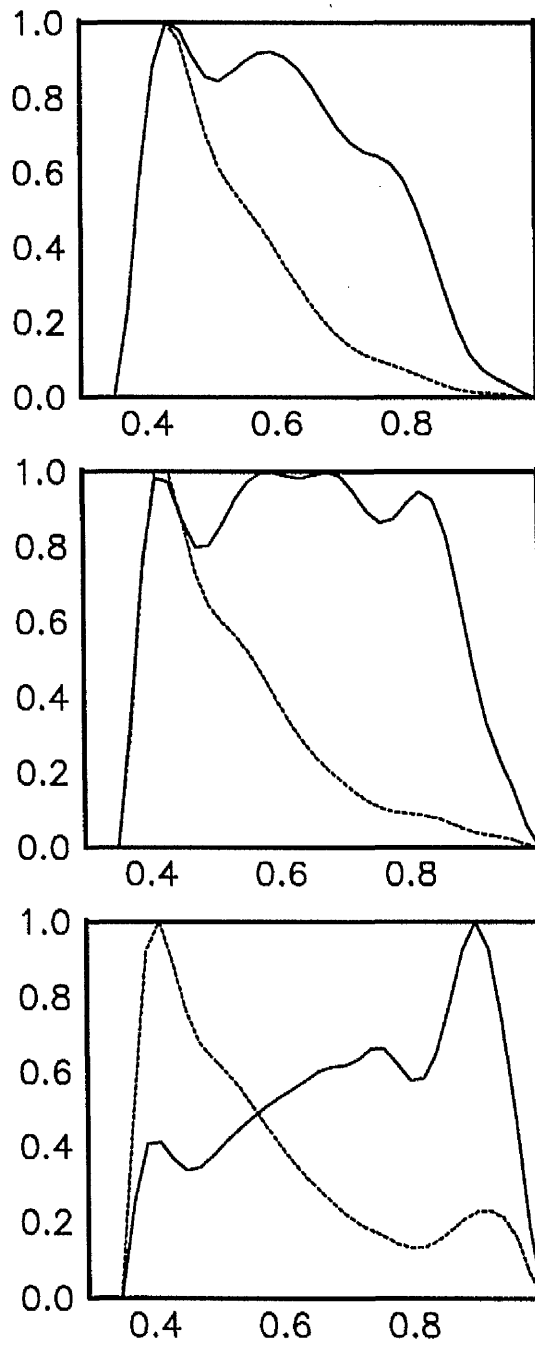


Figure 3.17: As Figure 3.15 but for the modes of Figure 3.16.

ing a stably stratified layer has the effect of trying to suppress convection in the stable layer. This acts to force a  $z$ -dependence on the motion, which conflicts with the Taylor-Proudman theorem. As a result we find in the case of a sphere that convection continues to penetrate into the stable region. The reason why this behaviour was not seen for a cylindrical geometry is that in that case there was no conflict between the introduction of a stable layer and the constraints of the Taylor-Proudman theorem. Since the stable layer is parallel to the  $z$ -axis in the cylinder, with the driving perpendicular to the rotation axis, convection, although suppressed in the stable part, can still maintain a  $z$ -independent structure. In the plane layer models of Boda and Ševčík, there is, as in the sphere, a conflict between the constraints of the stable layer and the Taylor-Proudman theorem, since the stable layer is perpendicular to the axis of rotation, with the thermal driving in this case being parallel to the rotation axis. We would expect therefore that the results for a plane layer geometry would be the same as those found for a sphere, and in particular that for  $\Lambda \ll 1$ , Boda and Ševčík, who only considered  $m \leq 5$ , would have found no suppression of convection in the stable layer, even if they had considered  $m_c$ .

When we have a magnetic field strength that is no longer small,  $\Lambda \geq O(1)$ , our findings are in agreement with past results. For  $\Lambda = 1$  we find that a stable layer has very little effect on convection, but when  $\Lambda \gg 1$ , convection concentrates in the unstably stratified fluid. Fearn and Richardson observed that localisation is associated with a short lengthscale perpendicular to the temperature gradient, and this is also the case here. They found that for  $\Lambda < O(1)$ , the azimuthal wave number  $m \gg 1$ , and for  $\Lambda \gg 1$ , there was a shortening of the lengthscale in the other perpendicular direction (the  $z$ -direction). In the spherical problem, the “other perpendicular direction” is the  $\theta$  direction, and indeed we find a shortening in the  $\theta$  lengthscale as  $\Lambda$  is increased (see Figures 3.14 and 3.16).

As far as the Earth’s magnetic field is concerned, the presence of a stably stratified layer at the CMB does not preclude convection from that region unless

the field is strong. If the Earth's field is not too strong,  $\Lambda \leq O(1)$ , then the presence of, or lack of convective motion at the CMB gives us no information as to whether or not such a stable region exists.

# Chapter 4

## Magnetic field expulsion into a conducting mantle

### 4.1 INTRODUCTION

In this chapter we consider a different problem. We look at a 2D numerical model of the expulsion of magnetic field from the Earth's core into a conducting mantle, driven by a prescribed upwelling fluid motion. We consider different possible conductivity profiles for the mantle, and compare with the fully insulating mantle solution as studied by Bloxham (1986). Motivated by recent work on the conductivity of the lower mantle, we later look at a conductivity profile with large lateral heterogeneity in conductivity.

Most studies of the Earth's core have in the past assumed that the mantle is electrically insulating. This has been a reasonable assumption, and a simple one to apply mathematically, but as models have become more complex, and our knowledge of the internal structure, composition and dynamics of the Earth's deep interior have increased, it becomes possible, and indeed necessary, to consider a more realistic conductivity for the mantle. There have been many studies which have considered a conducting mantle, and suggested profiles for the conductivity (e.g., Braginsky and Fishman 1976; Alldredge 1977; Ducruix, Courtillot and Le Mouél 1980; Benton and Whaler 1983; Fearn and Proctor 1992). The main approaches have been to either divide the mantle into layers of uniform conductivity, or to assume a radial power law of decreasing conductivity. The

conductivity of the mantle is not well known, and because of this it is necessary to choose simple representative models.

There has been considerable argument over the magnitude of mantle conductivity. Ducruix et al (1980) reported that mantle conductivity could not exceed  $100 \text{ Sm}^{-1}$  over any appreciable thickness, from an analysis of the secular variation impulse in the late 1960's. High pressure - high temperature experiments have been performed, testing the conductivity of the materials thought to be present in the lower mantle, under conditions simulating as close as possible those in the mantle. These have given conflicting estimates:- Li and Jeanloz (1987) put an upper bound of  $10^{-2} \text{ Sm}^{-1}$  on mantle conductivity between depths of 700 and 1900km, whereas Peyronneau and Poirier (1989) found conductivity to be  $\sim 1 \text{ Sm}^{-1}$  at a depth of 1000km, and obtained a lower bound of  $\sim 70 \text{ Sm}^{-1}$  at the core-mantle boundary. Despite the lack of agreement over conductivity values, it is more generally agreed that in the  $D''$  layer at the bottom of the mantle [ $\sim 200 - 300 \text{ km}$  thick (Young and Lay 1987)], there may be appreciable amounts of iron from the core present, resulting in a much higher conductivity in that layer [ $O(10^4 \text{ Sm}^{-1})$  Li and Jeanloz 1987]. Indeed, recent evidence (Jeanloz 1990) suggests that there could be large lateral heterogeneity in conductivity in this layer, with changes from metallic conductivity to virtually insulating material over a very short lengthscale. In our later results (Section 4.4.3) we attempt to model this lateral variation.

Our main aim here is to model the effects of mantle conductivity. To do this we extend the model of Bloxham (1986) to consider a conducting mantle. Bloxham solved the magnetic induction equation

$$\frac{\partial \mathbf{B}}{\partial t} = \nabla \times (\mathbf{U}_0 \times \mathbf{B}) + \eta \nabla^2 \mathbf{B} \quad (4.1)$$

for the magnetic field  $\mathbf{B}$  with a prescribed flow  $\mathbf{U}_0$ . He studied the expulsion of a uniform horizontal magnetic field from the core into the mantle, citing this process as a possible mechanism for an observed feature of the Earth's magnetic field,

namely a reversed flux patch over Southern Africa (see Bloxham and Gubbins 1985). We consider the same problem here, but instead of the mantle taken to be insulating, we consider a conducting layer of variable thickness and conductivity. Above this conducting layer the rest of the mantle is taken to be insulating.

## 4.2 MODEL

We consider a 2D kinematic model for the expulsion of magnetic field from the core into the mantle. We use Cartesian coordinates with  $x$  horizontal and  $z$  vertical, taking the system to be independent of  $y$  for simplicity. We have a plane layer model, unbounded horizontally, and split vertically into two layers. At the bottom we have a layer of height  $L$  representing the outer core. In this layer we have a prescribed flow  $\mathbf{U}_0$ , and a magnetic diffusivity  $\eta_c$  which is taken to be constant. Above this we have a layer representing the lower part of the mantle, which is not to be confused with the common definition of lower mantle, understood to be the part of the mantle below  $670\text{km}$ . This layer is of height  $\epsilon L$ , where we can choose  $\epsilon$  arbitrarily, and we prescribe the magnetic diffusivity here arbitrarily as  $\eta_m = f(x, z)$ . There is no flow in the mantle layer. Above this conducting layer, the upper mantle is taken to be insulating.

### 4.2.1 Governing equations

We solve numerically the magnetic induction equation in each layer.

$$\left. \begin{aligned} \frac{\partial \mathbf{B}}{\partial t} &= \nabla \times (\mathbf{U}_0 \times \mathbf{B}) + \eta_c \nabla^2 \mathbf{B} && \text{(core)} \\ -\frac{\partial \mathbf{B}}{\partial t} &= \nabla \times (\eta_m \nabla \times \mathbf{B}) && \text{(lower mantle)} \end{aligned} \right\} \quad (4.2)$$

If we write  $\mathbf{B} = \nabla \times \mathbf{A}$  where

$$\mathbf{A} = A(x, z, t) \mathbf{1}_y \quad (4.3)$$

then on "uncurling" (4.2) we obtain

$$\left. \begin{aligned} \frac{\partial A}{\partial t} &= -\mathbf{U}_0 \cdot \nabla A + \eta_c \nabla^2 A && \text{(core)} \\ \frac{\partial A}{\partial t} &= \eta_m \nabla^2 A && \text{(lower mantle)} \end{aligned} \right\} \quad (4.4)$$

Expressing  $\mathbf{U}_0$  in terms of a streamfunction  $\psi$

$$\mathbf{U}_0 = \left( -\frac{\partial \psi}{\partial z}, 0, \frac{\partial \psi}{\partial x} \right) \quad (4.5)$$

(4.4) then gives us

$$\left. \begin{aligned} \frac{\partial A}{\partial t} - \eta_c \nabla^2 A &= \frac{\partial A}{\partial x} \frac{\partial \psi}{\partial z} - \frac{\partial A}{\partial z} \frac{\partial \psi}{\partial x} && \text{(core)} \\ \frac{\partial A}{\partial t} &= \eta_m \nabla^2 A && \text{(lower mantle)} \end{aligned} \right\} \quad (4.6)$$

We non-dimensionalise this using the timescale of magnetic diffusion  $\tau_\eta = L^2/\eta_c$ , lengthscale  $L$  and velocity  $U$  giving

$$\left. \begin{aligned} \frac{\partial A}{\partial t} - \nabla^2 A &= R_m \left( \frac{\partial A}{\partial x} \frac{\partial \psi}{\partial z} - \frac{\partial A}{\partial z} \frac{\partial \psi}{\partial x} \right) && \text{(core)} \\ \frac{\partial A}{\partial t} &= \eta \nabla^2 A && \text{(lower mantle)} \end{aligned} \right\} \quad (4.7)$$

where our magnetic Reynolds number  $R_m$  is defined as

$$R_m = \frac{UL}{\eta_c} \quad (4.8)$$

and  $\eta = \eta_m/\eta_c$  is a diffusivity ratio.

In our non-dimensional coordinates, our rectangular region representing the core and lower mantle goes from  $z = -1$  at the base, through  $z = 0$  at the core-mantle boundary up to  $z = \epsilon$  at the top, and with  $x$  ranging from 0 to  $2\alpha$  where

$\alpha$  is a width to height ratio of a convection roll. We solve numerically with a spectral collocation method in  $x$  (see e.g, Orszag 1972; Wengle, Van den Bosch and Seinfeld 1978; Gottlieb and Orszag 1981), and we use second-order finite differences in  $z$  with semi-implicit timestepping. We use  $N$  collocation points in  $x$ , namely

$$x_j = \frac{2\alpha}{N}(j-1) \quad (1 \leq j \leq N) \quad (4.9)$$

where we are insisting that the equations be satisfied exactly at these points. We also have  $L$  and  $M$  grid points in  $z$  in the lower and upper layers respectively, namely

$$\begin{aligned} z_k &= -1 + \frac{k}{L} & (1 \leq k \leq L) & \quad (\text{core layer}) \\ z_{L+k} &= k \frac{\epsilon}{M} & (1 \leq k \leq M) & \quad (\text{conducting layer}) \end{aligned} \quad (4.10)$$

This scheme differs from that used in Bloxham (1986), in that he used Fourier transforms in  $x$  where we have used collocation.

We expand our magnetic potential  $A$  as

$$A(x_j, z_k, t) = \sum_{n=1}^N A_n(z_k, t) \exp\left(\frac{i(n-1)\pi x_j}{\alpha}\right) \quad (4.11)$$

and substitute this into (4.7) together with the appropriate second order finite-difference approximations

$$\frac{\partial A}{\partial t} \rightarrow \frac{A_{n,l}^{i+1} - A_{n,l}^i}{\delta t} \quad (4.12)$$

$$\frac{\partial^2 A}{\partial z^2} \rightarrow \left( \frac{A_{n,l+1}^{i+1} - 2A_{n,l}^{i+1} + A_{n,l-1}^{i+1}}{2\delta z^2} \right) + \left( \frac{A_{n,l+1}^i - 2A_{n,l}^i + A_{n,l-1}^i}{2\delta z^2} \right) \quad (4.13)$$

$$\frac{\partial A}{\partial z} \rightarrow \frac{A_{n,l+1}^i - A_{n,l-1}^i}{2\delta z} \quad (4.14)$$

$$A \rightarrow \begin{cases} \frac{A_{n,l}^{i+1} + A_{n,l}^i}{2} & \text{(only from } \nabla^2 A \text{ term)} \\ A_{n,l}^i & \text{(otherwise)} \end{cases} \quad (4.15)$$

where

$$A_{n,l}^i = A_n(z_l, t_i) \quad (4.16)$$

$t_i$  = time after  $i$  timesteps

and where we are using semi-implicit timestepping; treating the  $\nabla^2$  term implicitly and the rest explicitly.

#### 4.2.2 Boundary conditions

Above our conducting layer, the upper mantle is taken to be electrically insulating so we impose an insulating boundary condition at  $z = \epsilon$ . The inner core is assumed to be a perfect electrical conductor, and so we impose a perfectly conducting boundary condition at  $z = -1$ . We impose periodic boundary conditions at the sides. The boundary conditions at the perfectly conducting lower boundary and at the sides are easily obtained, but the condition at the top boundary requires further explanation. At the top we have an insulating upper mantle. In this insulating region,  $z > \epsilon$ , we have a potential field, and the equation for the magnetic potential  $A$  is simply

$$\nabla^2 A = 0 \quad (4.17)$$

We can solve (4.17) explicitly for the solution in the insulating part of the mantle which we find to be

$$A^{ins}(x, z) = \sum_{n=1}^N A_n^{ins} \exp\left(\frac{-(n-1)\pi z}{\alpha}\right) \exp\left(\frac{i(n-1)\pi x}{\alpha}\right) \quad (4.18)$$

whereas in the conducting layer the magnetic potential has form

$$A^{con}(x, z) = \sum_{n=1}^N A_n^{con}(z, t) \exp\left(\frac{i(n-1)\pi x}{\alpha}\right) \quad (4.19)$$

In equations (4.18) and (4.19) above, the use of *ins* and *con* as a superscript, relates to the solution being in the insulating and conducting regions respectively.

The condition at the boundary is that we make  $\mathbf{B}$  continuous. Matching  $B_x$  components above and below the boundary gives

$$\frac{\partial A_n^{con}}{\partial z} = \frac{-(n-1)\pi}{\alpha} A_n^{ins} \quad (1 \leq n \leq N) \quad (4.20)$$

and similarly matching  $B_z$  components gives us

$$A_n^{con} = A_n^{ins} \quad (1 \leq n \leq N) \quad (4.21)$$

From (4.20) and (4.21) we obtain the boundary condition for the magnetic potential  $A$  of the conducting layer at the top insulating boundary, namely

$$\frac{\partial A_n}{\partial z} = \frac{-(n-1)\pi}{\alpha} A_n \quad (4.22)$$

which is the expression we employ.

In finite-difference form, the boundary conditions can be written as

**Top:**

$$A_{n, L+M+1} = A_{n, L+M-1} - 2\delta z(n-1)\frac{\pi}{\alpha} A_{n, L+M} \quad (1 \leq n \leq N) \quad (4.23)$$

**Bottom:**

$$A_{n,1} = 0 \quad (1 \leq n \leq N) \quad (4.24)$$

**Sides:**

$$A_{N+1,l} = A_{1,l} (1 \leq l \leq L + M) \quad (4.25)$$

These apply at all  $t_i$ .

### 4.2.3 Matching the solution between the layers

At the boundary between the core and the mantle we must match the solutions from each layer. To do this we must make  $\mathbf{B}$  continuous at the boundary, which is equivalent to making both  $\frac{\partial A}{\partial x}$  and  $\frac{\partial A}{\partial z}$  continuous there. Since in both layers we have chosen a spectral representation in  $x$  of form (4.11), by making  $A$  continuous at the boundary we automatically satisfy  $\frac{\partial A}{\partial x}$  continuity. For the  $z$ -derivative we have

$$\frac{\partial A_{core}}{\partial z} = \frac{\partial A_{mantle}}{\partial z} \quad (z = 0) \quad (4.26)$$

We substitute the standard second order backward difference approximation for  $\frac{\partial A}{\partial z}$  in the core layer,

$$\frac{\partial A_{core}}{\partial z} \rightarrow \frac{3A_{n,L} - 4A_{n,L-1} + A_{n,L-2}}{2\delta z_1} \quad (4.27)$$

and similarly substitute a second order forward difference approximation to  $\frac{\partial A}{\partial z}$  in the mantle layer

$$\frac{\partial A_{mantle}}{\partial z} \rightarrow \frac{-3A_{n,L} + 4A_{n,L+1} - A_{n,L+2}}{2\delta z_2} \quad (4.28)$$

and hence obtain a matching condition

$$A_{n,L} = \frac{4\delta z_1 A_{n,L+1} + 4\delta z_2 A_{n,L-1} - \delta z_1 A_{n,L+2} - \delta z_2 A_{n,L-2}}{3(\delta z_1 + \delta z_2)} \quad (4.29)$$

where  $\delta z_1, \delta z_2$  are our  $z$ -gridding intervals in core and mantle layers respectively.

#### 4.2.4 Method of solution

When in matrix form our problem is

$$\mathbf{C} \mathbf{A}_{t=i} = \mathbf{D} \mathbf{A}_{t=i+1} \quad (4.30)$$

where  $\mathbf{C}$  and  $\mathbf{D}$  are  $[N \times (L+M)] \times [N \times (L+M)]$  matrices formed from our finite difference equations. They are banded in structure, and this was used to save on storage.  $\mathbf{A}_{t=i}$  is the column vector of the magnetic potential in its spectral representation. We initialise  $\mathbf{A}_{t=0}$  from our initial field by calculating the spectral coefficients from equation (4.11). We choose an initial field which is uniform and horizontal. In terms of the magnetic potential  $A$ , our choice is given by

$$A = 1 - z \quad (4.31)$$

To calculate the spectral representation of this field, we have to solve a linear system of equations [formed from equation (4.11)] of form

$$\mathbf{A}_{field} = \mathbf{E} \mathbf{A}_{spectral} \quad (4.32)$$

where  $\mathbf{A}_{field}$  is a column vector of the actual magnetic potential, and  $\mathbf{A}_{spectral}$  ( $\equiv \mathbf{A}_{t=0}$ ) is the column vector of its spectral representation.  $\mathbf{E}$  is an  $[N \times (L+M)] \times [N \times (L+M)]$  matrix of complex exponentials which is also banded in structure. The same numerical routines used later in the solving of (4.30) were used to solve

(4.32). We solve (4.30) by firstly multiplying through the left hand side, and then solving the resulting linear system of equations for  $\mathbf{A}$  at the next timestep. At any point we can output the vector  $\mathbf{A}$ , and after reconstructing the magnetic potential from the spectral coefficients we can plot the magnetic field lines as contours of  $A$ .

#### 4.2.5 Numerical stability of the model

The numerical system we employ is stable, as long as the timestep is sufficiently small and the diffusivity ratio  $\eta$  is not too large. As  $\eta$  is increased the local magnetic diffusion timescale in the conducting layer becomes smaller, and if  $\eta$  becomes too large then the solution fails in the conducting layer because of this, unless the timestep is decreased accordingly. The timestep that we used of  $5 \times 10^{-5}$  sufficed for  $\eta < 10^5$ , and since when  $\eta = 10^3$  we find that behaviour is similar to the fully insulating case (see Section 4.4), there is no need to increase  $\eta$  far beyond that.

#### 4.2.6 Mantle field

It is of further interest to us to observe the magnetic field lines when they enter the insulating part of the mantle. In the insulating region we have a potential field, and in Section 4.2.2 we found the explicit solution to be

$$A(x_j, z_k) = \sum_{n=1}^N A_n \exp\left(\frac{-(n-1)\pi z_k}{\alpha}\right) \exp\left(\frac{i(n-1)\pi x_j}{\alpha}\right) \quad (4.33)$$

The coefficients  $A_n$  can be determined by matching to the solution in the lower (conducting part of the) mantle. We can then use (4.33) to determine the field in the upper (insulating part of the) mantle. We include this in our solution plots.

### 4.3 CHECKING CASES

Before proceeding to a full investigation of our model, it is necessary to check our numerical code with simpler checking cases. Firstly we consider the

case where we simply allow the field to decay with no flow in the core. We also can compare with the work of Bloxham (1986) by looking at the fully insulating mantle case.

#### 4.3.1 Decay time

If we have a zero flow in the core, obtained by setting  $R_m = 0$ , and prescribe an initial field  $\mathbf{B} = B(z, t)\mathbf{1}_x$  that is purely horizontal, then we can solve for the magnetic field analytically and compare the numerical decay time for the field with the theoretically calculated value. For example, if we consider the simple model which will be used in Section 4.3.2 below, where we have a purely insulating mantle, then the equation for the magnetic field in the core simplifies to

$$\frac{\partial B}{\partial t} = \frac{\partial^2 B}{\partial z^2} \quad (4.34)$$

with boundary conditions

$$z = -1 : \quad \frac{\partial B}{\partial z} = 0 \quad (4.35)$$

$$z = 0 : \quad B = 0 \quad (4.36)$$

We assume  $B$  decays exponentially as  $\exp(-pt)$ , and hence find the solution to be

$$B = C \cos(\sqrt{p}(z + 1)) \exp(-pt) \quad (4.37)$$

where  $C$  is an arbitrary constant chosen to be 1, and also

$$\sqrt{p} = \frac{(2n + 1)\pi}{2} \quad n = 0, 1, 2, \dots \quad (4.38)$$

If we choose the fundamental mode of solution, corresponding to  $n = 0$ , and assign our initial field with this accordingly,

$$B = \cos\left(\frac{\pi}{2}(z + 1)\right) \quad (4.39)$$

then we expect this field to decay as  $\exp(-\frac{\pi^2}{4}t)$ .

The analysis for the model with a conducting layer of constant diffusivity  $\eta$  is more complicated but can be done in a similar way. The equations for the magnetic field in this case are

$$\left. \begin{aligned} \frac{\partial B}{\partial t} &= \frac{\partial^2 B}{\partial z^2} && \text{(core)} \\ \frac{\partial B}{\partial t} &= \eta \frac{\partial^2 B}{\partial z^2} && \text{(lower mantle)} \end{aligned} \right\} \quad (4.40)$$

with boundary conditions

$$z = -1 : \quad \frac{\partial B}{\partial z} = 0 \quad (4.41)$$

$$z = \epsilon : \quad B = 0 \quad (4.42)$$

At  $z = 0$  we must match the solutions from each layer. We require 2 continuity conditions. We obtain the first by matching  $B_x$  at the boundary, and this takes the form

$$B_{core} = B_{mantle} \quad (4.43)$$

The second condition at  $z = 0$  is obtained by matching the tangential component of the electric field at the boundary. This yields

$$\frac{\partial B_{core}}{\partial z} = \eta \frac{\partial B_{mantle}}{\partial z} \quad (4.44)$$

Again we assume that  $B$  decays exponentially as  $\exp(-pt)$ , and hence we find the solution to be

$$\left. \begin{aligned} B &= C_1 \cos(\sqrt{p}z + \delta_1) && \text{(core)} \\ B &= C_2 \cos\left(\sqrt{\frac{p}{\eta}}z + \delta_2\right) && \text{(lower mantle)} \end{aligned} \right\} \quad (4.45)$$

where  $C_1, C_2, \delta_1$  and  $\delta_2$  are constants to be determined from the boundary conditions. Applying (4.41) tells us that

$$\delta_1 = \sqrt{p} \quad (4.46)$$

and from (4.42) we deduce that

$$\delta_2 = -\sqrt{\frac{p}{\eta}} + (2n + 1)\frac{\pi}{2} \quad n = 0, 1, 2, \dots \quad (4.47)$$

Again we choose the most basic mode of solution corresponding to  $n = 0$ . From equation (4.43) we get

$$C_1 \cos \sqrt{p} = C_2 \cos \left( \frac{\pi}{2} - \sqrt{\frac{p}{\eta}} \epsilon \right) \quad (4.48)$$

and similarly (4.44) gives us

$$C_1 \sin \sqrt{p} = C_2 \sqrt{\eta} \sin \left( \frac{\pi}{2} - \sqrt{\frac{p}{\eta}} \epsilon \right) \quad (4.49)$$

and combining (4.48) and (4.49) provides us with the following equation for  $\sqrt{p}$

$$\tan \sqrt{p} - \sqrt{\eta} \tan \left( \frac{\pi}{2} - \sqrt{\frac{p}{\eta}} \epsilon \right) = 0 \quad (4.50)$$

A simple application of the bisection method was used to find  $\sqrt{p}$  for given  $\epsilon$  and  $\eta$ .

Having found  $\sqrt{p}$  we use equation (4.47) to obtain  $\delta_2$ . We have freedom to choose one of the constants  $C_1$  or  $C_2$  since the problem is linear in  $B$ . We choose  $C_1$  to be 1, and calculate  $C_2$  from either (4.48) or (4.49). We then choose as initial field

$$\left. \begin{aligned} B &= \cos(\sqrt{p}(z+1)) && \text{(core)} \\ B &= C_2 \cos\left(\sqrt{\frac{p}{\eta}}\left(z - \epsilon + \frac{\pi}{2}\right)\right) && \text{(lower mantle)} \end{aligned} \right\} \quad (4.51)$$

This field should then decay exponentially as  $\exp(-pt)$ .

To obtain the decay rate from our model, we must calculate the horizontal magnetic field strength  $B_x$ , and see how this changes over time. Since  $B_x = -\frac{\partial A}{\partial z}$ , we obtain  $B_x$  from our magnetic potential  $A$  by approximating the  $z$ -derivative. The decay rate can then be calculated from a graph of  $B_x$  against time. We calculate the decay rate at the midpoints of both the core and mantle layers. The numerical decay rates we find in each layer are almost identical, the slight differences being due to numerical inaccuracies. We show comparisons of theoretical and numerical decay rates for several layer sizes and diffusivities in Table 4.1. We find that there is excellent agreement between the predicted and actual decay rates for our model over the full range of parameters used for our results. This gives us confidence in the model to proceed to the full problem.

### 4.3.2 Comparison with Bloxham's results

We can check much of the numerical code by considering the case of a fully insulating mantle. This problem was studied by Bloxham (1986), and we can compare our results with his. To do this we remove the conducting layer from

$\epsilon$	$\eta$	$\sqrt{p}$ (theoretical)	$\sqrt{p}$ core	$\sqrt{p}$ mantle
0	$\infty$	1.5708	1.5704	-
0.1	1	1.4280	1.4281	1.4284
0.1	10	1.5552	1.5550	1.5561
0.5	10	1.4948	1.4947	1.4957
0.5	100	1.5630	1.5627	1.5626
1.0	100	1.5551	1.5549	1.5550
1.0	1000	1.5692	1.5690	1.5695

Table 4.1: Values of the theoretical and numerical decay rates for a variety of layer sizes and diffusivity ratios. Numerical values were obtained by calculating the horizontal magnetic field strength in the middle of both the core and mantle layers.

our model, solving in the core as described in Section 4.2, but applying the insulating boundary condition (4.22) at the core-mantle boundary. Again we add on top the explicit solution in the insulating region as in Section 4.2.6. On running this program over a range of parameters we find good agreement with Bloxham's results. As an illustration, if we choose the same parameters as in Figure 5 of Bloxham (1986), an initially uniform horizontal field,  $R_m = 50$  and streamfunction

$$\psi = \frac{1}{\pi} \sin \frac{\pi x}{\alpha} \sin \pi z \quad (4.52)$$

then the behaviour that we see (Figure 4.1) is consistent with Bloxham's results. In this figure, the first four contour plots are taken at the same times as the four in Figure 5 of Bloxham (1986). The field evolves in the same way as in Bloxham's results, although our solution takes slightly longer to reach the same state. This could be due to the differences between our two numerical schemes or the truncations used, but apart from this discrepancy the behaviour is the same for both models. Having recreated these results we can move on to encompass the main interest of this work, namely a finitely conducting mantle.

#### 4.4 RESULTS

We consider various models of conductivity for our conducting layer. We do this by defining different profiles for the diffusivity ratio  $\eta$ . These fall into three categories.

(a)  $\eta = \text{constant}$ ,

(b)  $\eta = f(z)$ ,

(c)  $\eta = g(x)$ ,

All our results here are with  $R_m = 50$ , a timestep of  $5 \times 10^{-5}$  and streamfunction (4.52). This choice of streamfunction represents an upwelling motion up the middle of the layer which drives the expulsion process. Our choice of  $R_m = 50$

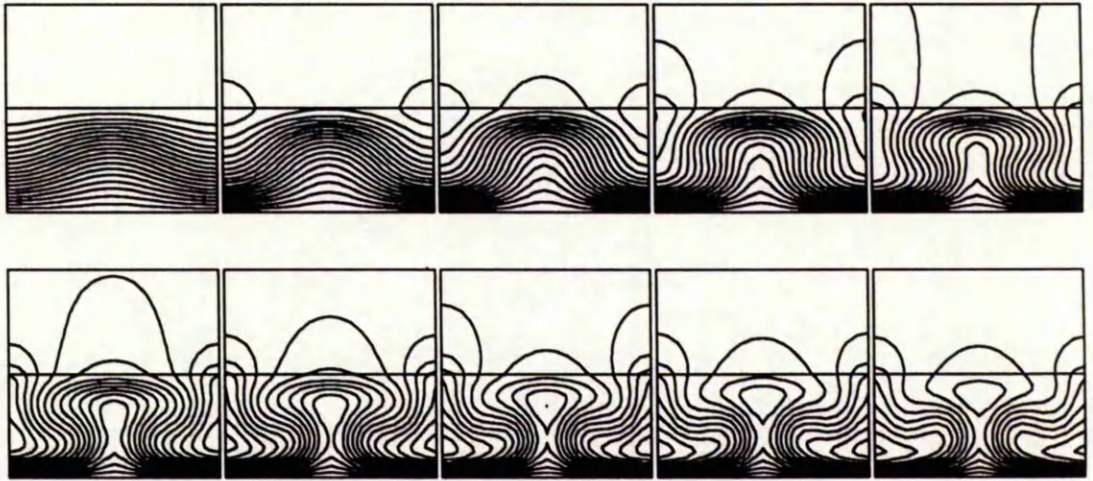


Figure 4.1: A plot of the evolution of the magnetic field, as a contour map of the magnetic potential  $A$ , with a fully insulating mantle, with  $N = L = M = 20$ ,  $R_m = 50$  and streamfunction (4.52). The timestep here is  $5 \times 10^{-5}$  and a picture is taken every 100 timesteps. The upper part is the extrapolation through the mantle of the solution obtained analytically for the insulating region as explained in Section 4.2.6.

is somewhat arbitrary, but we are looking at a variety of conductivities here, so feel justified in choosing a particular value of  $R_m$  as it is not possible to consider too many varying parameters. The choice of timestep is one which gives stable solutions for values of  $\eta$  considered here, and also allows us to obtain results in a relatively short amount of CPU time. We impose an initially uniform horizontal magnetic field. Unless otherwise stated our results are for a numerical truncation of  $N = L = M = 20$ , and with this, the solution appears well resolved. The results were checked over a range of timesteps, and at higher truncation for various diffusivity ratios  $\eta$  and layer sizes, with no appreciable change in the observed behaviour.

#### 4.4.1 $\eta = \text{constant}$

We first consider the simplest case which is to make our upper layer uniformly conducting. We look at  $\eta = 1, 10, 100$  and  $1000$  for different layer thicknesses  $\epsilon = 0.1$  (Figure 4.2),  $\epsilon = 0.5$  (Figure 4.3) and  $\epsilon = 1$  (Figure 4.4), and compare with the fully insulating case (see Figure 4.1). For low values of  $\eta$  the field in the core evolves more slowly and the flux expulsion is suppressed making the field lines more horizontal at the core-mantle boundary. This is true even for a thin layer ( $\epsilon = 0.1$ ). As we increase  $\eta$  the expulsion process becomes more pronounced with the field lines diffusing more quickly, and we see that the field behaviour gradually evolves to that of the insulating case. For  $\eta = 1000$  the field picture resembles very closely that of the fully insulating mantle case. This being the case we do not pursue higher values of  $\eta$ . The size of the layer is not important here.

#### 4.4.2 $\eta = f(z)$

We now consider a  $z$ -dependence on  $\eta$ . We want to model a rapid increase in diffusivity with height, so we look at two types, a linear dependence and a power law relationship.

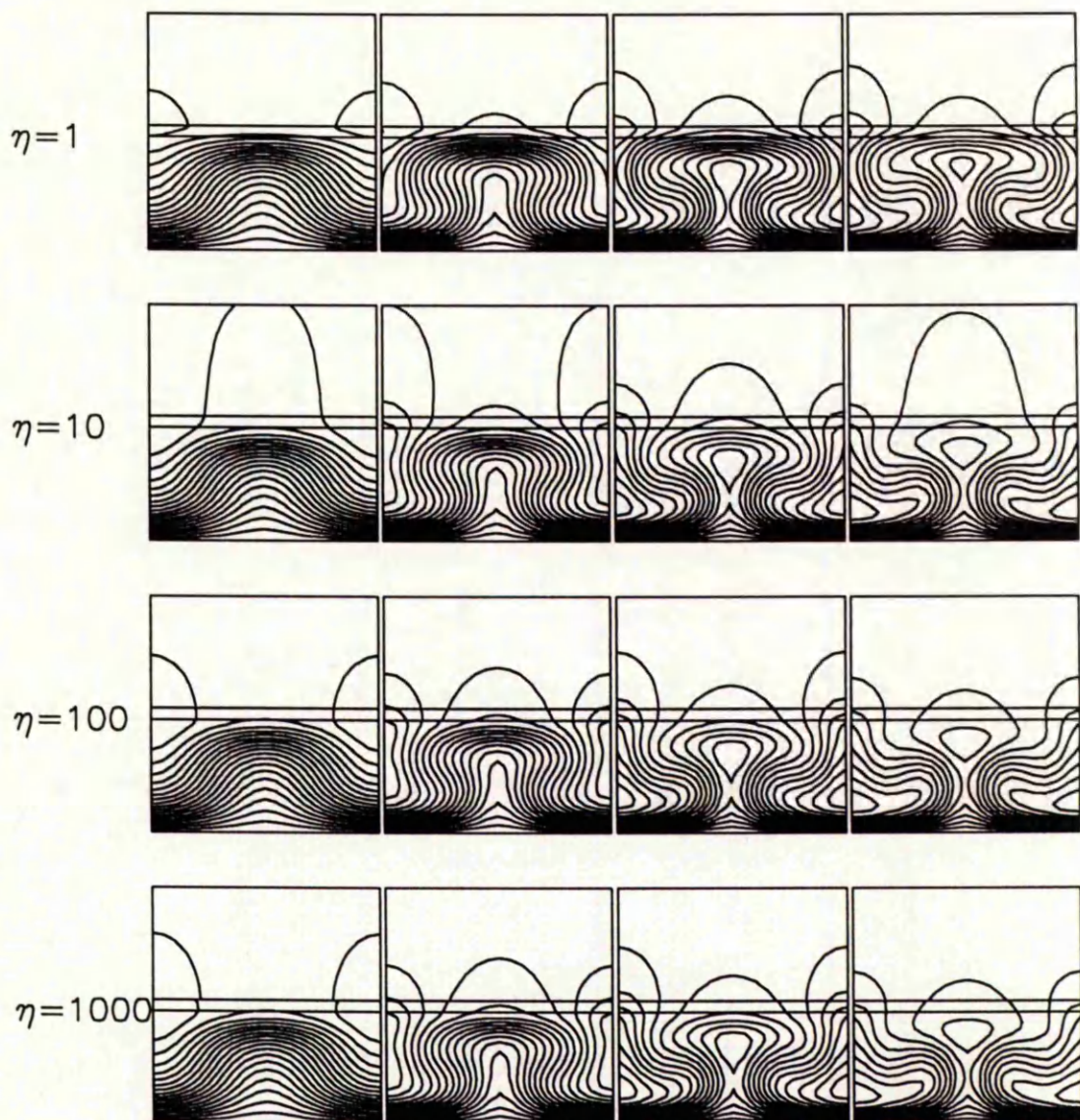


Figure 4.2: Time evolution of the magnetic field with diffusivity ratios  $\eta = 1, 10, 100$  and  $1000$ , and with a conducting layer of thickness  $\epsilon = 0.1$ ,  $R_m = 50$ ,  $N = L = M = 50$  and streamfunction (4.52). The timestep is  $5 \times 10^{-5}$  and the pictures are taken every 250 timesteps.

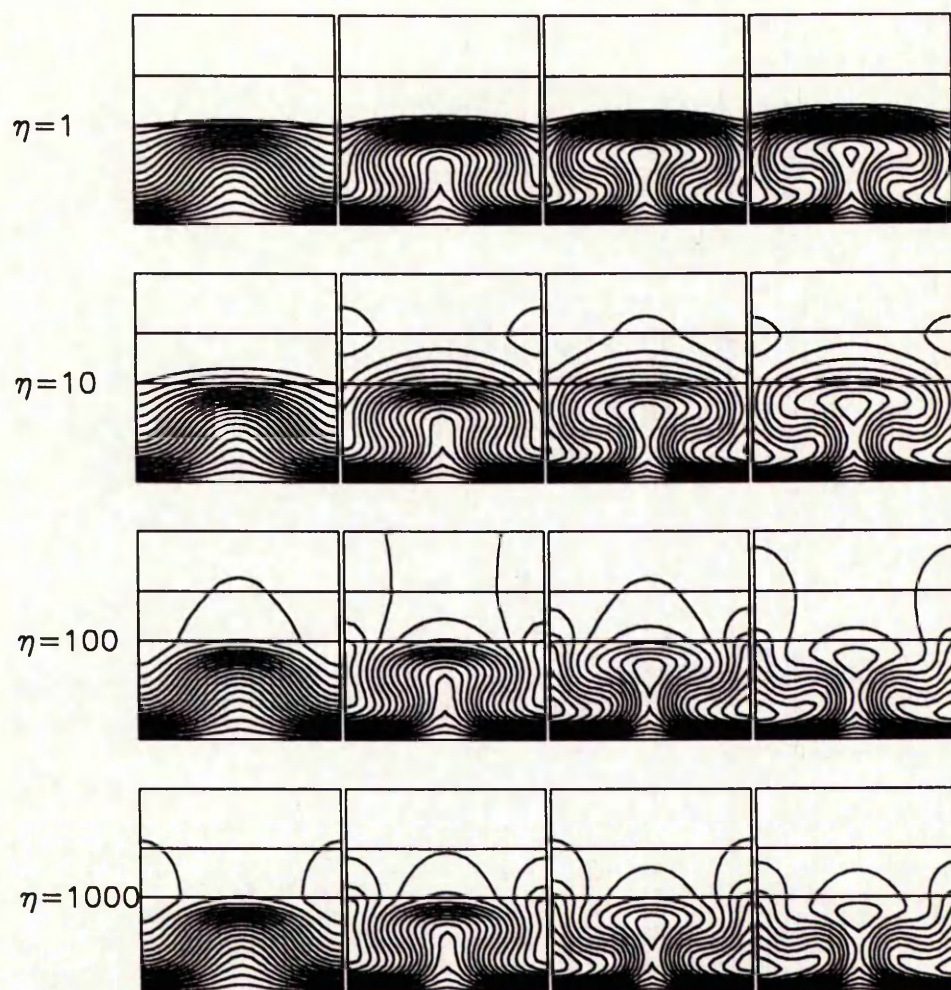


Figure 4.3: As Figure 4.2 but with  $\epsilon = 0.5$ .

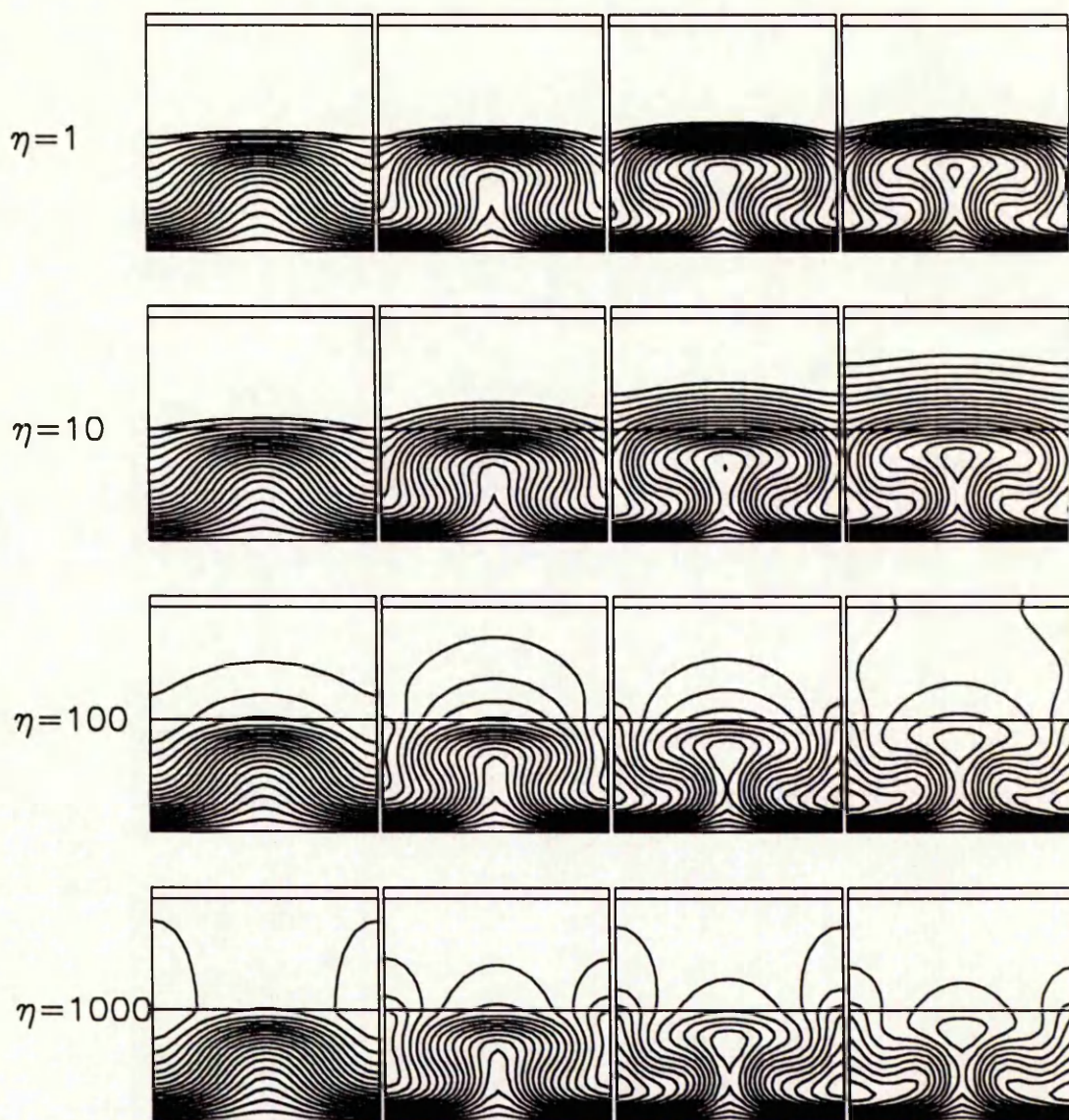


Figure 4.4: As Figure 4.2 but with  $\epsilon = 1$ .

$$(1) \eta = 1 + z \times 10^n$$

We look at the cases  $n = 1, 2$  and  $3$ . We show the field evolution for  $\epsilon = 0.1, 0.5$  and  $1$  in Figures 4.5, 4.6 and 4.7 respectively. When  $n = 1$  we find, not surprisingly, that the behaviour is somewhere between the cases  $\eta = 1$  and  $\eta = 10$  of Section 4.4.1. We see the slow expulsion of nearly horizontal field lines and diffusion of the field upwards. When  $n = 2$  we see the field lines becoming more drawn out as  $z$  increases, and when  $n = 3$  the field picture resembles the fully insulating case. Again, even with a thin conducting layer  $\epsilon = 0.1$ , the expulsion process can be inhibited.

$$(2) \eta = (1 + z)^n$$

We display results for  $n = 3, 6, 9$  and  $12$  with layer sizes  $\epsilon = 0.1, 0.5$  and  $1$  in Figures 4.8, 4.9 and 4.10 respectively. For low  $n$ , behaviour is similar to the  $\eta = 10$  case of Section 4.4.1. As  $n$  is increased, the field lines rise faster with increasing  $z$ , with a bell shaped pattern eventually emerging. The field pattern in the core develops more slowly than in the insulating case, even with a thin layer and when  $n$  is large.

#### 4.4.3 $\eta = g(x)$

It is believed (Jeanloz 1990) that the bottom of the mantle (the  $D''$  layer) can have large lateral heterogeneity in its conductivity, with variations of several orders of magnitude over a short lengthscale. We attempt to model this here, the simplest method of doing so being to use trigonometric functions for  $\eta$ . We show results for four choices

$$(1) \eta = 1000 + 999 \sin\left(\frac{3\pi x}{\alpha}\right)$$

$$(2) \eta = 1000 + 999 \cos\left(\frac{3\pi x}{\alpha}\right)$$

$$(3) \eta = 1000 + 999 \sin\left(\frac{5\pi x}{\alpha}\right)$$

$$(4) \eta = 1000 + 999 \cos\left(\frac{5\pi x}{\alpha}\right)$$

These choices vary  $\eta$  from  $1$ , where conductivity is the same as in the core, to  $1000$ , which we have seen produces results similar to the fully insulating case,

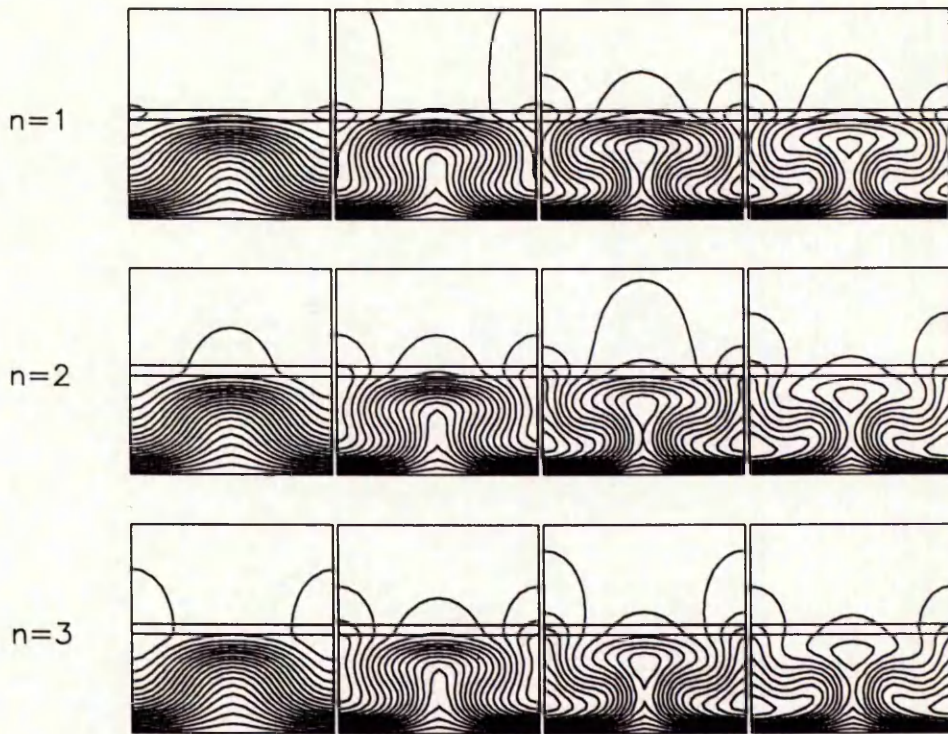


Figure 4.5: As Figure 4.2, but with a linear  $z$ -dependence for  $\eta$ ,  $\eta = 1 + z \times 10^n$  and  $\epsilon = 0.1$ .

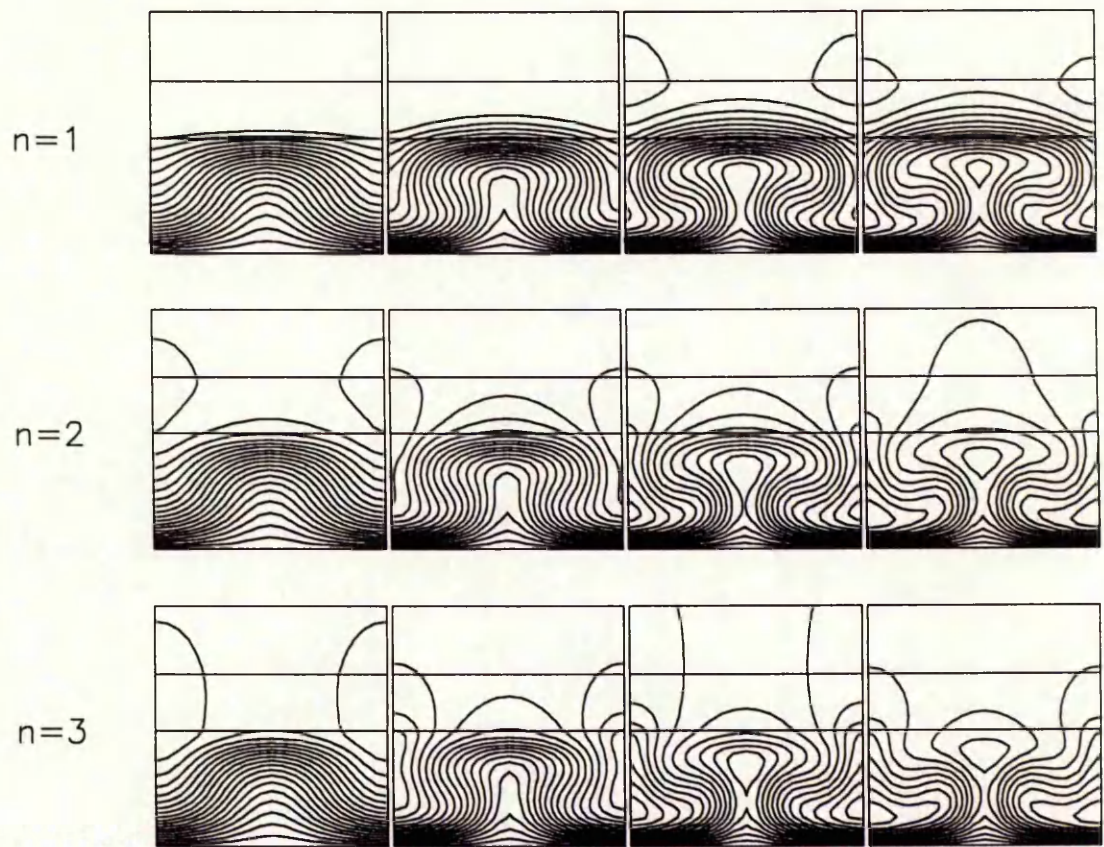


Figure 4.6: As Figure 4.5 but with  $\epsilon = 0.5$ .

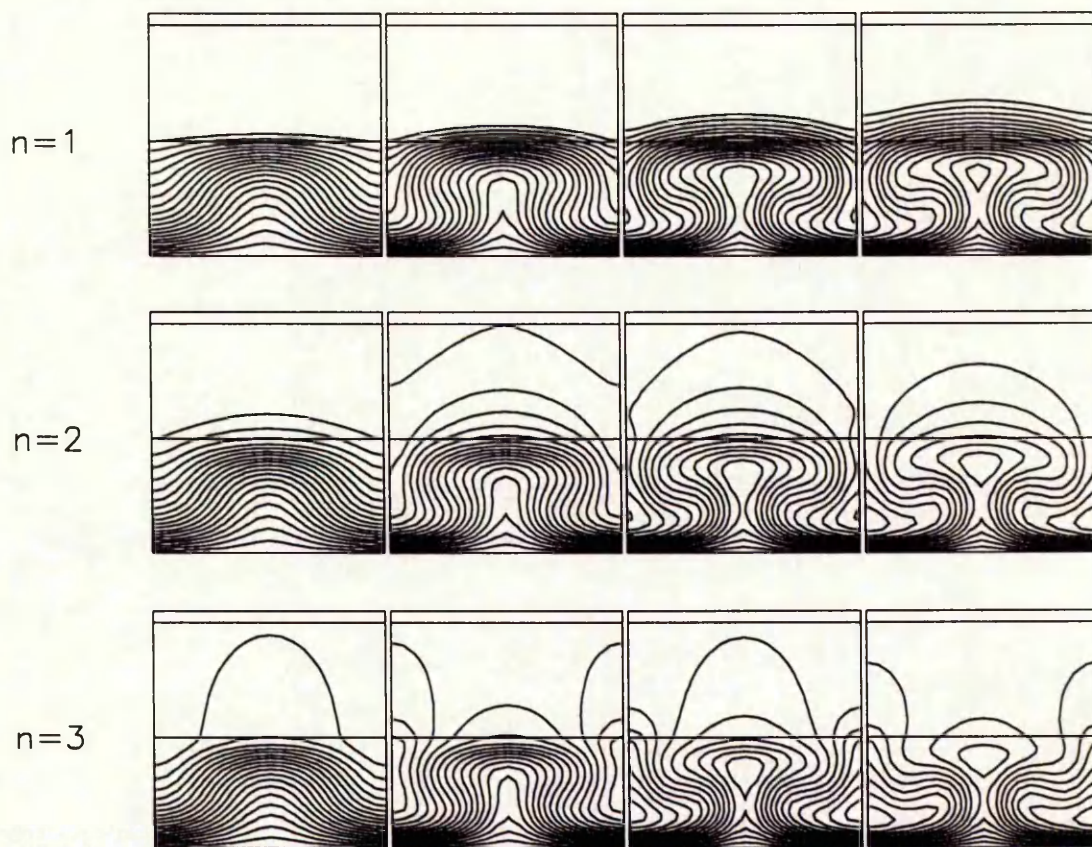


Figure 4.7: As Figure 4.5 but with  $\epsilon = 1$ .

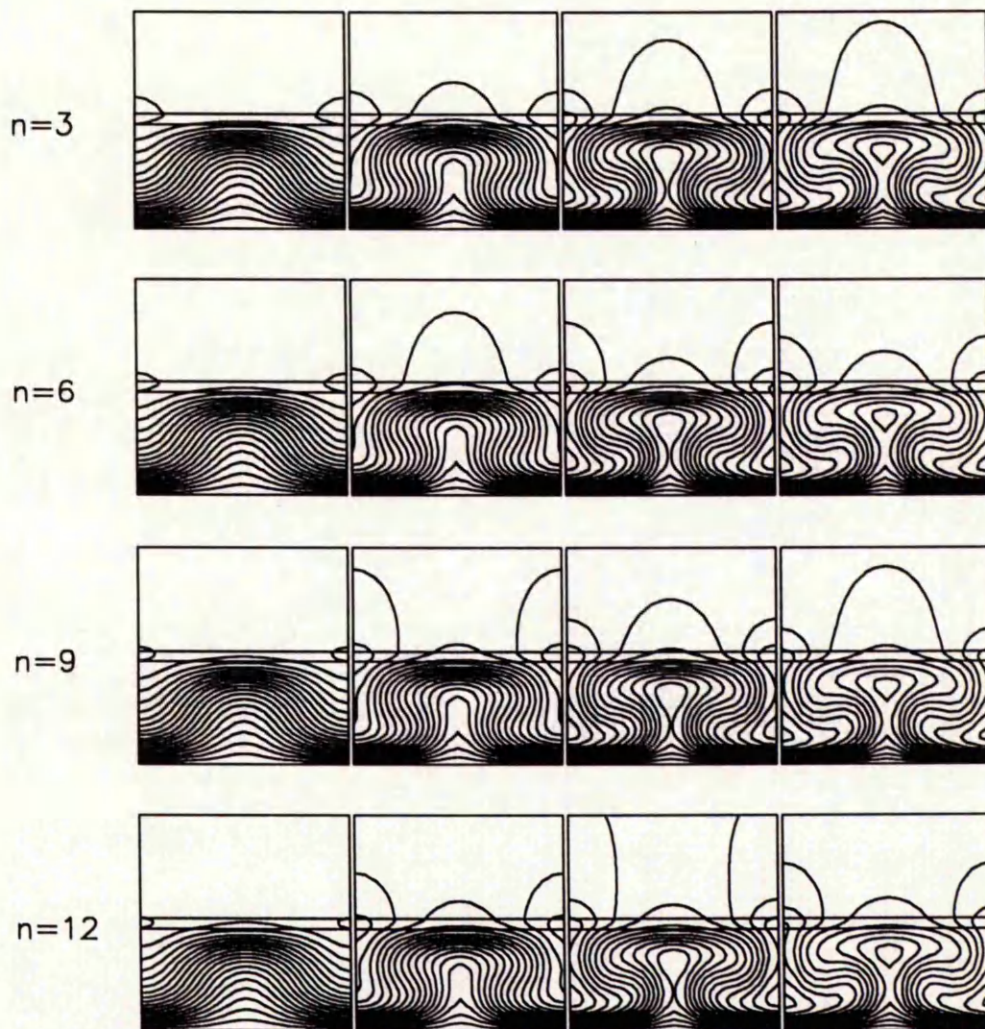


Figure 4.8: As Figure 4.2, but with a power law  $z$ -dependence,  $\eta = (1 + z)^n$  and  $\epsilon = 0.1$ .

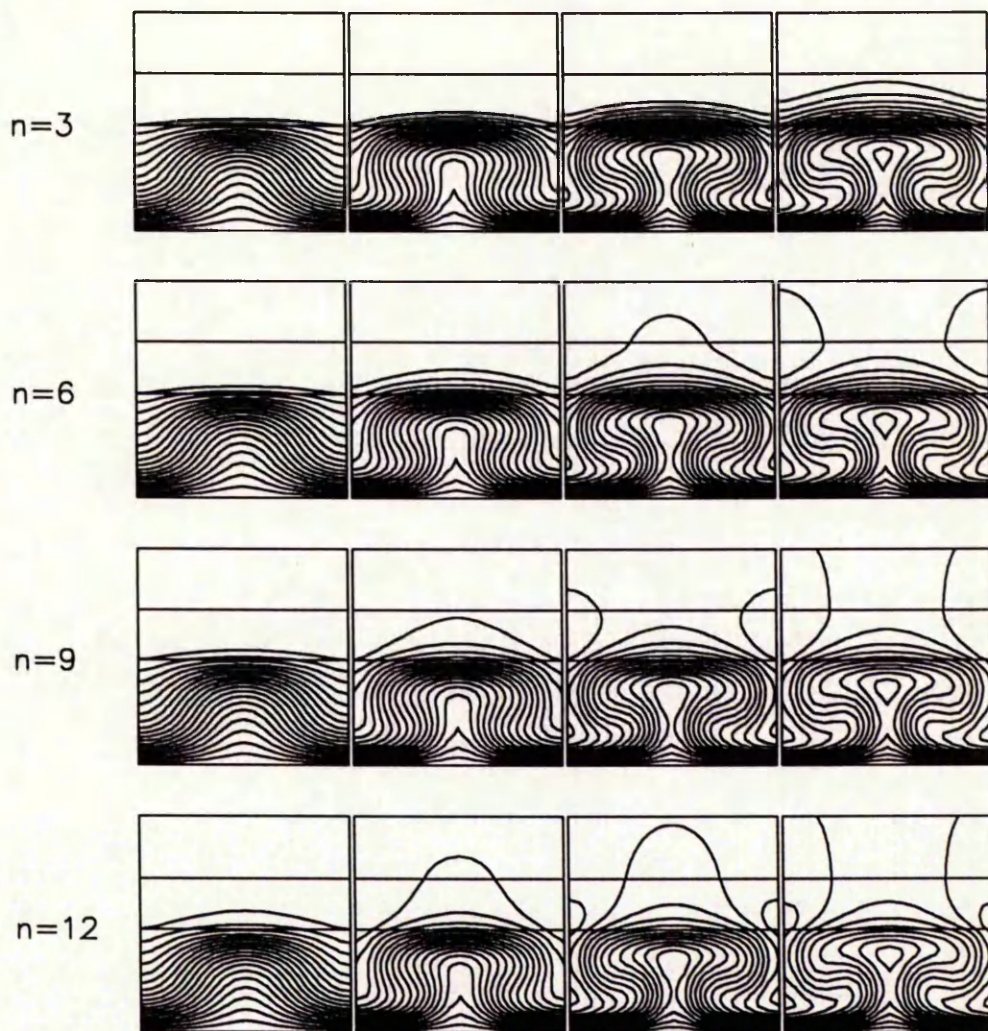


Figure 4.9: As Figure 4.8 but for  $\epsilon = 0.5$ .

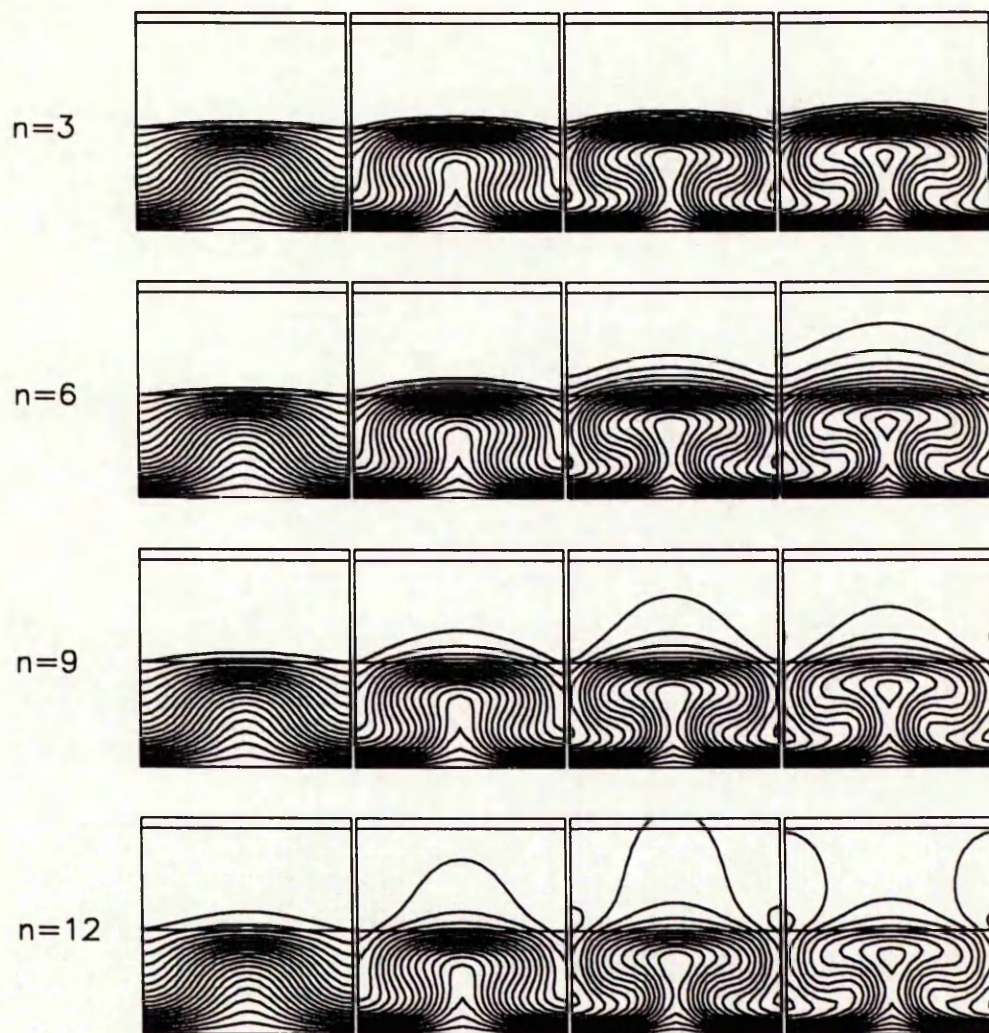


Figure 4.10: As Figure 4.8 but with  $\epsilon = 1$ .

and give two different lengthscales for the lateral variation. We display the field evolution with time for a layer size  $\epsilon = 0.1$  in Figure 4.11, and for  $\epsilon = 0.5$  in Figure 4.12. We can see that the heterogeneity has a very noticeable effect on the field lines. In the conducting layer there can be much distortion. This is most evident with a larger layer size, but even with  $\epsilon$  small the field lines are noticeably affected by the variation in conductivity. In such a case though, the field pattern is only really altered inside the conducting layer, with the solution outwith the layer almost completely unaffected by the layer. When the layer is thicker however, we also see differences in the core and upper mantle. In the core evolution is more restricted than in the fully insulating case, and the expulsion slower, similar to what we have seen in Sections 4.4.1 and 4.4.2. In the upper mantle, we can see that the “pinning” of field lines in regions of higher conductivity in the conducting layer, can lead to the shifting of the expelled field lines (e.g., Figure 4.12 top row) or the inhibition of the expulsion into the upper region (e.g., Figure 4.12 second row). We especially notice that the structure of the field in the mantle is representative of the conductivity in the mantle, and not of the structure of the core field in this case.

Because we are looking at large variation over a short lengthscale, we increase our numerical truncation in  $x$  to  $N = 40$  to check that our solution is well resolved. We find though, that the behaviour is essentially the same as for  $N = 20$ .

#### 4.4.4 Long term behaviour

In the results we have displayed so far, we have only considered the solution up until about  $t = 0.05$ . It is of interest to see what happens to the solution over a longer period of time. We find that for all the cases considered above, the solution eventually reaches a steady form whose amplitude gradually decreases. Figures 4.13 and 4.14 show the behaviour of the horizontal magnetic field strength  $B_x$  with time for a variety of parameters in the core and mantle respectively.  $B_x$  was calculated as in Section 4.3.1 from the solution in the centre of each layer. After undergoing the evolution pictured above the solution eventually settles down to

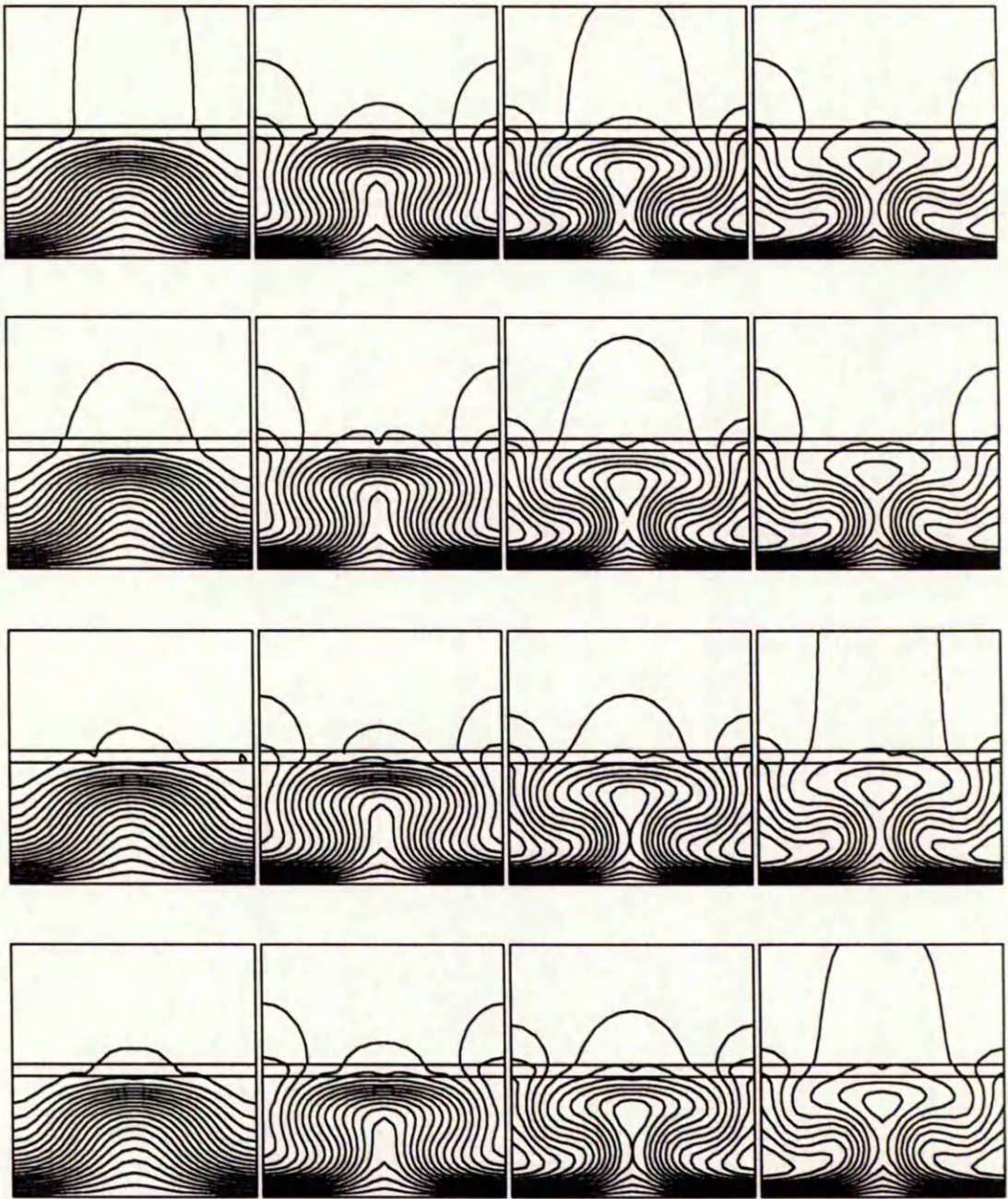


Figure 4.11: As previously, but now considering the  $x$ -dependence for  $\eta$  respectively from top to bottom  $\eta = 1000 + 999 \sin\left(\frac{3\pi x}{\alpha}\right)$ ,  $\eta = 1000 + 999 \cos\left(\frac{3\pi x}{\alpha}\right)$ ,  $\eta = 1000 + 999 \sin\left(\frac{5\pi x}{\alpha}\right)$  and  $\eta = 1000 + 999 \cos\left(\frac{5\pi x}{\alpha}\right)$ , and with  $\epsilon = 0.1$ .

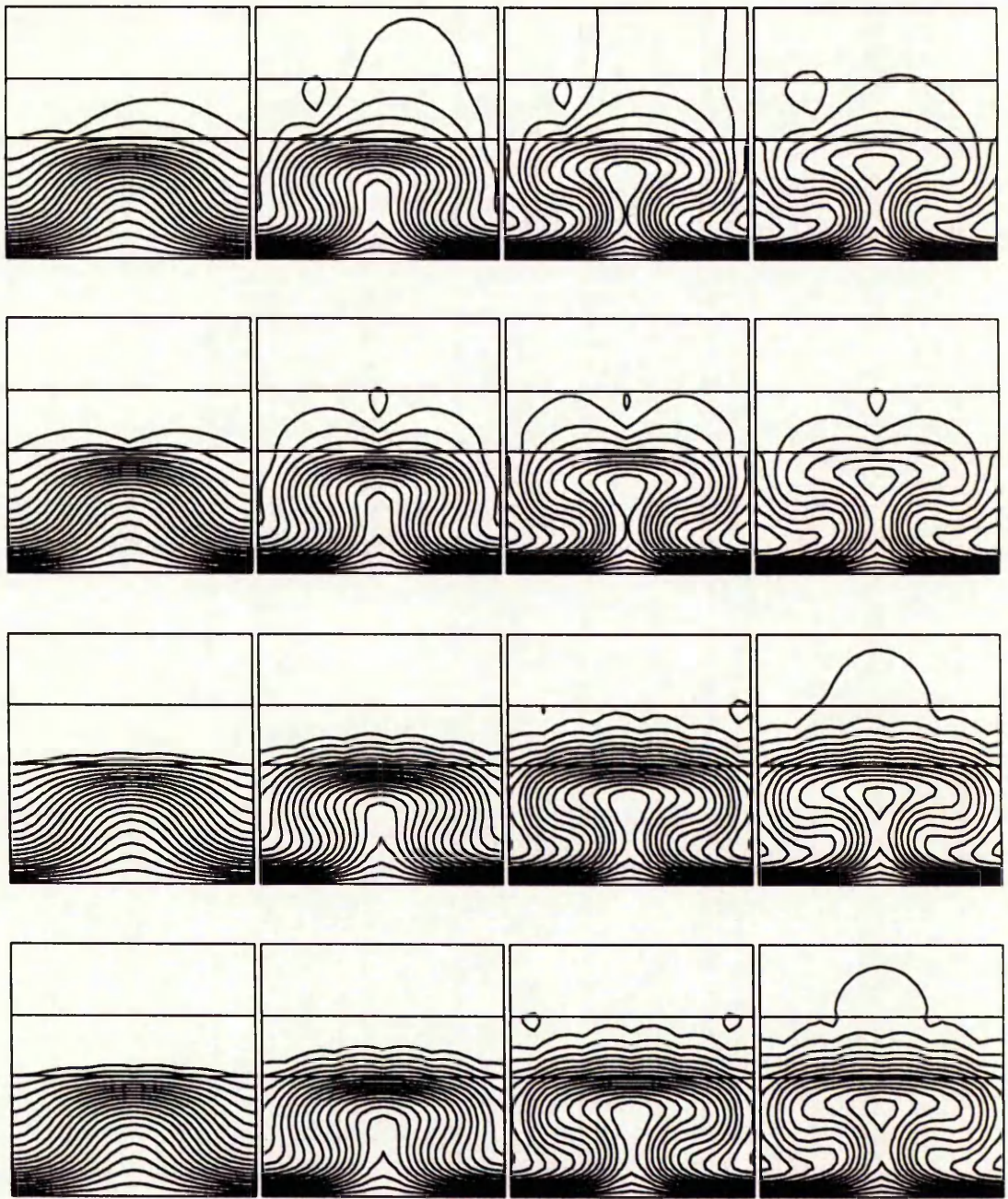


Figure 4.12: As Figure 4.11 but with  $\epsilon = 0.5$ .

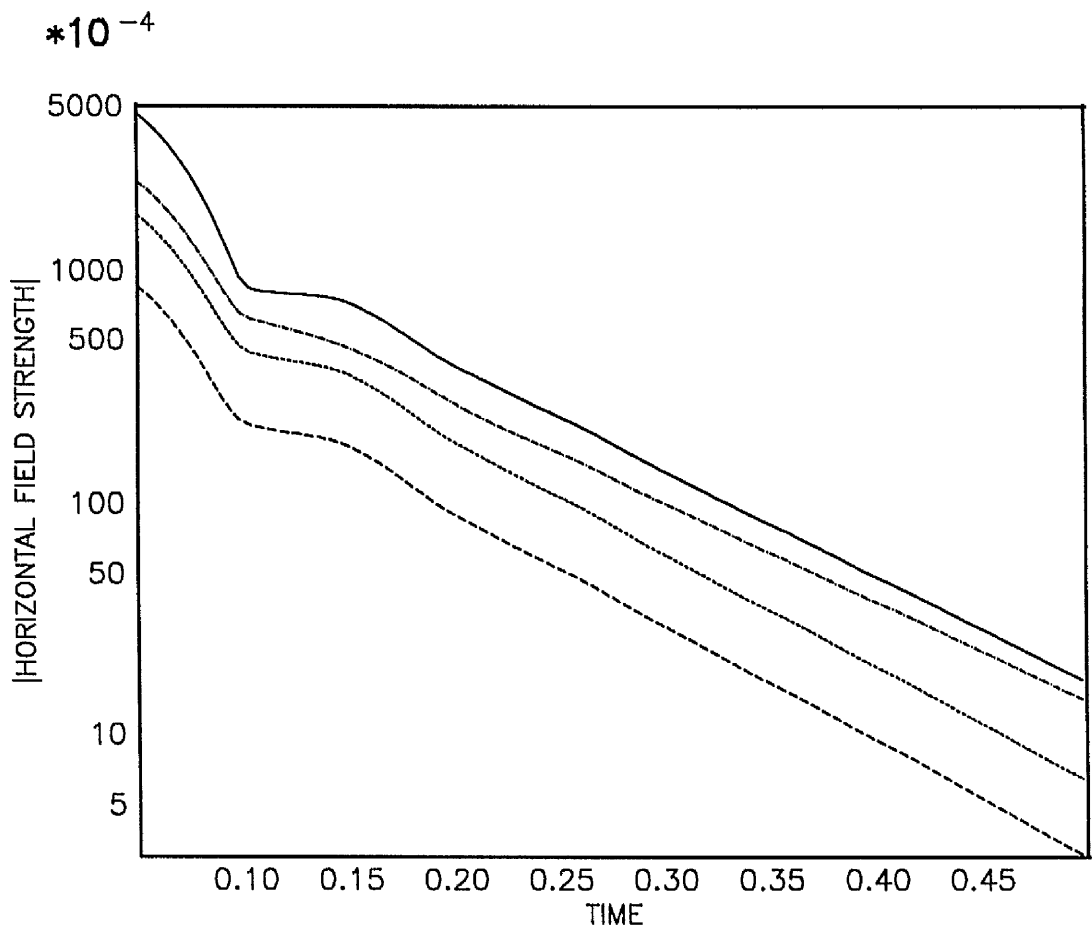


Figure 4.13: Graph of horizontal magnetic field  $B_x$  against time calculated at the centre of the core layer. The curves shown are for  $\epsilon = 0.5, \eta = 1$  (full line),  $\epsilon = 0.5, \eta = 10$  (short dashed line),  $\epsilon = 0.1, \eta = 10$  (long dashed line) and  $\epsilon = 0.5, \eta = (1 + z)^{12}$  (dot-dash line).

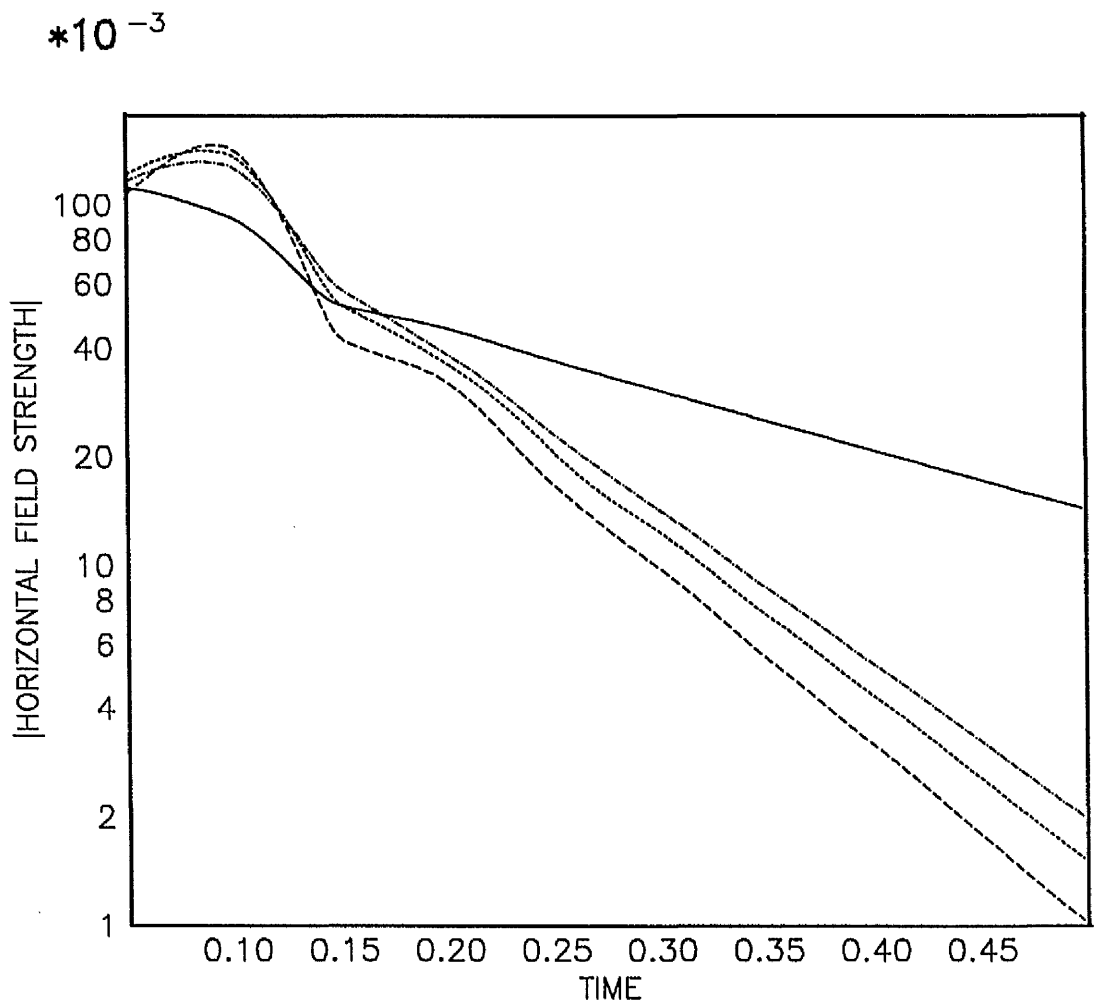


Figure 4.14: As Figure 4.13, but with  $B_x$  calculated at the centre of the mantle layer. The curves shown are for  $\epsilon = 0.5, \eta = 10$  (full line),  $\epsilon = 0.1, \eta = 10$  (short dashed line),  $\epsilon = 0.5, \eta = 1 + z \times 10^3$  (long dashed line) and  $\epsilon = 0.5, \eta = (1 + z)^{12}$  (dot-dash line).

steady state, and we find in all cases that the field then just decays exponentially with time.

#### 4.4.5 Effect of changing initial magnetic field

Although a natural choice as initial field, and for making comparison with Bloxham's results, an initially uniform horizontal field does not satisfy the boundary conditions at the upper insulating boundary [see equation (4.23)]. In the insulating region, if one component of the field is zero, then the other component must necessarily be zero also, so our non-zero, purely horizontal field cannot be sustained. To determine whether or not this is a problem, we consider an initial field which satisfies all the boundary conditions, namely

$$A = (z - \epsilon)^2(z + 1) \quad (4.53)$$

which is horizontal still, but non-uniform. Running our program with this field, we find that although field evolution is different at first, we eventually see the same behaviour emerging as for our uniform field. We illustrate this for  $\eta = 10$  in Figure 4.15, and we can compare the final contour plot, with the final plot of Figure 4.3 (second row). Since our results are qualitatively the same with both fields, we conclude that the use of an initially uniform field is not a problem.

### 4.5 DISCUSSION

We have produced a 2D numerical model for the expulsion of magnetic flux from the core into a conducting mantle. We have looked at different distributions of conductivity for the mantle, making comparison with the work of Bloxham (1986), who studied the same problem with an insulating mantle. We have seen that making the lower mantle conducting can have a noticeable effect on the solution. Even a thin layer with a conductivity close to that of the core can slow the expulsion rate and restrict the development of the core field. This can be further seen in Figures 4.5, 4.6 and 4.7 where we have conductivity falling off rapidly with increasing  $z$ . Perhaps the most interesting case is where we try to

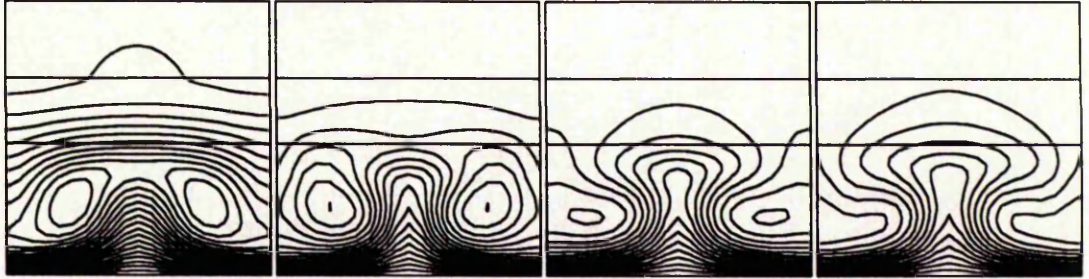


Figure 4.15: Time evolution of magnetic field with initial field chosen to satisfy top boundary condition,  $A = (z - \epsilon)^2(z + 1)$ , and for  $\epsilon = 0.5$  and  $\eta = 10$ . The timestep here is  $5 \times 10^{-5}$  and pictures are taken every 500 timesteps.

model the lateral heterogeneity in conductivity believed to occur in the bottom  $D''$  layer of the mantle. Modelling this can have a strong effect on the field lines in the conducting layer. If this layer is thin, then the overall effect on the field evolution is minimal, but a thicker layer can affect the field pattern considerably. From a geophysical viewpoint, what we would expect to see would depend on the nature of the flow in the outer core. If the fluid motion was taking place through the whole outer core region, then the thin conducting layer regime would be appropriate, since the outer core thickness is  $\sim 2270\text{km}$  (Gubbins and Roberts, 1987) so this is roughly equivalent to  $\epsilon = 0.1$  in our model. However if the flow is a more local one, in relation to the core-mantle boundary, then a thicker layer would be relevant, and our more interesting results would then apply. In particular, with a thicker conducting layer we have seen that the structure of the field emerging from the mantle is largely due to the conductivity of the mantle, and is not representative of the field in the core.

Overall then, the presence of even a thin layer of appreciable conductivity at the base of the mantle, can affect the expulsion of magnetic field from the core. It would be worthwhile therefore, in future models, to include the finite conductivity in the mantle.

## References.

- Acheson, D.J., 1978. Magnetohydrodynamic waves and instabilities in rotating fluids, in *Rotating fluids in geophysics*, pp. 315–349, eds. Roberts, P.H. and Soward, A.M., Academic Press, London.
- Acheson, D.J., 1979. On magnetoconvection in a rotating layer of high thermal conductivity, *Astrophys. Space Sci.* **65**, 453–458.
- Acheson, D.J., 1983. Local analysis of thermal and magnetic instabilities in a rapidly rotating fluid, *Geophys. Astrophys. Fluid Dynam.* **27**, 123–136.
- Aldredge, I. R., 1977. Deep mantle conductivity, *J. Geophys. Res.* **82**, 5427–5431.
- Benton, E. R. & Whaler, K. A., 1983. Rapid diffusion of the poloidal geomagnetic field through the weakly conducting mantle: a perturbation solution, *Geophys. J. R. Astr. Soc.* **75**, 77–100.
- Bloxham, J., 1986. The expulsion of magnetic flux from the Earth's core, *Geophys. J. R. Astr. Soc.* **87**, 669–678.
- Bloxham, J. and Gubbins, D., 1985. The secular variation of Earth's magnetic field, *Nature* **317**, 777–781.
- Bloxham, J., Gubbins, D. and Jackson, A., 1989. Geomagnetic secular variation, *Phil. Trans. R. Soc. Lond.* **A329**, 415–502.
- Bloxham, J. and Jackson, A., 1991. Fluid flow near the surface of Earth's outer core, (Abstract) *Geophys. Astrophys. Fluid Dynam.* **60**, 366–368.
- Boda, J., 1988. Thermal and magnetically driven instabilities in a non-constantly stratified fluid layer, *Geophys. Astrophys. Fluid Dynam.* **44**, 117–139.
- Braginsky, S. I. and Fishman, V. M., 1976. Electromagnetic interaction of the core and mantle when electrical conductivity is concentrated near the core boundary, *Geomag. Aeron.* **16**, 601–606.
- Busse, F., 1978. Theory of Geomagnetism, in *Rotating fluids in Geophysics*, pp. 361–388, eds. Roberts, P.H. and Soward, A.M., Academic Press, London.

- Drew, S.J., 1991. Thermal convection in a spherical shell with a variable radius ratio, *Geophys. Astrophys. Fluid Dynam.* **59**, 165–183.
- Drew, S.J., 1992a. The effect of a stable layer at the core-mantle boundary on thermal convection, *Geophys. Astrophys. Fluid Dynam.* **65**, 173–182.
- Drew, S.J., 1992b. Magnetic field expulsion into a conducting mantle, submitted.
- DuCruix, J., Courtillot, V. & Le Mouél, J.-L., 1980. The late 1960's secular variation impulse, the eleven year magnetic variation and the electrical conductivity of the deep mantle, *Geophys. J. R. Astr. Soc.* **61**, 73–94.
- Dziewonski, A.M. and Anderson, D.L., 1981. Preliminary reference Earth model, *Phys. Earth Planet. Inter.* **25**, 297–356.
- Eltayeb, I.A. and Kumar, S., 1977. Hydromagnetic convective instability of a rotating, self-gravitating fluid sphere containing a uniform distribution of heat sources, *Proc R. Soc. Lond.* **A353**, 145–162.
- Fearn, D.R., 1979a. Thermally driven hydromagnetic convection in a rapidly rotating sphere, *Proc R. Soc. Lond.* **A369**, 227–242.
- Fearn, D.R., 1979b. Thermal and magnetic instabilities in a rapidly rotating fluid sphere, *Geophys. Astrophys. Fluid Dynam.* **14**, 103–126.
- Fearn, D.R., 1983a. Boundary conditions for a rapidly rotating hydromagnetic system in a cylindrical container, *Geophys. Astrophys. Fluid Dynam.* **25**, 65–75.
- Fearn, D.R., 1983b. Hydromagnetic waves in a differentially rotating annulus I. A test of local stability analysis, *Geophys. Astrophys. Fluid Dynam.* **27**, 137–162.
- Fearn, D.R., 1984. Hydromagnetic waves in a differentially rotating annulus II. Resistive instabilities, *Geophys. Astrophys. Fluid Dynam.* **30**, 227–239.
- Fearn, D.R., 1985. Hydromagnetic waves in a differentially rotating annulus III. The effect of an axial field, *Geophys. Astrophys. Fluid Dynam.* **33**, 185–197.

- Fearn, D.R., 1988. Hydromagnetic waves in a differentially rotating annulus IV. Insulating boundaries, *Geophys. Astrophys. Fluid Dynam.* **44**, 55–75.
- Fearn, D.R., 1989a. Differential rotation and thermal convection in a rotating hydromagnetic system, *Geophys. Astrophys. Fluid Dynam.* **49**, 173–193.
- Fearn, D.R., 1989b. Compositional Convection and the Earth's core, in *Geomagnetism and Paleomagnetism*, pp. 335–346, eds. Lowes, F.J. *et al*, Kluwer Academic Publishers, Dordrecht.
- Fearn, D.R., 1991a. Eigensolutions of boundary value problems using inverse iteration, *J. Comp. Appl. Math.* **34**, 201–209.
- Fearn, D.R., 1991b. Convection near the Earth's core-mantle boundary?, in *Advances in Solar System MHD*, pp. 61–75, ed. Priest, E.R., Cambridge University Press.
- Fearn, D.R. and Loper, D.E., 1981. Compositional convection and stratification of the Earth's core, *Nature* **289**, 393–394.
- Fearn, D.R. and Proctor, M.R.E., 1983a. Hydromagnetic waves in a differentially rotating sphere, *J. Fluid Mech.* **128**, 1–20.
- Fearn, D.R. and Proctor, M.R.E., 1983b. The stabilizing role of differential rotation on hydromagnetic waves, *J. Fluid Mech.* **128**, 21–36.
- Fearn, D. R. & Proctor, M. R. E., 1992. Magnetostrophic balance in non-axisymmetric non standard dynamo models, *Geophys. Astrophys. Fluid Dynam.* , in press.
- Fearn, D.R., and Richardson, L., 1991. Convection in a non-uniformly stratified fluid permeated by a non-uniform magnetic field, *Geophys. J. Int.* **104**, 203–211.
- Fearn, D.R., Roberts, P.H. and Soward, A.M., 1988. Convection, stability and the dynamo, in *Energy stability and convection*, pp. 60–324, eds. Straughan, B. and Galdi, G.P., Longmans, Harlow.
- Fearn, D.R. and Weiglhofer, W.S., 1991a. Magnetic instabilities in rapidly rotating spherical geometries I. From cylinder to sphere, *Geophys. Astrophys. Fluid Dynam.* **56**, 159–181.

- Fearn, D.R. and Weiglhofer, W.S., 1991b. Magnetic instabilities in rapidly rotating spherical geometries II. More realistic fields and resistive instabilities, *Geophys. Astrophys. Fluid Dynam.* **60**, 275–294.
- Fearn, D.R. and Weiglhofer, W.S., 1992a. Resistive instabilities and the magnetostrophic approximation, *Geophys. Astrophys. Fluid Dynam.* **63**, 111–138.
- Fearn, D.R. and Weiglhofer, W.S., 1992b. Magnetic instabilities in rapidly rotating spherical geometries III. The effect of differential rotation, *Geophys. Astrophys. Fluid Dynam.* , in press.
- Gire, C., Le Mouëli, J.-L., and Madden, T., 1986. Motions at the core surface derived from SV data, *Geophys. J. R. Astr. Soc.* **84**, 1–29.
- Gottlieb, D. and Orszag, S.A., 1981. Numerical analysis of spectral methods: Theory and applications, *SIAM*, Philadelphia, PA.
- Gubbins, D., 1977. Energetics of the Earth's core, *J. Geophys.* **43**, 453–464.
- Gubbins, D., 1982. Finding core motions from magnetic observations, *Phil. Trans. R. Soc. Lond.* **A306**, 247–254.
- Gubbins, D., 1991. On unique determination of toroidal or geostrophic flow in the Earth's core, *Geophys. Astrophys. Fluid Dynam.* **60**, 165–176.
- Gubbins, D. and Masters, T.G., 1979. Driving mechanisms for the Earth's dynamo, *Adv. Geophys.* **21**, 1–50.
- Gubbins, D., Masters, T.G. and Jacobs, J.A., 1979. Thermal evolution of the Earth's core, *Geophys. J. R. Astr. Soc.* **59**, 57–99.
- Gubbins D., Thomson C.J. and Whaler K.A., 1982. Stable regions in the Earth's liquid core, *Geophys. J. R. Astr. Soc.* **68**, 241–251.
- Gubbins, D. & Roberts, P. H., 1987. Magnetohydrodynamics of the Earth's core, in *Geomagnetism* Vol. 2, pp. 1–183, ed. Jacobs, J. A., Academic Press, London.
- Jeanloz, R., 1990. The nature of the Earth's core, *Ann. Rev. Earth Planet. Sci.* **18**, 357–386

- Li, X. & Jeanloz, R., 1987. Electrical conductivity of (Mg,Fe)SiO<sub>3</sub> perovskite and a perovskite-dominated assemblage at lower mantle conditions, *Geophys. Res. Lett.* **14**, 1075–1078
- Loper, D.E., 1989. Dynamo Energetics and the structure of the outer core, *Geophys. Astrophys. Fluid Dynam.* **49**, 213–219.
- Orszag, S.A., 1972. Comparison of pseudospectral and spectral approximation, *Stud. appl. Math.*, **51**, 253–259.
- Peters, G. and Wilkinson, J.H., 1971a. Eigenvectors of real and complex matrices by LR and QR triangularisations, in *Handbook for Automatic Computation*, Vol. 2: Linear Algebra, eds. Wilkinson, J.H. and Reinsch, C., pp. 370–395. Springer.
- Peters, G. and Wilkinson, J.H., 1971b. The calculation of specified eigenvectors by inverse iteration, in *Handbook for Automatic Computation*, Vol. 2: Linear Algebra, eds. Wilkinson, J.H. and Reinsch, C., pp. 418–439. Springer.
- Peyronneau, J. & Poirier, J. P., 1989. Electrical conductivity of the Earth's lower mantle, *Nature* **342**, 537–539
- Roberts, P.H., 1968. On the thermal instability of a rotating fluid sphere containing heat sources, *Phil. Trans. R. Soc. Lond.* **A263**, 93–117.
- Roberts, P.H. and Loper, D.E., 1979. On the diffusive instability of some simple steady magneto-hydrodynamic flows, *J. Fluid Mech.* **90**, 641–668.
- Roberts, P.H. and Soward, A.M., 1992. Dynamo theory, *Ann. Rev. Fluid Mech.*, **24**, 459–512.
- Ševčík, S., 1989. Thermal and magnetically driven instabilities in a non-constantly stratified rapidly rotating fluid layer with azimuthal magnetic field, *Geophys. Astrophys. Fluid Dynam.* **49**, 195–211.
- Soward, A.S., 1979. Thermal and magnetically driven convection in a rapidly rotating fluid layer, *J. Fluid Mech.* **90**, 669–684.
- Soward, A.S., 1991. The Earth's Dynamo, *Geophys. Astrophys. Fluid Dynam.* **62**, 191–209.

- Voorhies, C.V., 1986. Steady flows at the top of the Earth's core derived from geomagnetic field models, *J. Geophys. Res.* **91**, 12,444-12466.
- Wengle, H., Van den Bosch, B. and Seinfeld, J.H., 1978. Solution of atmospheric diffusion problems by pseudospectral and orthogonal collocation methods, *Atmospheric Environment*, **12**, 1021-1032.
- Whaler, K.A., 1980. Does the whole of the Earth's core convect?, *Nature* **287**, 528-530.
- Young, C. J. & Lay, T., 1987. The core-mantle boundary, *Ann. Rev. Earth Planet. Sci.* **15**, 25-46

